Design and Control of Microsatellite Clusters for Tracking Missions

by

John Daniel Griffith

B.S. in Aeronautics and Astronautics
Massachusetts Institute of Technology, 2005

Submitted to the Department of Aeronautics and Astronautics
in partial fulfillment of the requirements for the degree of

Master of Science in Aeronautics and Astronautics

at the

MASSACHUSETTS INSTITUTE OF TECHNOLOGY

June 2007

Author ....
Department of Aeronautics and Astronautics
May 21, 2007

Certified by ....
Leena Singh
Charles Stark Draper Laboratory
Thesis Supervisor

Certified by ....
Jonathan How
Associate Professor of Aeronautics and Astronautics
Thesis Advisor

Accepted by ....
Jaime Peraire
Professor of Aeronautics and Astronautics
Chairman, Department Committee on Graduate Students

Design and Control of Microsatellite Clusters for Tracking Missions

by

John Daniel Griffith

Submitted to the Department of Aeronautics and Astronautics
on May 21, 2007, in partial fulfillment of the
requirements for the degree of
Master of Science in Aeronautics and Astronautics

Abstract

Space-based tracking missions are an emerging interest that could be accomplished using a cluster of microsatellites. This thesis addresses the design of microsatellite clusters to accurately track a target in a probabilistic suborbital occupancy corridor by pursuing the following: orbit determination using optimal measurement principles, cluster design heuristics and fuel optimal cluster maintenance. These are all evaluated on a high-fidelity simulation testbed. First, the orbital determination approach utilizes optimal measurement principles to design a constellation of clusters that minimizes the average model-based target tracking error. A two part approach, (1) constellation design and (2) cluster design, reduces the overall orbit determination complexity. The constellation design provides continuous, 24 hour coverage of the occupancy corridor and virtual formation centers about which the cluster design formulates the relative microsatellite orbits. Results suggest that satellite separations, rather than the number of the microsatellites in the cluster, are more important for providing target tracking accuracy. Results also show that the J_2-induced relative drift of the satellites in a cluster can be reduced by several orders of magnitude with very little degradation in the cluster's tracking capability. Second, this research formulates a cluster design heuristic that provides a robust cluster viewing geometry for a target in any direction. This robust design heuristic provides tracking capability for a cluster that is demonstrated to be comparable to one specifically tuned for a particular target orbit. Third, this thesis presents a receding horizon Model Predictive Control approach to cluster maintenance that exhibits reduced cluster-wide fuel expenditure by allowing relative satellite drift while maintaining mission driven cluster characteristics. The controller achieves this performance by being robust to unmodeled dynamics and noise. Finally, the performance of the integrated cluster-based orbit determination, tracking and control laws is demonstrated on a high-fidelity, multi-satellite simulation testbed. Results include tracking performance and trade-offs as a function of various control objectives.

Thesis Supervisor: Leena Singh
Title: Senior Member of Technical Staff

Thesis Advisor: Jonathan How
Title: Associate Professor of Aeronautics and Astronautics

Acknowledgements

There are several people I would like to recognize for their help and support during the completion of my master's thesis. First, and foremost, I would like to thank my advisors. I am extremely grateful for having Leena Singh as a thesis advisor. Her advice and confidence in my work made the thesis process an entirely enjoyable one. I would like to thank Professor Jonathan How for his technical advice and direction that I believe helped me enrich the quality and depth of my research.

I would also like to acknowledge the Charles Stark Draper Laboratory for providing me with the opportunity to explore this thesis topic. In particular, I would like to express my appreciation to Ernie Griffith at Draper for his conversations and involvement with my research.

Finally, I would like to thank my family and friends for their support during my master's program. Without their support, I'm not sure I would have ever gotten this far. Thank you.

This thesis was prepared at The Charles Stark Draper Laboratory, Inc., under Independent Research and Development Project Number 20279-01.

(Author's Signature)

THIS PAGE INTENTIONALLY LEFT BLANK

Contents

List of Figures

THIS PAGE INTENTIONALLY LEFT BLANK

List of Tables

THIS PAGE INTENTIONALLY LEFT BLANK

Chapter 1

Introduction

This thesis is a conceptual study of using a cluster of microsatellites for space-based target tracking missions. This chapter provides the motivation, concept of operations, research objectives and outline for this thesis.

1.1 Motivation

The motivation for this research concept is to provide tracking capability of a Low Earth Orbit (LEO) region in a rotating Earth reference frame using space-based assets in a way that is generalizable to other tracking missions. Resources must be conserved and the best tracking accuracy possible must be provided given the assets being used. To do so, this research capitalizes on recent advances in microsatellite and formation flying technology.

1.1.1 Space Awareness

The ability to accurately track objects above the Earth's atmosphere has several critical space-based operational applications and inherent benefits to many fields including science, commerce and defense.

A space-based observation and tracking facility has many important applications for scientists (NASA) such as closely monitoring sites on the Earth at high risk of volcanic activity. In addition, both NASA and commercial organizations are currently engaged in tracking space debris. For example, the International Space Station recently had to maneuver to avoid a debris field from the destruction of the Chinese FENGYUN 1C polar-orbiting weather satellite due to a recent Chinese ASAT test. Over a thousand trackable pieces of debris have been identified from this test. Many older, nonoperational satellites still blindly orbit for years after the end of their effectiveness. The space above the Earth's atmosphere has become more populated with man-made satellites and their related debris [45]. Thus, the likelihood of collisions in space has greatly increased and any further collisions would lead to many smaller, yet still lethal, pieces of debris. A space-based tracking system could identify orbiting debris and nonoperational satellites that may pose as threats to current, operational satellites. If a piece of space debris were determined to be a threat to a satellite, then action could be taken so that the threatened satellite was no longer in danger.

Tracking ballistic trajectories is an important interest to nation defense. A typical ballistic trajectory scenario is broken down into three parts: the boost phase, the mid-course phase, and the terminal phase. The boost phase is generally the easiest to track and identify because the rockets are burning and the missile is moving relatively slow. However, this phase only lasts three to five minutes. The mid-course phase of the flight can last anywhere from twenty to thirty minutes. A series of land-, sea-, air- and space-based sensors either already exist or are in the early stages of development and would be capable of tracking a missile in this phase of flight. The terminal phase of flight corresponds to reentry into the Earth's atmosphere and lasts approximately thirty seconds. A space-based tracking cluster of microsatellites would track a ballistic missile in its second phase of flight. A space-based tracking system has several benefits over land- and sea-based assets such as the target does not need to be directly above the sensor. There are also no atmospheric noise disturbances associated with a space-based tracking system.

This research focuses on the problem of designing a *constellation of clusters* to track a ballistic object. This problem was selected because it is best possible to define and analyze the problem of monitoring a single long duration event in a localized area of space. This approach also provides the best avenue for generating generalizable scalable system solutions.

1.1.2 Recent Technological Advances

First generation satellites were built with the rationale that they should be robust to failure. It was reasonable to add redundant systems to a satellite if millions of dollars were to be spent designing and launching a satellite. If one system failed, then the entire satellite would not be rendered useless. However, a newer trend in satellite design has moved to building microsatellites (named as such because they are *micro* in size compared to previously built satellites) and nanosatellites. The transition to building microsatellites has also been supported by improvements in satellite reliability and, thus, many microsatellites do not have redundant systems. Technology advances in areas such as MEMS devices have allowed sensors on satellites to be built on a much smaller scale then ever before. Microsatellites have a great added advantage in that they are cheaper to launch into orbit since they weigh so much less than previously built satellites. The satellite industry's move to microsatellites has been a logical one given these benefits.

In many current and proposed microsatellite missions, several microsatellites flying in a formation work in tandem to perform missions with a high degree of success. Scharf et al. [28] defines formation flying as:

> A set of more than one spacecraft whose *dynamic states are coupled through a common control law.* In particular, at least one member of the set must 1) track a desired state relative to another member, and 2) the tracking control law must at the minimum depend upon the state of this other member.

In the past decade there have been several major advances in both the modeling and control of satellite relative motion that has made this shift to formation flying missions possible. The earliest models for formation flying used Hill's equations. Hill's equations, however, are only applicable for nearly circular orbits and over short periods of time. New advances in relative motion modeling accurately model highly eccentric orbits and incorporate some of the major disturbances such as drag and gravitational harmonics of the Earth [14, 24]. Newer, linearized dynamic models are now capable of modeling relative motion over longer periods of time with very high levels of accuracy.

There have also been strides in satellite formation control algorithms. Minimizing fuel consumption is extremely important for space missions since it is both a limited and expensive resource. One advance in current algorithms has been to take advantage of the natural dynamics of orbiting bodies to minimize fuel consumption [31, 5]. Others have utilized optimization and model predictive control (MPC) techniques to produce satellite trajectories in a formation that minimize cluster-wide fuel consumption [37, 19, 5, 4, 7].

These recent technological advances have provided several inherent benefits to using a cluster of microsatellites for space-based missions. Some of these benefits include [23]:

Adaptability Neither the geometry nor the number of satellites in a formation is fixed. Therefore, a formation of satellites is capable of adapting to new and different mission requirements.

Flexibility A formation of satellites can grow as needed. If system functions require additional satellites, then more satellites can be inserted into the formation. Similarly, satellites may be replaced or the cluster can reconfigure to accommodate the loss of information from a satellite when satellites run out of fuel or break.

Redundancy If a single sensor or satellite in the cluster fails, a formation of satellites should still be able to perform a mission to some degree of success. This also makes the cluster less susceptible to component failure.

Economy of Scale Redundant microsatellites lend themselves to major savings in production costs since they can be mass produced. Smaller sized satellites are also more manageable for testing and shipping and they can be launched together on one vehicle. In addition, they can piggyback on other launches to replenish currently existing clusters.

1.2 Concept of Operations

Several space-based target tracking missions that a cluster of microsatellites could perform have been identified. However, this research focuses on tracking engagement that is representative of a ballistic object tracking mission in LEO. The ballistic tracking application provides an interesting and definable problem because it requires 24 hour coverage of a well defined *occupancy corridor* that rotates with the Earth. The time of launch of the vehicle is, thus, assumed to be unknown.

1.2.1 Mission Statement

The mission statement considered in this thesis is to develop a space-based target tracking system capable of reliably meeting tracking accuracy specifications of an object in a probabilistic occupancy corridor.

The occupancy corridor used in this research is symbolic of a randomly chosen ballistic, suborbital reentry vehicle. Yet, all the approaches and results in this thesis are extendable and adaptable to other tracking scenarios. All satellite assets are assumed to be equipped with visual-based target tracking cameras capable of providing line-of-sight measurements to the target. In addition, each satellite is equipped with a GPS instrument to estimate its own position and velocity and star-tracker and IMU sensors to estimate attitude and attitude rate data. A centralized, extended Kalman filter extracts target position and velocity information from the collection of line-of-sight measurements.

1.2.2 Constellation of Clusters

The proposed system approach is a constellation of clusters since 24 hour coverage is required for this concept of operations. Ref. [29] defines a constellation as "a set of spacecraft whose states are not dynamically coupled in any way (i.e., the change of state of one spacecraft does not impact the state of another)." A constellation of clusters has a cluster of microsatellites instead of a satellite at each node of the constellation. The microsatellites in a single cluster are dynamically coupled and assumed to be capable of communicating with each other. However, communication between different clusters in the constellation is assumed to be impossible.

The design approach for this system, thus, has two parts. First, the constellation is designed using simplified assumptions about each cluster. Then the individual clusters are synthesized about the nodes of the constellation, or *formation centers.* This approach reduces the dimensionality of each step in the design process.

1.3 Thesis Objectives

The main objective of this thesis project is to provide initial insight into the use of a cluster of microsatellites for space-based tracking missions. A cluster of microsatellites is designed, implemented in simulation, and analyzed to achieve this object. While there are several technical issues that would have to be considered to completely design a target tracking cluster of microsatellites such as target camera sensor and communication technology, this research focuses primarily on the orbital design and control of the cluster. This research aims to identify how the relative motion of the satellites in a cluster affect target tracking accuracy. In addition, some control issues are identified and techniques to minimize cluster-wide fuel consumption are studied.

The necessary background for this research is provided in Chapter 2. This chapter begins with a brief introduction to the fundamentals of astrodynamics and leads into current techniques used to model satellite relative motion. Background for optimal measurement methods and principles are also provided. These techniques were originally established in the scientific community for optimal sensor placement and is an attractive approach to designing a cluster for target tracking missions.

The constellation design is provided in Chapter 3. The primary objective of the constellation is to provide a centroid, or formation center, orbit about which a cluster can be designed. In this study, the formation center is defined as a node of a Walker delta pattern constellation, which is designed using optimal observation techniques to provide 24 hour coverage of the perceived occupancy corridor. This chapter provides insight into optimal orbits that a cluster may be designed and identifies a cluster's tracking capability for a target in the occupancy corridor.

The cluster design problem is first considered in Chapter 4. The clusters are formulated about a formation center from the constellation and are synthesized using optimization techniques to minimize the average model-based value for the target position estimation error covariance. The research presented in this chapter focuses on the geometric properties of the cluster such as cluster baseline size (maximum allowable satellite separation) and assemblage size (number of microsatellites in the cluster). The objective of this research component is to provide insight into how cluster baseline size and assemblage size affect target tracking accuracy. Intuitively, larger cluster baseline size and assemblage size should provide better mission performance. Findings from this chapter suggest that cluster baseline size is more important to tracking accuracy than cluster assemblage size. Conversely, clusters with more satellites do improve convergence speed of target state estimation error. The research in this chapter also investigates a methodology to design a target tracking cluster that exhibits minimal relative satellite drift due to the major gravitational disturbance (J_2). Design results show that relative satellite drift can be reduced by several orders of magnitude while having little to no effect on predicted target tracking accuracy.

A shortcoming of the design approach taken in Chapter 4 is that the occupancy corridor must be accurately known. This is rarely possible, such as for debris identification or rogue satellite tracking. The occupancy corridor may be widely dispersed or there may be little to no information as to where the target may be at any time. Thus, the objective in Chapter 5 is to derive a heuristic for cluster design given that the target may be in any direction at any point in time relative to the cluster. An analytic derivation from optimal measurement methods shows that maximizing the average *tetrahedral volume* of a four satellite cluster is a good (i.e., robust) heuristic for cluster design that provides a robust viewing geometry for a target in any direction. This chapter also extends the heuristic to clusters with more than four satellites.

Cluster maintenance techniques are explored in Chapter 6. An MPC approach is studied that admits reconfiguration orbits once every five orbits to maintain cluster target tracking capability while minimizing fuel consumption. Results in this chapter confirm the importance of designing a tracking cluster with minimal J_2-induced relative drift even when the control algorithm allows drift to occur. In addition, techniques to minimize fuel consumption by accounting for unmodeled disturbances are investigated.

Chapter 7 presents a high-fidelity simulation that compares the different cluster design approaches studied in this thesis. Optimal measurement methods and techniques were first used to design a cluster of target tracking microsatellites in Chapters 3 and 4. Afterwards, Chapters 5 and 6 investigated a simpler heuristic for cluster design and a maintenance algorithm that allowed relative satellite drift to occur without hindering tracking capability. A 30 day, high-fidelity simulation with over 400 target tracking engagements compares these two approaches. Results from this simulation emphasize that maximizing the average tetrahedral volume and allowing relative satellite drift to occur are acceptable and robust approaches to cluster design and control.

Finally, the major conclusions of this thesis work are again presented in Chapter 8. This chapter discusses several issues for designing and implementing a space-based target tracking cluster of microsatellites. Several possible research directions are also provided for readers interested in expanding on this thesis work.

THIS PAGE INTENTIONALLY LEFT BLANK

Chapter 2

Background

The purpose of this chapter is to provide the fundamental background necessary for this thesis project. This chapter begins with the two-body equations of relative motion for a central gravitational field and follows with a description of Kepler's equations and orbital elements used to model satellite motion about the Earth. The Lagrangian coefficients transition matrix of an orbiting body in Cartesian coordinates is then presented. This matrix is necessary for propagating a target in the *occupancy corridor* described in Chapter 3. Perturbational theory and the dynamic model used to describe satellite relative motion are then provided. This chapter also discusses the theory of optimal measurement methods, which is critical for both constellation design in Chapter 3 and cluster design components in Chapters 4 and 5. The measurement and information matrices for a camera-based target tracking system are also identified. The last part of this chapter describes a high-fidelity simulation used throughout this thesis to simulate target tracking engagements.

2.1 Orbital Mechanics

The two-body, nonlinear equation of motion for a body in a gravitational field is

$$\begin{aligned} \frac{d^2}{dt}\mathbf{r} + \frac{\mu}{\mathbf{r}^3}\mathbf{r} &= 0 \\ \mathbf{v} &= \frac{d}{dt}\mathbf{r} \end{aligned} \tag{2.1}$$

In this equation, $\mu = G(m_1 + m_2)$ where m_1 and m_2 are the masses of the two point-mass bodies and G is the gravitational constant (6.6742×10^{-11} m^{3}s^{-2}kg^{-2}). For satellites

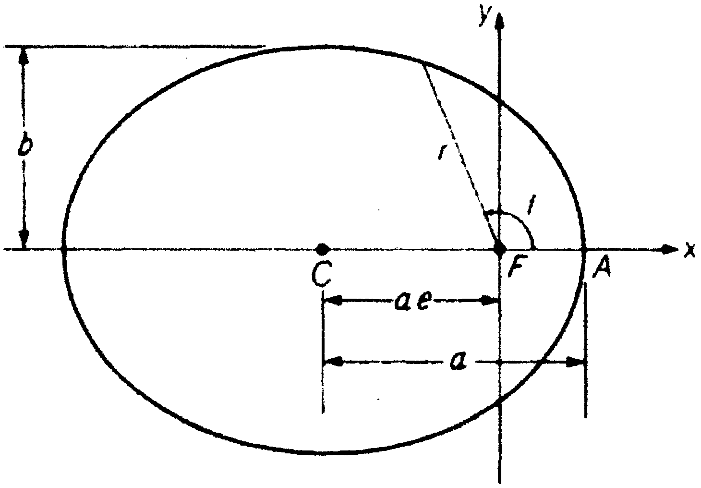

Figure 2-1: The ellipse traced by an orbiting body [3].

orbiting the Earth, the mass of a satellite is dropped since it is much smaller than the mass of the Earth and $\mu = 3.986005 \times 10^{14}$ m^{3}s^{-2}. The vector $\mathbf{r}$ represents the position vector from one body to the other and $\mathbf{v}$ is the relative velocity vector.

2.1.1 Kepler's Equations and Orbital Elements

While Eqn. 2.1 is nonlinear, it has an analytic solution with many interesting properties. Several of these important properties were discovered by Johannes Kepler in the beginning of 17th century and carry his name.

Kepler's second law, Eqn. 2.2, simply states that the massless angular momentum ($\mathbf{h}$) of an orbiting body is constant. This law has two important consequences: first, it requires that all unperturbed relative motion lies in a plane; second, the law demonstrates that the relative position vector r sweeps out equal areas in equal periods of time.

$$\mathbf{h} = \mathbf{r} \times \mathbf{v} = \text{constant} \tag{2.2}$$

Kepler's first law defines the path of an orbiting body (see Fig. 2-1). Kepler discovered that an orbiting body follows an ellipse with the central body at one focus (F)

$$r = \frac{p}{1 + e\cos f} \tag{2.3}$$

$$\text{where: } p \equiv \frac{h^2}{\mu} \tag{2.4}$$

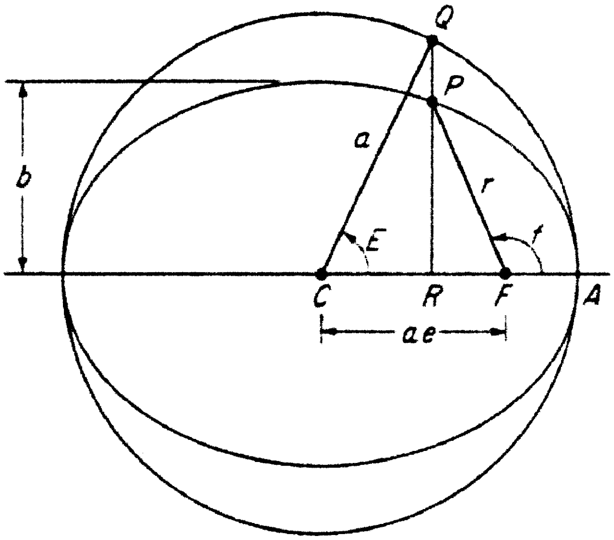

Figure 2-2: Eccentric anomaly [3].

The radial component r and the true anomaly f are defined in Fig. 2-1. The eccentricity e is a non-dimensional constant that describes the shape of the orbit. A circle corresponds to $e = 0$, while $0 < e < 1$ correspond to different ellipses. A parabola has $e = 1$ and hyperbolas correspond to $e \geq 1$. The semi-latus rectum p is also related to the semimajor axis a by the relationship $p = a(1 - e^2)$.

Kepler's third law states that the square of the orbital period of an orbiting body is proportional to the cube of the semimajor axis

$$P = 2\pi\sqrt{\frac{a^3}{\mu}} \tag{2.5}$$

This result is often used to describe the mean motion n of an orbital body

$$n = \frac{2\pi}{P} = \sqrt{\frac{\mu}{a^3}} \tag{2.6}$$

Kepler's equation are useful for describing relative motion in the orbital plane. However, while the true anomaly represents the angular position of the body, it does not advance about the ellipse at a uniform rate. Consider Fig. 2-2 with the relationship

$$r = a(1 - e\cos E) \tag{2.7}$$

and E is the eccentric anomaly. A direct relationship between the eccentric anomaly and

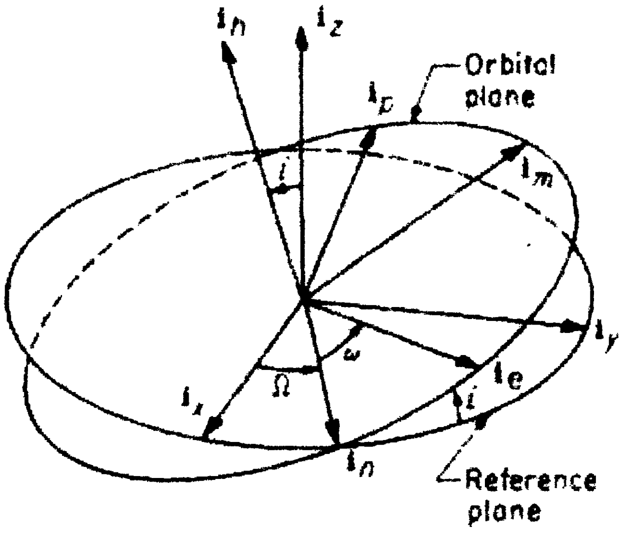

Figure 2-3: The 3-1-3 Euler angles [3].

true anomaly can be found using trigonometric identities such that

$$\tan \frac{1}{2} f = \sqrt{\frac{1+e}{1-e}} \tan \frac{1}{2} E \tag{2.8}$$

Finally, by defining the mean anomaly M

$$M = E - e \sin E \tag{2.9}$$

an orbital parameter is found whose rate of change is non-varying

$$M = M_0 + n(t - t_0) \tag{2.10}$$

Now that the necessary components to define an orbital ellipse in a plane have been presented, the last component needed to fully define an orbiting body is the orientation of the ellipse in three-dimensional Cartesian space. This thesis makes use of the standard 3-1-3 Euler rotations that correspond to the right ascension of the ascending node Ω, the orbital plane inclination i and the argument of perigee ω. The Euler angles are defined in Fig. 2-3.

2.1.2 The Lagrangian Coefficients Transition Matrix

While the two-body orbital equations of motion are nonlinear, a transition matrix exists that can propagate position and velocity vectors. The transition matrix in Eqn. 2.11 provides an easier and more convenient propagation methodology in many applications [3].

$$\begin{bmatrix} \mathbf{r} \\ \mathbf{v} \end{bmatrix} = \Phi \begin{bmatrix} \mathbf{r_0} \\ \mathbf{v_0} \end{bmatrix} \quad \text{where } \Phi = \begin{bmatrix} K & L \\ K_t & L_t \end{bmatrix} \tag{2.11}$$

The matrix elements are the Lagrangian coefficients in Eqn. 2.12 and have the property that K_t and L_t are time derivatives of K and L.

$$K = 1 - \frac{r}{p}(1 - \cos\theta) \tag{2.12a}$$

$$L = \frac{r r_0}{\sqrt{\mu p}} \sin\theta \tag{2.12b}$$

$$K_t = \frac{\sqrt{\mu}}{r_0 p}\left[\sigma_0(1 - \cos\theta) - \sqrt{p}\sin\theta\right] \tag{2.12c}$$

$$L_t = 1 - \frac{r_0}{p}(1 - \cos\theta) \tag{2.12d}$$

$$\text{where:} \quad \frac{r}{r_0} = \frac{p}{r_0 + (p - r_0)\cos\theta - \sqrt{p}\sigma_0 \sin\theta}$$

$$\theta = f - f_0$$

$$\sigma_0 = \frac{\mathbf{r_0} \cdot \mathbf{v_0}}{\sqrt{\mu}}$$

This thesis utilizes the Cartesian linearized state transition matrix for propagating target position measurements.

2.1.3 Variation of Parameters Theory

This chapter so far has only considered simple, two-body orbital motion. In an ideal world orbital motion would follow these dynamics. In reality, however, there are several forces intrinsic and extrinsic to the model that cause perturbations in orbital motion such as small gravitational forces from the Sun and the Moon, as well as atmospheric drag and solar wind. An important consideration, particularly for this thesis work, is the gravitational perturbation due to the Earth's oblateness. For satellites in LEO, this last perturbation to Kepler's equations dominates all others.

Variation of parameter theory is useful for studying perturbational forces on orbital motion. The method of studying variation of parameters developed by Joseph-Louis Lagrange provides some of the best insight and ability to model disturbing forces. Consider the two-body equation of motion augmented with a general disturbing function **R**

$$\frac{d^2}{dt}\mathbf{r} + \frac{\mu}{r^3}\mathbf{r} = \left[\frac{\delta \mathbf{R}}{\delta \mathbf{r}}\right]^T \tag{2.13}$$

Lagrange derived the time derivatives of the standard orbital element set $(a, e, i, \Omega, \omega, M)^T$ as a function of the disturbing function where $b^2 = a^2(1 - e^2)$ [3]

$$\frac{da}{dt} = \frac{2}{na}\frac{\delta R}{\delta M_0} \tag{2.14a}$$

$$\frac{de}{dt} = -\frac{b}{na^3 e}\frac{\delta R}{\delta \omega} + \frac{b^2}{na^4 e}\frac{\delta R}{\delta M_0} \tag{2.14b}$$

$$\frac{di}{dt} = -\frac{1}{nab\sin i}\frac{\delta R}{\delta \Omega} + \frac{\cos i}{nab\sin i}\frac{\delta R}{\delta \omega} \tag{2.14c}$$

$$\frac{d\Omega}{dt} = \frac{1}{nab\sin i}\frac{\delta R}{\delta i} \tag{2.14d}$$

$$\frac{d\omega}{dt} = -\frac{\cos i}{nab\sin i}\frac{\delta R}{\delta i} + \frac{b}{na^3 e}\frac{\delta R}{\delta e} \tag{2.14e}$$

$$\frac{dM_0}{dt} = -\frac{2}{na}\frac{\delta R}{\delta a} - \frac{b^2}{na^4 e}\frac{\delta R}{\delta e} \tag{2.14f}$$

These equations have led to several advances in modeling orbital motion such as providing the ability to accurately model and predict the effect of gravitational harmonics without requiring numerical integration.

Earth Oblateness Perturbational Effects

The Earth is an oblate spheroid (i.e., it is slightly flattened on at the poles). While there are several order gravity perturbation terms necessary to completely model the Earth's oblateness effects on satellite motion (i.e., J_2, J_3, J_5), only J_2 is considered in this study because it is several orders of magnitude greater than the next most significant. The time average, mean value of disturbing function due to the J_2 disturbance is

$$\bar{R} = \frac{n^2 J_2 r_{eq}^2}{4(1 - e^2)^{3/2}}(2 - 3\sin^2 i) \tag{2.15}$$

In this research, the coefficient $J_2 = 0.0010826$ is used and the equatorial radius of the Earth is modeled as $r_{eq} = 6,378,145$ m. The average rates of change of all standard orbital elements can easily be calculated using the differential equations derived by Lagrange in Eqn. 2.14

$$
\begin{aligned}
\frac{d\bar{\Omega}}{dt} &= -\frac{3}{2}J_2 n \left(\frac{r_{eq}}{p}\right)^2 \cos i && \text{(2.16a)}\\
\frac{d\bar{\omega}}{dt} &= \frac{3}{4}J_2 n \left(\frac{r_{eq}}{p}\right)^2 (5\cos^2 i - 1) && \text{(2.16b)}\\
\frac{d\bar{M}_0}{dt} &= \frac{3}{4}J_2 n \left(\frac{r_{eq}}{p}\right)^2 \sqrt{1-e^2}(3\cos^2 i - 1) && \text{(2.16c)}
\end{aligned}
$$

The remaining orbital elements (a, e, i) do not have mean variations due to the J_2 gravitational harmonic.

Gauss' Variational Equations

Gauss' variational equations provide a similar approach to modeling orbital disturbances. The equations for the standard orbital elements are a function of general acceleration disturbances in the osculating radial, tangential, and orthogonal directions of the orbiting body (see Eqn. 2.17). Gauss' form is useful for modeling disturbances such as drag and self-imposed forces such as thruster firings.

$$
\frac{d}{dt}\begin{bmatrix} a \\ e \\ i \\ \Omega \\ \omega \\ M \end{bmatrix} = \begin{bmatrix} 0 \\ 0 \\ 0 \\ 0 \\ 0 \\ n \end{bmatrix} + \begin{bmatrix} \frac{2a^2}{h} e \sin f & \frac{2a^2 p}{hr} & 0 \\ \frac{1}{h} p \sin f & \frac{(p+r)\cos f + re}{h} & 0 \\ 0 & 0 & \frac{r\cos\theta}{h} \\ 0 & 0 & \frac{r\sin\theta}{h\sin i} \\ \frac{-p\cos f}{he} & \frac{(p+r)\sin f}{he} & \frac{-r\sin\theta\cos i}{h\sin i} \\ \frac{b}{ahe}(p\cos f - 2re) & \frac{-b}{ahe}(p+r)\sin f & 0 \end{bmatrix} \begin{bmatrix} a_r \\ a_\theta \\ a_h \end{bmatrix} \tag{2.17}
$$

Nonsingular Variational Equations

A shortcoming of modeling satellite orbital motion with the standard orbital elements occurs for orbits with small eccentricities or inclinations. The argument of perigee and mean anomaly are undefined when the eccentricity of an orbiting body is zero. Similarly, zero eccentricity causes singularities in Gauss' variational equations. The right ascension of the ascending node (Ω) is undefined when a body is in a zero inclination orbit and a singularity in Gauss' variational equations exists due to $1/\sin i$ terms.

As is such, many equinoctial (or nonsingular) orbital elements have been derived that do not exhibit singularities at these important orbits. For this thesis, the equinoctial orbital elements defined by $(a, \theta, i, q_1, q_2, \Omega)$ are used where $\theta = \omega + f$, $q_1 = e\cos\omega$ and $q_2 = e\sin\omega$. These orbital elements are valid for both circular and highly eccentric orbits; however, the singularity due to zero inclination still persists. The nonsingular variational equations are

$$\frac{d}{dt}\begin{bmatrix} a \\ \theta \\ i \\ q_1 \\ q_2 \\ \Omega \end{bmatrix} = \begin{bmatrix} 0 \\ \frac{h}{r^2} \\ 0 \\ 0 \\ 0 \\ 0 \end{bmatrix} + \begin{bmatrix} \frac{2a^2(q_1\sin\theta - q_2\cos\theta)}{h} & \frac{2a^2p}{hr} & 0 \\ 0 & 0 & \frac{r\sin\theta\ \arctan i}{h} \\ 0 & 0 & \frac{r\cos\theta}{h} \\ \frac{p\cos\theta}{h} & \frac{(p+r)\cos\theta + r\,q_1}{h} & \frac{r\,q_2\sin\theta\ \arctan i}{h} \\ -\frac{p\cos\theta}{h} & \frac{(p+r)\sin\theta + r\,q_2}{h} & -\frac{r\,q_1\sin\theta\ \arctan i}{h} \\ 0 & 0 & \frac{r\sin\theta}{h\sin i} \end{bmatrix} \begin{bmatrix} a_r \\ a_\theta \\ a_h \end{bmatrix} \tag{2.18}$$

The term for argument of latitude is provided in Ref. [3]. The variational equations for q_1 and q_2 are found by differentiating to obtain

$$\frac{dq_1}{dt} = -e\sin\omega\frac{d\omega}{dt} + \cos\omega\frac{de}{dt} \tag{2.19}$$

$$\frac{dq_2}{dt} = e\cos\omega\frac{d\omega}{dt} + \sin\omega\frac{de}{dt} \tag{2.20}$$

and using the previous variational equations for e and ω. These equations are simplified using trigonometric identities similar to those used by Battin [3] to derive a similar equinoctial orbital element set.

2.2 Modeling Relative Satellite Motion

Researchers have recently studied satellite relative motion models because of current interest in *formation flying* and rendezvous missions. Initial research focused on the Hills equations, which are only applicable for nearly circular orbits. Later, Gauss' variational equations were used because they are accurate for eccentric orbits [33].

Further work has taken into account disturbances such as drag and gravity perturbations due to the Earth's oblateness. In this thesis, only the major gravity perturbation (J_2) is used in modeling satellite relative motion. There are secular (mean and long period) J_2 effects (see Eqns. 2.16a- 2.16c) as well as osculating (short period oscillatory) ones that have both been accurately identified. Researchers have taken several approaches to incorporate J_2 disturbances into relative satellite motion models. For example, Ref. [32] modified the Clohessy-Wiltshire equations to provide an analytic solution for satellite relative motion that accounted for J_2 effects.

This thesis utilizes the linearized state transition matrix developed in Ref. [14] for modeling satellite relative motion. Consistent with Gaussian variational equation literature, the relative satellite motion dynamics are propagated in the equinoctial orbital element set defined by $\mathbf{e} = (a, \theta, i, q_1, q_2, \Omega)^T$. Ref. [14] defines $\delta\mathbf{e_i} = \mathbf{e_i} - \mathbf{e_{fc}}$ (where i represents the i^{th} satellite and fc is the *formation center*). The state transition matrix to propagate the relative dynamics of satellite i with respect to the formation center is given by the analytic solution to Eqn. 2.21.

$$\delta\mathbf{e_{mean}}(t) = \phi_e(t, t_o)\delta\mathbf{e_{mean}}(t_o) \tag{2.21}$$

This transition matrix takes into account the secular J_2 effects.

The osculating components of relative motion are modeled from the mean components with the transformation

$$\delta\mathbf{e_{osc}}(t) = D(t)\delta\mathbf{e_{mean}}(t) \tag{2.22}$$

This transformation matrix converts relative mean orbital elements into relative osculating orbital elements and is a linear approximation of the theory developed by Brouwer and Lyddane [9, 21]. Finally, the analytic solution to Eqn. 2.23 is a transformation from the relative mean orbital element set into Cartesian coordinates, $\mathbf{X} = (x, y, z, v_x, v_y, v_z)^T$, defined about the formation center in Fig. 2-4. A slightly different transformation is used to convert relative osculating orbital elements into relative Cartesian elements (see Eqn. 2.24).

$$\begin{aligned} \mathbf{X_{mean}}(t) &= \{\bar{A}(t) + \alpha\bar{B}(t)\}\delta\mathbf{e_{mean}}(t) && (2.23) \\ \mathbf{X_{osc}}(t) &= \{A(t) + \alpha B(t)\}D(t)\delta\mathbf{e_{mean}}(t) && (2.24) \\ \text{where: } \alpha &= 3J_2 r_{eq}^2 \end{aligned}$$

The parameter-varying state transition matrices, despite being a linear approximation, are extremely accurate for small time steps. They can model both the secular and osculating J_2 effects on relative satellite motion. In this study, however, only the secular effects are modeled since long term relative satellite motion is considered. A singularity in the

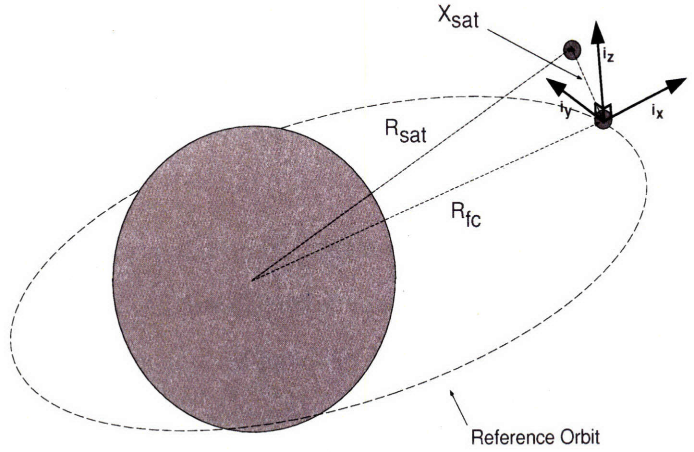

Figure 2-4: Cartesian coordinate frame $(\mathbf{i_x}, \mathbf{i_y}, \mathbf{i_y})$ defined about the formation center.

transformation matrix from secular to osculating orbital elements at critical inclination also prevents modeling of the osculating relative motion at critically inclined orbits.

2.3 Optimal Measurement Methods

Optimum experimental design theory is a major existing method for locating sensors to minimize the error covariance associated with a state being measured. In general, measurement systems (or sensor locations) are synthesized by trying to maximize "the goodness of parameter estimates in terms of the covariance matrix of the estimates [40]." This approach is complicated by constraints on sensors such as the range or number of sensors and knowledge about the system being measured. Thus, measurement systems often have to be designed with some simplifications and prior knowledge of the behavior of the state being measured [40].

Consider the general dynamic system in Eqn. 2.25. In this equation, $\mathbf{x}$ represents the state of the system and $F(x,t)$ is a Jacobian matrix that defines how the state changes with time (t). The vector $\mathbf{u}$ and matrix G are process noise inputs and $\mathbf{z}$ is the measurement of $\mathbf{x}$ in Eqn. 2.26. For this notation, y is some parameter or variable of the measurement matrix H (i.e., sensor placement) and $\mathbf{v}$ is the sensor noise model.

$$\dot{\mathbf{x}} = F(\mathbf{x},t)\mathbf{x} + G\mathbf{u} \tag{2.25}$$

$$\mathbf{z} = H(\mathbf{x},y,t)\mathbf{x} + \mathbf{v} \tag{2.26}$$

For these equations the noise models of the system are assumed to be Gaussian white noise

$$\begin{aligned} E[\mathbf{u}(t)\mathbf{u}^T(\tau)] &= Q\delta(t-\tau) && (2.27)\\ E[\mathbf{v}(t)\mathbf{v}^T(\tau)] &= R\delta(t-\tau) && (2.28)\\ E[\mathbf{u}(t)\mathbf{v}^T(\tau)] &= 0 && (2.29) \end{aligned}$$

Finally, the error covariance for the estimated state vector ($\hat{\mathbf{x}}$) is the covariance matrix

$$P(t) = E[(\mathbf{x}(t) - \hat{\mathbf{x}}(t))(\mathbf{x}(t) - \hat{\mathbf{x}}(t))^T] \tag{2.30}$$

The goal of designing an observing system is to provide the best possible estimate of the state $\mathbf{x}$. Simply, an optimal approach to sensor design would be to choose the parameter(s) of H (y) that minimize the final error covariance of the state estimate given some *a priori* knowledge of the system behavior

$$J = \min_{y} \; P(t_f) \tag{2.31}$$

The final covariance does not require that the actually measurements be known. In fact, $P(t_f)$ can be determined by integrating the matrix Riccati equation and is a function of the dynamics of the system and the noise models

$$P(t_f) = \int_{t_0}^{t_f} \left(FP + PF^T - PH^TR^{-1}HP + GQG^T\right)\, dt \tag{2.32}$$

Posing the covariance matrix as an optimization problem is extremely difficult, though, because the Riccati equation is a nonlinear differential equation. However, the Cramér-Rao inequality provides a relationship between the covariance of a system and the information of that system that lends itself to a set of equations that is easier to manipulate for optimal sensor design. Assuming that R^{-1} in Eqn. 2.28 is a diagonal matrix such that it can be written as $\frac{1}{\sigma^2}I$, then the information matrix is

$$\begin{aligned} M &= \frac{1}{\sigma^2}\int_{t_0}^{t_f} H^T H dt = \sum_{i=1}^{N} M_i && (2.33)\\ \text{where: } M_i &= \frac{1}{\sigma^2}\int_{t_0}^{t_f} h_i^T h_i dt \end{aligned}$$

The h_i vectors are the individual measurements from each of the sensors ($i = 1, \ldots, N$) at time t such that $H^T = [h_1^T, h_2^T, \ldots, h_N^T]$. This property makes the information matrix very useful for sensor placement design problems. The information matrix is the sum of all the individual measurements and their correlated information matrices. The Cramér-Rao inequality states that the inverse of the information matrix is less than or equal to the covariance matrix

$$||M^{-1}|| \leq ||P|| \tag{2.34}$$

The Cramér-Rao inequality provides a lower bound on the covariance of the state being estimated. Previous work on optimal measurement methods have successfully used the information matrix as a figure-of-merit for solving sensor placement problems [40].

Given the Cramér-Rao inequality, an optimal approach to the sensor placement problem is to maximize the information of the state being measured

$$J = \max_{y} M(t_f) \tag{2.35}$$

Thus, the information matrix is sought that satisfies the relationship: $M^\star \succeq M$, $\forall M$. However, a mapping from the n-dimensional information matrix to a one-dimension performance or optimization metric is required for standard optimization techniques. Several standard criterions exist that map the information matrix into one-dimension (f : $\Re^n \rightarrow \Re^1$). Some of the most common ones follow.

The D-optimality criterion is the natural log of the determinant of the information matrix [40]

$$J = \min \; -\ln(\det(M)) \tag{2.36}$$

Minimizing the determinant of the information matrix results in an optimal solution that provides the minimum volume of the uncertainty ellipsoid for the state estimates.

The A-optimality criterion is the trace of the inverse of the information matrix [40]

$$J = \min \; tr(M^{-1}) \tag{2.37}$$

This criterion provides an optimal solution that minimizes the average axis length of the uncertainty ellipsoid.

The E-optimality criterion is defined by the maximum eigenvalue of the inverse of the information matrix [40]

$$J = \min\ \lambda_{max}(M^{-1}) \tag{2.38}$$

This optimal criteria provides a solution with the smallest length of the largest axis of the uncertainty ellipsoid

The sensitivity criterion maximizes the average of the eigenvalues of the information matrix [22]

$$J = \min\ -tr(M) \tag{2.39}$$

This criterion is often used because of its ease in computing. However, in some circumstances this method could lead to a singular value such that the information matrix is not invertible.

For this thesis, the A-optimality criterion is used because of its similarity to the standard norm (i.e., the trace) of the error covariance matrix used in Kalman filtering.

2.3.1 Measurement Over a Trajectory

The information matrix propagation equations for discrete measurement systems are similar to those used to propagate the alternative form of the discrete Kalman filter [10]

$$\begin{aligned} P_k^{-1} &= (P_k^-)^{-1} + H_k^T R_k^{-1} H_k && (2.40) \\ P_{k+1}^- &= \Phi_k P_k \Phi_k^T + Q_k && (2.41) \end{aligned}$$

The lower bound, provided by information matrix and due to the Cramér-Rao inequality, is impacted by dropping the process noise component Q_k and assuming that ${R_k}^{-1}$ can be written as $\frac{1}{\sigma^2}I$. Thus, the propagation equation for the information matrix is

$$M_{k+1} = (\Phi_k^T)^{-1} M_k (\Phi_k)^{-1} + \frac{1}{\sigma^2}(\Phi_k^T)^{-1} H_k^T H_k (\Phi_k)^{-1} \tag{2.42}$$

Repeating this process provides a discrete propagation formulation for the information matrix over an entire trajectory [40]

$$M(t_N) = \sum_{k=1}^{N} \left\{ \left(\prod_{i=N-1}^{k} (\Phi_i^T)^{-1} \right) \frac{1}{\sigma^2} H_k^T H_k \left(\prod_{i=k}^{N-1} (\Phi_i)^{-1} \right) \right\} \tag{2.43}$$

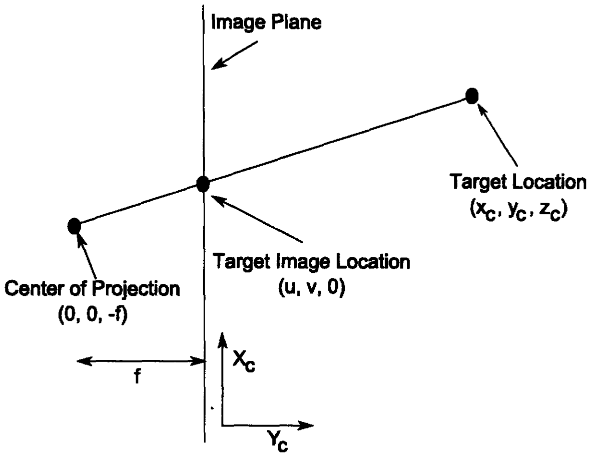

Figure 2-5: Targeting camera model [2].

This equation, by the Cramér-Rao inequality, provides a lower bound for the target state vector covariance where Φ_i is the transition matrix for the process being observed.

2.3.2 Targeting Camera Model

In this study, a target camera is used to provide pointing vector measurement to the target (see Fig. 2-5). Each camera provides information of the target position in the plane orthogonal to the pointing vector since measurements are taken on an image plan. The camera measurement matrix is a nonlinear function that includes a coordinate frame transformation and a projection onto the camera image plane. The target position in the camera coordinate frame relative to the center of the camera image plane is given by [1]

$$\begin{bmatrix} x_c \\ y_c \\ z_c \end{bmatrix} = \begin{bmatrix} t_x \\ t_y \\ t_z \end{bmatrix} + RM \begin{bmatrix} x \\ y \\ z \end{bmatrix} \tag{2.44}$$

where RM is the rotation matrix from the global Cartesian coordinate frame into the camera coordinate frame. The vector $(t_x, t_y, t_z)^T$ is a translational shift the accounts for the relative positions of the origins in the global Cartesian and camera coordinate frames. The target image location $(u, v)^T$ in the X_c and Y_c directions is then [1]

$$\mathbf{y} = \begin{bmatrix} u \\ v \end{bmatrix} = \frac{1}{1+\beta z_c} \begin{bmatrix} x_c \\ y_c \end{bmatrix} \tag{2.45}$$

and β is the inverse of the camera focal length (f). To simplify this equation, the assumption is made that the targeting camera is pointing directly at the target. This assumption is useful because the translational component $(t_x, t_y, t_z)^T$ from the coordinate transformation equation falls out and z_c is simply the Euclidean distance from the tracking satellite to the target. The measurement matrix H can be approximated by observing that the measurements u and v provide information of the target position in the plane orthogonal to the pointing vector $\mathbf{v} = (x, y, z)^T$. The measurement matrix is

$$H = \frac{1}{1 + \beta|\mathbf{v}|} \begin{bmatrix} x_1 & y_1 & z_1 \\ x_2 & y_2 & z_2 \end{bmatrix} \tag{2.46}$$

where (x_1, y_1, z_1) and (x_2, y_2, z_2) are unit vectors orthogonal to each other and to $\mathbf{v}$.

The information matrix for a target's position due to a single pointing vector measurement (assuming that R can be diagonalized) is then

$$\begin{aligned} H^t R^{-1} H &= \frac{1}{\sigma^2} H^t H && (2.47) \\ &= \frac{1}{\sigma^2(1 + \beta|\mathbf{v}|)^2} \left[I - \frac{\mathbf{v} \cdot \mathbf{v^T}}{\mathbf{v^T} \cdot \mathbf{v}} \right] && (2.48) \end{aligned}$$

Two observations can be made from this information matrix. First, the closer a satellite is to the target, the better the target position estimate. This observation is driven by the $|\mathbf{v}|$ term on the bottom of Eqn. 2.48. Second, the matrix component on the top of Eqn. 2.48 dictates that satellite targeting camera separation is important. The measurement system is very similar to a triangulation system. Thus, having two sensors on top of each other, or very close to each other, reduces the information matrix (see Fig. 2-6).

2.4 Simulation Design

A high-fidelity simulation testbed was developed in Simulink® to analyze cluster target tracking performance. The microsatellites in the cluster are propagated with a J_2 gravitational model and are modeled with GPS and IMU sensors to estimate their own positions, velocities and attitudes. In addition, a targeting camera on each satellite provides line-of-sight vector measurements to the target. On-board satellite sensors are modeled with 1st-order Markov and random noise models in the simulation (see Table 2.1). These noise

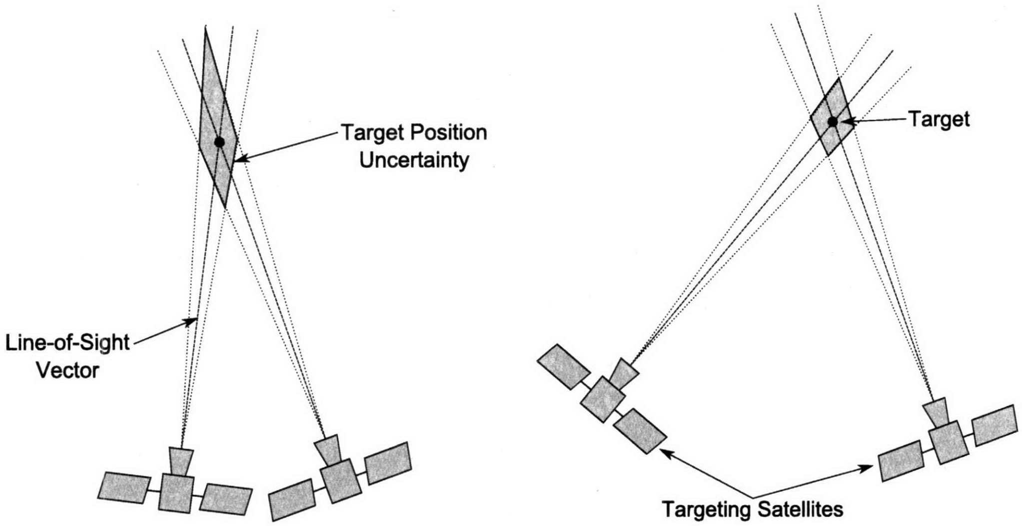

(a) Poor cluster geometry. (b) Good cluster geometry.

Figure 2-6: Simple examples of two satellite clusters tracking a target. The cluster with greater satellite separation can more accurately estimate the target position.

Table 2.1: Microsatellite sensor 1st-order Markov and random noise models used in the simulation.

Sensor	1-Sigma Dispersion Value	Correlation Time	Random Noise
GPS Receiver	30 m	200 sec	3 m
IMU	50.0^{-6} rad	50 sec	n/a
Targeting Camera	50.0^{-6} rad	100 sec	20.0^{-6} rad

models are added directly to the true nonlinear dynamics and a centralized extended Kalman filter running at 1 Hz is utilized to estimate the target's state vector. Each satellite takes a target line-of-sight measurement once every 16 seconds and all measurements occur at least 2 seconds apart. In the simulation, the target measurement provides an angular direction from the satellite to the target. The simulation begins when the cluster of microsatellites is given a cue to the target's estimated initial position and velocity and the satellites slew their tracking cameras toward the target to begin taking line-of-sight vector measurements until the end of the target's modeled trajectory. In this simulation, neither the true target nor the target model in the Kalman filter include J_2 gravitational effects.

The covariance matrix is propagated in the simulation using the well known discrete

Kalman filter recursive equations

$$P_k = P_k^- - P_k^- H_k^T (H_k P_k^- H_k^T + R_k)^{-1} H_k P_k^- \tag{2.49}$$

$$P_{k+1}^- = \Phi_k P_k \Phi_k^T + Q_k \tag{2.50}$$

where P_k is the error covariance matrix, H_k is the measurement matrix, R_k and Q_k are the measurement error and process noise covariance matrices, and Φ_k is the usual state transition matrix [10]. The Kalman filter recursive equations include process noise and error profiles for all GPS, IMU and camera sensors.

Throughout this thesis, two target tracking results are reported from the simulation data. The true target position error (denoted as $|x_p - \hat{x}_p|$) is the average position error during the last 200 seconds of the target's trajectory. The estimated target position error (denoted as $\sqrt{\mathrm{E}[(x_p - \hat{x}_p)(x_p - \hat{x}_p^T]}$) is the standard deviation of the estimated target position error reported directly from the Kalman filter. This value is the root mean square of the estimated position error. Again, the average value over the last 200 seconds of an engagement is reported.

2.5 Chapter Summary

The purpose of this chapter was to provide the technical background necessary for this thesis. The chapter began with the two-body equations of motion and discussed perturbational theory. The relative satellite motion model and optimal measurement methods presented in this chapter are integral to the constellation and cluster design studies in Chapters 3 through 5. The simulation testbed is used throughout this thesis to analyze cluster tracking performance.

Part I

Orbit Determination

Chapter 3

Formulating the Formation Center

The primary object in this chapter is to choose a *formation center* about which a target tracking clusters can be designed. In order to achieve that object, this chapter describes an optimization approach to designing a *constellation of clusters* capable of providing 24 hour coverage of a perceived *occupancy corridor* and satisfying minimum tracking capability of a target in the corridor. The constellation design in this chapter is constrained to Walker delta patterns because of their design simplicity and the approach utilizes optimal measurement techniques to synthesis the constellation based on realistic target tracking sensor and satellite capabilities.

This chapter begins with a definition of the occupancy corridor and then presents constellation design constraints and approaches. Constellation design results are provided in Sec. 3.5. A constellation with four planes and six clusters per plane is chosen from the results in this chapter to provide tracking coverage because constellations with more clusters show diminished returns per additional cluster.

3.1 Definition of the Occupancy Corridor

Maintaining 24 hour coverage of an occupancy corridor is desired in this study. In previous studies, such as Ref. [27], the occupancy corridor has been defined as a volumetric tube that includes a wide dispersion of candidate target trajectories. For design simplicity purposes, the occupancy corridor considered in this study is a single suborbital trajectory with an expected launch and reentry point. The trajectory is representative of the centroid of a volumetric occupancy corridor and is a minimum energy trajectory that traverses one-

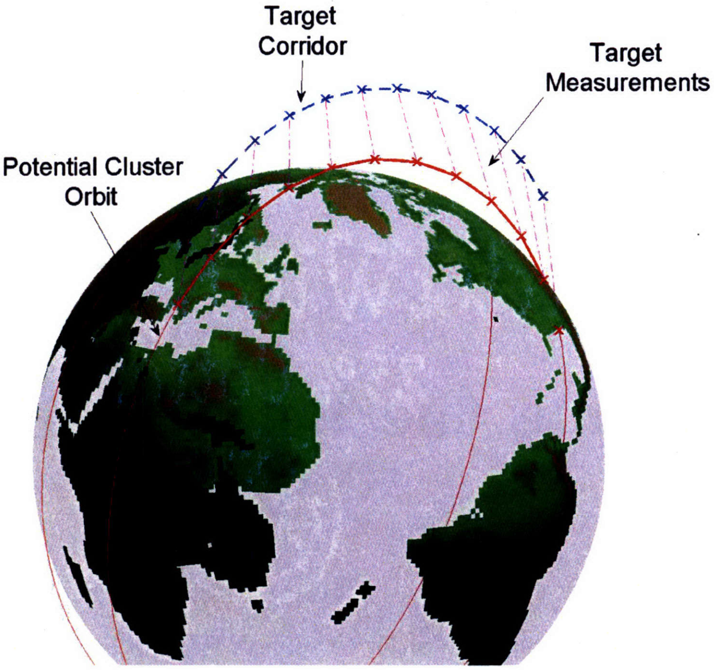

Figure 3-1: The target occupancy corridor and a candidate formation center, or node of the constellation, are plotted in the ECEF coordinate frame.

quarter of the Earth's circumference. Since the time of launch is unknown, the occupancy corridor is fixed in the Earth Centered, Earth Fixed (ECEF) coordinate frame and rotates with the Earth in the ECI reference frame (see Fig. 3-1). The target occupancy corridor is completely defined in Table 3.1, except for the right ascension, which is a function of the target's time of launch.

3.2 Constellation Design Approach

Walker delta pattern constellations are considered for this problem because of their symmetry and ease of design. Walker delta patterns are made up of T satellites, where S satellites are distributed about each of the P orbital planes of the constellation [42]. Thus, the planes are equally spaced around the equator and the satellites in each of the planes are evenly separated by their mean anomaly. The inclination and phase difference F between the planes completely define the constellation. A typical shorthand notation to describe a Walker delta pattern constellation is i:T/P/F [44] and an example of a 65°:15/5/1 constellation is provided in Fig. 3-2.

The reason for constraining the constellation design to Walker delta patterns is multi-

Table 3.1: Target occupancy corridor parameters. The occupancy corridor rotates with the ECEF reference frame.

Parameter	Value
a	5988 km
e	0.4142
i	63.0°
ω	270°
Ω	$\mathrm{f}(\mathrm{w_e t} + \mathrm{c})$
$f_{initial}$	135°
f_{final}	225°
Time of flight	2100 seconds

$*\ w_e = 0.250684454$ deg/min (angular rate of the Earth)

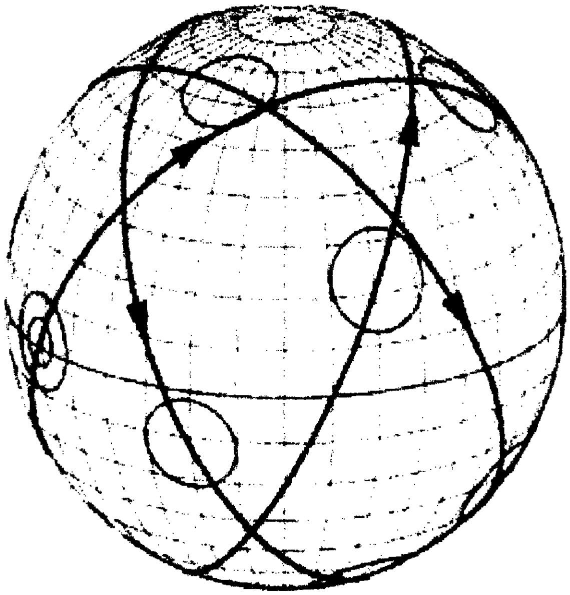

Figure 3-2: Example of a 65:15/5/1 Walker delta pattern [43]. The circles correspond to clusters at each node of the constellation.

Table 3.2: Design matrix for Walker delta patterns.

Number of Clusters (T)		Clusters per Plane (S)			
		5	6	7	8
Planes (P)	2	10	12	14	16
	3	15	18	21	24
	4	20	24	28	32
	5	25	30	35	40

fold. First, only one plane needs to be considered in the design process since the planes in the constellation are identical. For example, a constellation with four planes that repeats its ground track every 24 hours only requires that six hours of a single plane need to be considered to fully characterize the model-based tracking capability of the entire constellation. The coverage plateaus of the individual clusters in the constellation can also be easily identified with a Walker delta pattern. The number of planes in the constellation will provide insight into the number of sequential orbits a cluster is capable of tracking a target in the occupancy corridor. For example, if a constellation with four planes that completes 16 orbits per day provides acceptable coverage, then this result suggests that each target tracking cluster is capable of tracking a target in the occupancy corridor for four sequential orbits every day. Similarly, a combination of the orbital period of the constellation and number of satellites per plane provide insight into the viewing window that a cluster can track targets in the occupancy corridor during each orbital pass [44]. Results from the constellation design will also provide insight into number of clusters and orbital energy of the constellation necessary to provide adequate target tracking capability. The number of cluster should correspond well with principal implementation costs.

The number of planes and clusters per plane considered in the design process of this chapter are in Table 3.2. Only critical inclined ($i_{crit} \approx 63.43°$) and repeat ground track constellations are considered in this research for reasons to be described in Sec. 3.3. In addition, the planes of the constellation are assumed to be phased such that every plane/occupancy corridor relative engagement geometry is identical.

3.3 Constellation Design Considerations

This section presents constellation design considerations and constraints used in this study.

3.3.1 Altitude Constraints

The minimum allowable elevation is set to 400 km to ensure the constellation does not degrade quickly due to drag [11]. A maximum allowable elevation of 2500 km is used to keep the constellation in LEO. These constraints are satisfied with the following conditions on radius of perigee and apogee of the orbit

$$\frac{a(1-e^2)}{1+e} = r_p \geq r_{eq} + 400 \text{ km} \tag{3.1}$$

$$\frac{a(1-e^2)}{1-e} = r_a \leq r_{eq} + 2500 \text{ km} \tag{3.2}$$

3.3.2 Repeat Ground Track

A satellite in a repeat ground track orbit is one who's projection of the orbit on the Earth's surface repeats every n-integer days. The constellation design is constrained to simple repeat ground tracks so that only a small time period (less than three days) has to be considered while designing the constellation and the clusters. A repeat ground track is maintained by constraining the relative Keplerian period and ground track shift of the satellite to integers and simple fractions such as $\frac{29}{2}$.

A common approach in constellation design, that is utilized in this study, is to constrain the constellation to critical inclination ($i_{crit} = \arccos\sqrt{\frac{1}{5}} \approx 63.43°$) to ensure that the argument of perigee does not precess due to the J_2 gravitational harmonic. With the orbit critically inclined, the ground track shift of a satellite is a result of the rotation rate of the Earth (ω_e) and the nodal regression of the right ascension of the ascending node due to the Earth's oblateness. The ground track shift per orbit is [13]

$$S = \frac{2\pi}{\bar{n}}(w_e - \dot{\Omega}) \tag{3.3}$$

where $\dot{\Omega}$ was defined in Eqn. 2.16a and $\bar{n}$ is a result of Kepler's third law plus a correction due to the effect of J_2 on the mean anomaly of a satellite [13]

$$\bar{n} = \sqrt{\frac{\mu}{a^3}}\left[1 + \frac{3}{2}\frac{J_2 R_{eq}^2}{p^2}\left(1 - \frac{3}{2}\sin^2 i\right)\sqrt{1-e^2}\right] \tag{3.4}$$

The secular rate of the argument of perigee would also have to be considered in this equation if the orbit was not critically inclined. The ground track shift S gives the angular rotation of the ground track each orbit. Thus, the trace repetition parameter defined as $Q = \frac{2\pi}{S}$ (orbits/day) is constrained to integers and simple fractions.

3.3.3 Cluster Visibility of Target

A cluster, or node of the constellation, is assumed to be able to identify and track a target in the occupancy corridor when constraints on distance to target, satellite maximum angular rotation rates, and celestial background are met.

Range to Target

A maximum distance to the target of 5000 km is used to represent target tracking camera sensor limitations and a minimum distance of 200 km ensures that the target does not travel through the cluster.

Angular Rotation Rate

An important consideration for constellation design is the expected angular rates of the satellites in the cluster while keeping their target tracking cameras pointed at the target in the occupancy corridor (since microsatellites are considered in this study, the assumption is made that none of the sensors on the microsatellites are gimballed). A maximum allowable angular rate ensures that the star tracker on the satellite is able to accurately estimate the attitude of the satellite and thus the line-of-sight vector to the target. Only the angular rate of the formation center is considered by assuming that the distance of the satellites to the target is much larger than the distance of each of the satellites to the target. Thus, the angular constraint is

$$|w_{fc}| \leq 3\ ^{\circ}/\text{sec} \tag{3.5}$$

where $w_{fc} = (R_{tgt} - R_{fc}) \times (V_{tgt} - V_{fc}) = dR \times dV$ (see Fig. 3-3).

Celestial Background

The last condition is for the target to have a celestial background on the tracking camera's image plane so that the target discrimination algorithm can identify the target. The active constraint is that the Earth and the Earth's limb (i.e., the atmosphere) do not occlude the line-of-sight between the target and the tracking cluster. The following equations define the

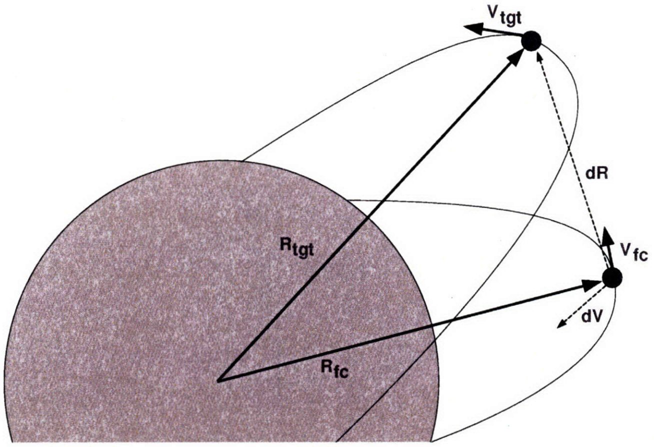

Figure 3-3: Angular rates of the microsatellites in a cluster are due to the satellites tracking the target.

central angles of the viewing geometry for the cluster and target relative geometry described in Fig. 3-4.

$$c_A = \arccos \frac{R_l}{R_{fc}} \tag{3.6a}$$

$$c_B = \arccos \frac{R_l}{R_{tgt}} \tag{3.6b}$$

$$c_1 = c_A - c_B \tag{3.6c}$$

$$c_2 = c_A + c_B \tag{3.6d}$$

When the central angle between the formation center and the target is greater than c_1 and less than c_2, then the viewing geometry satisfies the celestial background constraint and the cluster is assumed to be able to measure the line-of-sight vector to the target [13]. The position of the Sun may also have to be taken into account for actual implementation, but is not considered in this study.

3.4 Constellation Figure-of-Merit

The constellation figure-of-merit is the average model-based value for the target position estimation error covariance over one complete repeat ground track of the constellation. In this application, the clusters are assumed to be independent entities that cannot communicate between each other. Thus, the cluster that provides the minimum model-based tracking

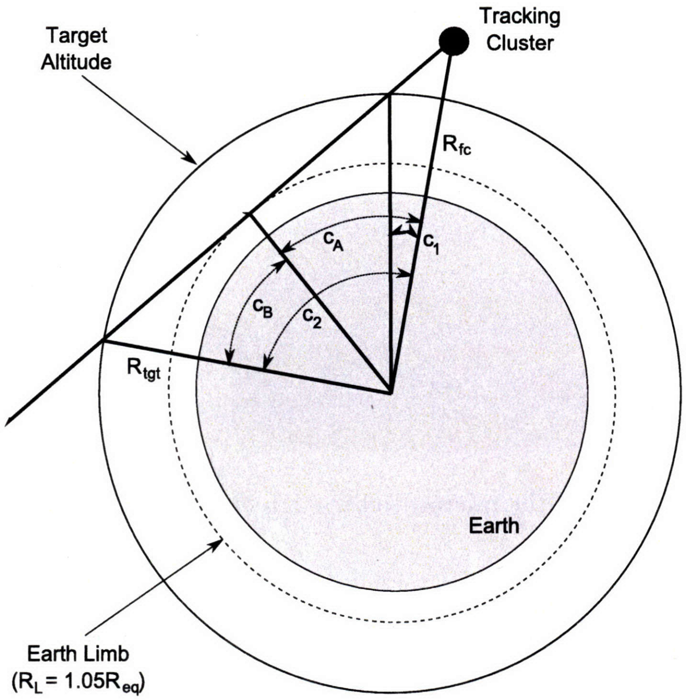

Figure 3-4: Central angle definitions for cluster/target geometry [13].

error for each possible target launch time separated by 60 seconds is used to calculate the average cluster figure-of-merit. The constellation average model-based value for the target position estimation error covariance is

$$O_{const.} = \frac{1}{T}\sum_{j=1}^{T} \min_{i} \left[tr_{pos}\{M_1^{-1}(t_j)\}, \ldots, tr_{pos}\{M_i^{-1}(t_j)\}, \ldots, tr_{pos}\{M_S^{-1}(t_j)\} \right] \tag{3.7}$$

where the matrix operator $tr_{pos}\{\cdot\}$ is the trace of the upper 3×3 portion of the matrix argument (i.e., the position covariance) and the units are length squared (i.e., m^2). Thus, the design problem is to choose the orbital elements of the constellation to minimize $O_{const.}$

$$\begin{aligned} J &= \min_{\mathbf{e_i}} \; O_{const.} \\ s.t. &\quad \mathbf{e_i} \in \mathbf{Œ_{LEO}} \end{aligned} \tag{3.8}$$

The orbital elements of a formation center ($\mathbf{e_i}$) are said to exist in the allowable LEO orbital element set ($Œ_{LEO}$) if

1. $r_p \geq 400 \text{ km} + R_{eq}$
2. $r_a \leq 2500 \text{ km} + R_{eq}$
3. $i = i_{crit}$
4. $\Omega_1 = \ldots = \Omega_i = \ldots = \Omega_S$
5. $\omega_1 = \ldots = \omega_i = \ldots = \omega_S$
6. $M_i = \frac{360^\circ}{S} + M_{i-1}$ (mean anomaly)
7. Q is an integer or simple fraction

In this study a time step of 60 seconds is used and the Lagrangian coefficients transition matrix, Φ_k, defined in Eqn. 2.11 is utilized to propagate the information matrix (Eqn. 2.43). If the constraints from Sec. 3.3.3 are not met at time t_k for cluster i, then no measurement occurs and $M(t_k) = 0$. Otherwise, the information matrix at time t_k is assumed to be equivalent to a cluster with four satellites on a plane through the formation center that is perpendicular to the line-of-sight vector to the target (see Fig. 3-5). The satellites are equally phased by 90 degrees and are 50 km from the formation center. Thus, the information matrix for a single time-step is

$$\begin{aligned} M(t_k) = \frac{1}{\sigma^2} H_k^T H_k &= \sum_{j=1}^{4} \frac{1}{\sigma^2 (1 + \beta |\mathbf{v_j}|)^2} \left[I - \frac{\mathbf{v_j} \cdot \mathbf{v_j}^T}{\mathbf{v_j}^T \cdot \mathbf{v_j}} \right] \\ \text{where: } \beta &= \frac{1}{f} = 1 \text{ m}^{-1} \\ \sigma &= f \cdot 2 \cdot 10^{-5} \text{ rad} = 2 \cdot 10^{-5} \text{ m} \\ \mathbf{v_j} &= \mathbf{v_{fc}} + \delta \mathbf{v_j} \end{aligned} \tag{3.9}$$

This nonlinear optimization problem was solved using MATLAB's built-in constrained nonlinear program (*fmincon*). The program uses a sequential quadratic programming (SQP) method to solve a quadratic programming (QP) subproblem at each iteration. In this method, the Hessian is updated at each iteration [35]. While finding the global optimal solution cannot be guaranteed, the program was run several times with different initial guesses to avoid erroneous, local solutions.

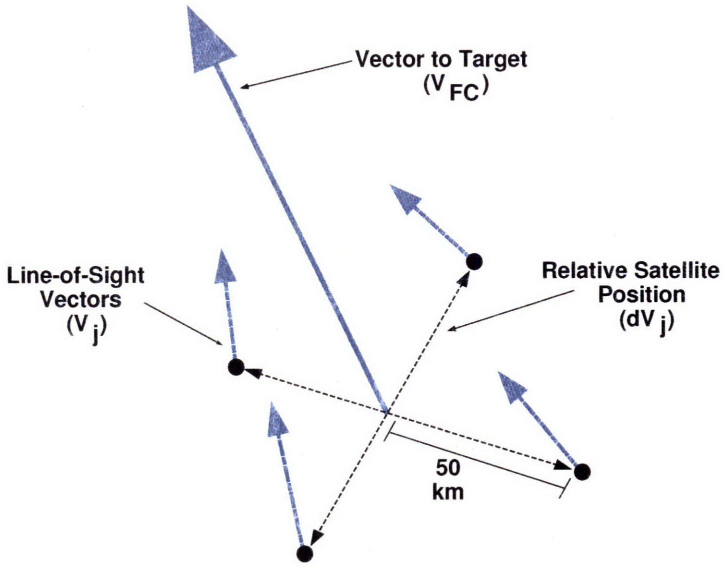

Figure 3-5: Modeled satellite geometry in cluster for constellation design.

3.5 Design Results

Several constellations were considered without constraining the repeat ground track and for all constellations the active constraint was the minimum allowable altitude (400 km). This result corresponded to a repeat ground track of approximately 15.23 orbits/day. Thus, the remaining constellations studied were constrained to a repeat ground track of 15 orbits/day. The cluster/occupancy corridor engagement relative geometry will then re-initialize every 24 hours and will simplify cluster design in following chapters.

Constellation design results for all the admitted configurations in Table 3.2 are presented in Fig. 3-6. Increasing both the number of planes and number of clusters per plane improves (i.e., decreases) the average model-based value for the target position estimation error covariance. There is a significant decrease in $O_{const.}$ between constellations with two planes and three planes. This result suggests that a single cluster can only provide reasonable tracking capability of a target in the occupancy corridor for no more than one-third of a day or five consecutive orbits. Similarly, the largest decrease in constellation performance for number of clusters per plane occurs between five and six suggesting that a single cluster in a 15 orbits/day repeat ground track configuration can provide adequate tracking for no more than one-sixth of its orbit. This corresponds to approximately 16 consecutive minutes of tracking coverage of the occupancy corridor for each cluster in a constellation with an orbital period of 96 minutes.

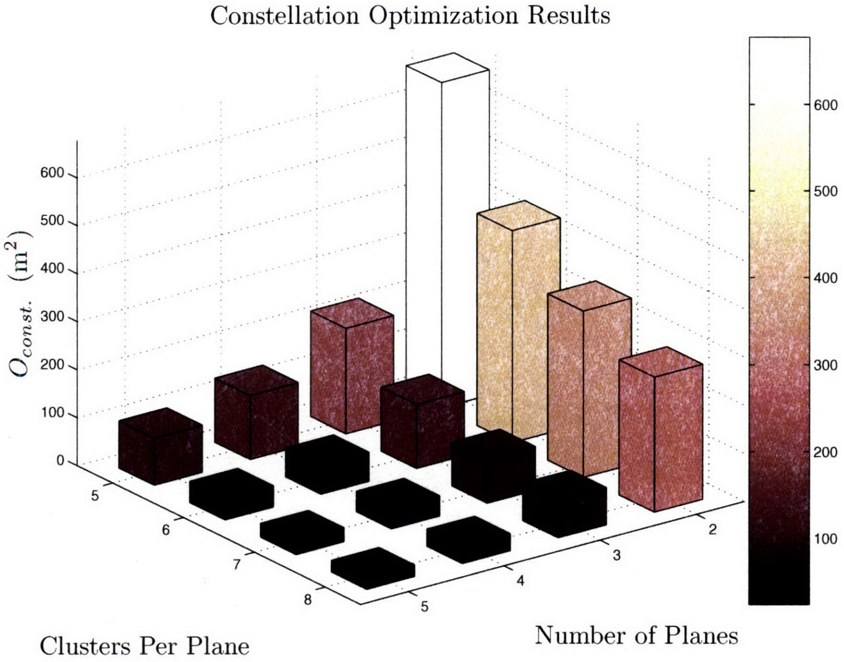

Figure 3-6: The average target position estimation error covariance as estimated in the model is plotted against number of planes and clusters per plane.

Results plotted against clusters per constellation are provided in Fig. 3-7. The most interesting observations are for the two constellation with 24 clusters and the constellation with 25 clusters. The four plane, six clusters per plane constellation has a better performance index than the three plane, eight clusters per plane and the five plane, five clusters per plane constellations. This result suggests that for constellation designs with more than 24 clusters that the constellation should have at least four planes and six clusters per plane.

The improvement in tracking capability per additional cluster (i.e., the derivative) is plotted in Fig. 3-8 by considering the convex hull of the data points in Fig. 3-7. The plot show a diminished return per additional cluster that can be approximated by an exponential curve. The plot suggests that for constellation with more than 25 clusters there is little to no improvement in tracking capability per additional cluster in the constellation. This information is important when weighing the expected tracking capability of a constellation with the cost of implementing the constellation.

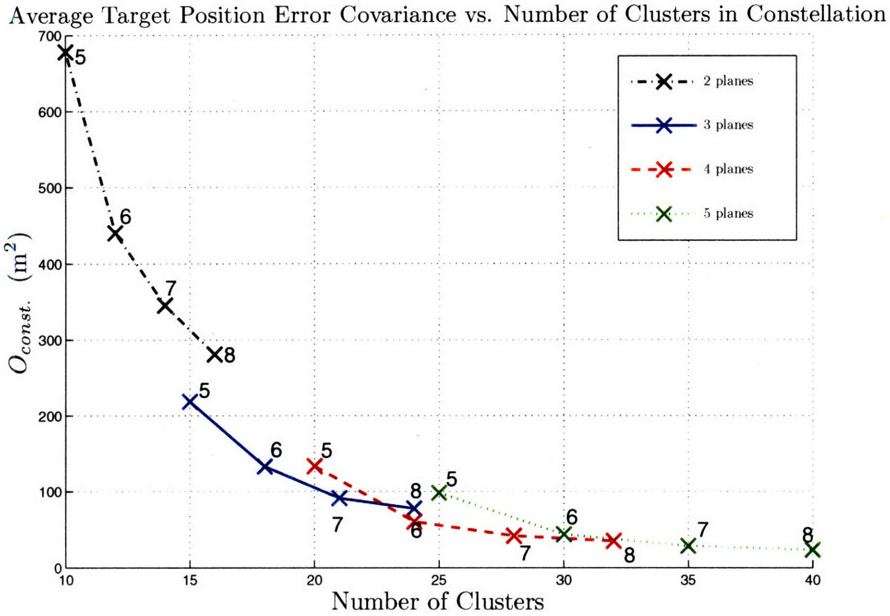

Figure 3-7: The average target position estimation error covariance as estimated in the model is plotted against number of clusters in the constellation. The x's mark the number of cluster's per plane.

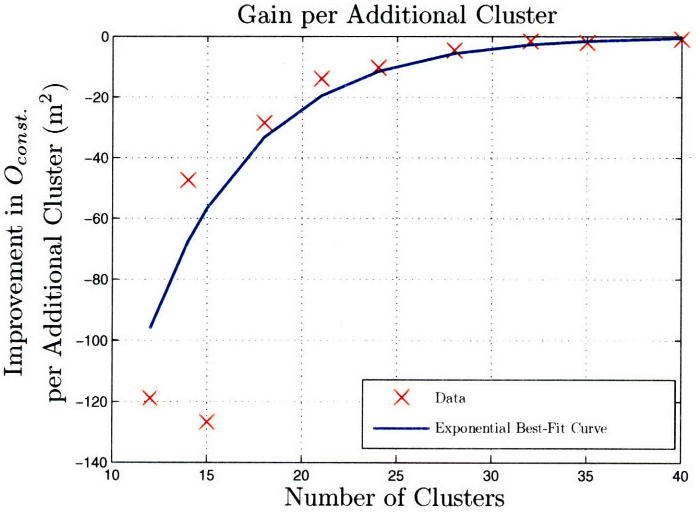

Figure 3-8: Plot showing improvement in average model-based value for the target position estimation error covariance per additional satellite for the convex set of points in Fig. 3-7. These results show diminished returns in constellation performance after approximately 25 clusters in the constellation.

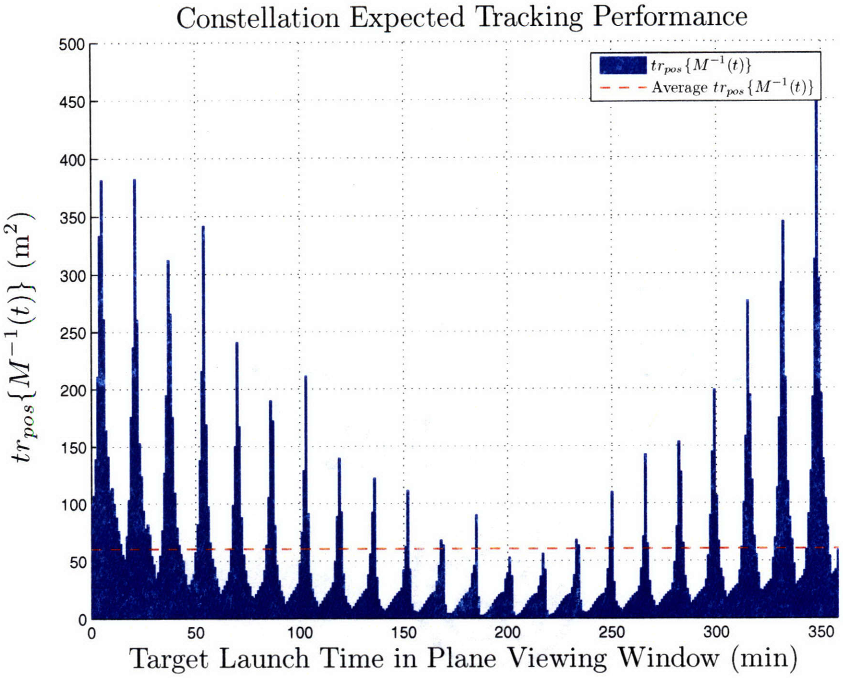

Figure 3-9: Design results for a Walker delta pattern with four planes, six clusters per plane and a repeat ground track of 15 orbits/day.

3.5.1 Constellation with Four Planes, Six Clusters Per Plane

A constellation with four planes and six cluster per plane is chosen to provide 24 hour coverage of the perceived occupancy corridor because constellations with more cluster assets had minimal improvement in tracking performance per additional cluster. Fig. 3-9 presents the target position error covariance as estimated in the model over the entire coverage window of a single plane (six hours). The average value is 60.5 m^2 and the standard deviation is 73.1 m^2. In addition, the mean is 31.3 m^2 and the worst case estimated target position error covariance is 487.2 m^2. The peaks in Fig. 3-9 correspond to the extremes between two clusters when the cluster/target engagement relative geometry is the worst for two consecutive clusters. The hulls correspond to good cluster/target engagement relative geometry. The overall convexity of the plot is due to diminished tracking capability due to the extremes of the plane rotating across the occupancy corridor in the ECEF reference frame (i.e., $|\Omega_{fc} - \Omega_{tgt}|$). This behavior is logical since it was previously observed that more orbital planes in the constellation design improved the average model-based estimation of the target position error covariance.

The constellation's semimajor axis is 6887.86 km and eccentricity is zero (both typical

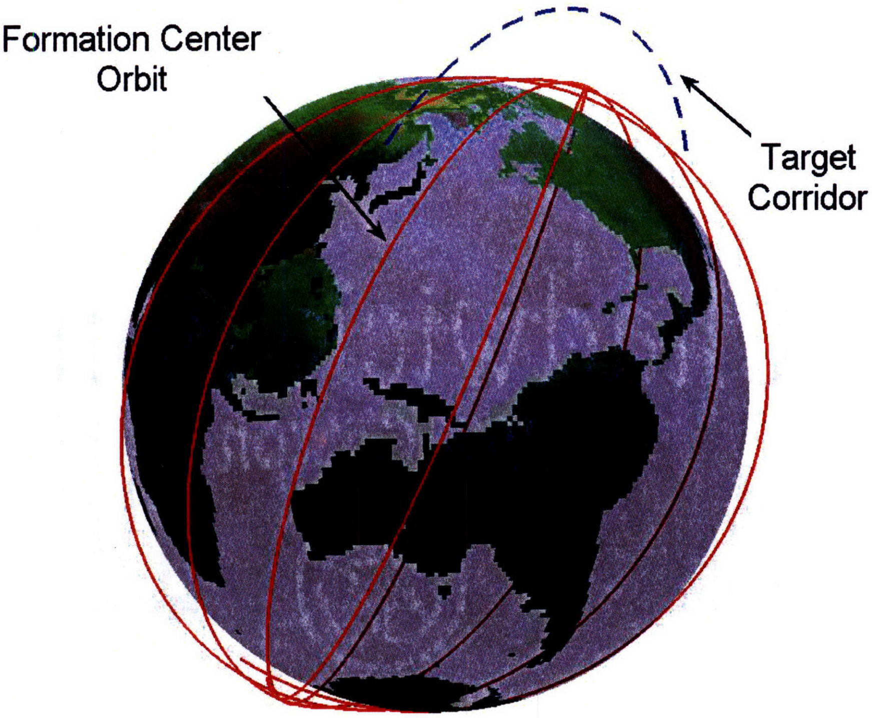

Figure 3-10: Target corridor and optimal formation center of the constellation plotted in the ECEF coordinate frame.

of all constellation designs). A node, or formation center, of the constellation is plotted in Fig. 3-1 along with the occupancy corridor in the ECEF coordinate frame. The four consecutive plotted orbits correspond to the six hour window which the cluster would be capable of tracking a target in the occupancy corridor. The ground trace of the constellation over 30 days is shown in Fig. 3-11 and the 15 orbit/day repeat ground track is easily observable.

Table 3.3 presents data for a single node of the constellation that will be used as a formation center for cluster design in the following chapters. Plots in Fig. 3-12 show criteria on $(\Omega_{target} - \Omega_{cluster})$ and $\theta_{cluster}$ that identify the cluster with the best tracking capability for the corresponding target trajectory. This information provides a subspace for cluster design that reduces the complexity of the design problem and allows the clusters to be synthesized completely independent of each other. The equations for tracking coverage

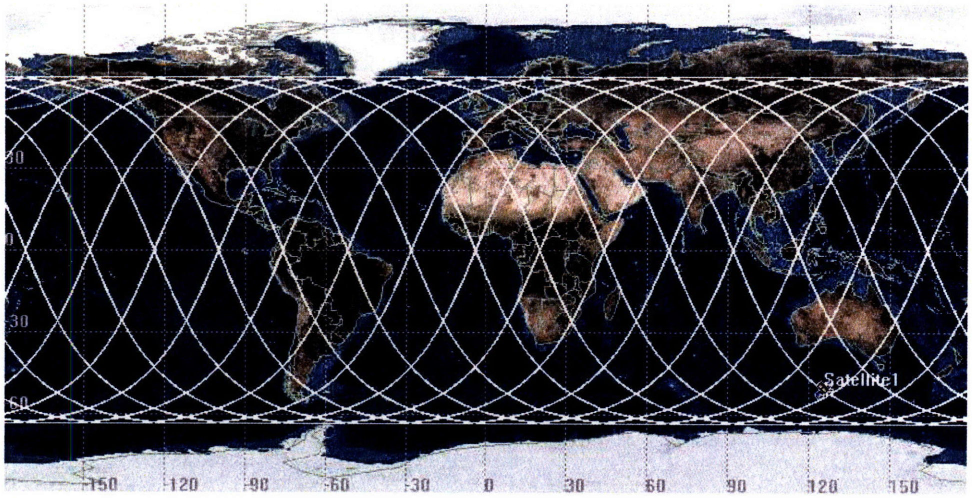

Figure 3-11: The ground trace of a satellite in the constellation over 30 days.

Table 3.3: Constellation and formation center parameters used for cluster design in following chapters.

Parameter	Value
Number of Planes	4
Number of Clusters per Plane	6
a	6887.86 km
e	0
i	63.43°
ω	n/a
$\Omega^\star$	$-21.638°$
$\theta^\star$	$-120°$

$\star$ These values are specific to each cluster and can be derived from the number of planes and number of clusters per plane.

criteria of a single cluster are

$$2.25 \leq (\Omega_{target} - \Omega_{cluster}) \leq 3.86 \tag{3.10}$$

$$-1.85 \leq \theta_{cluster} - \frac{1}{2}(\Omega_{target} - \Omega_{cluster}) \leq -0.76 \tag{3.11}$$

where: $\Omega \in [-\pi, \pi]$ and $\theta \in [-\pi, \pi]$

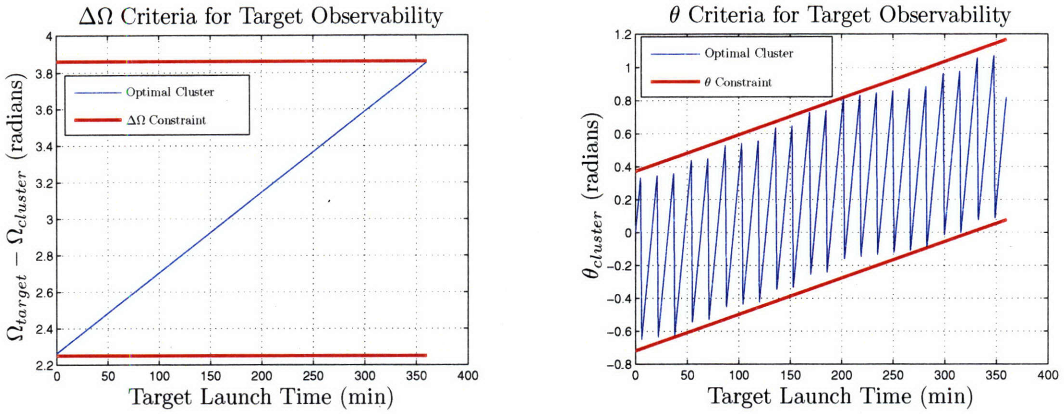

(a) Relative cluster right ascension. (b) Cluster argument of latitude.

Figure 3-12: Plots showing configuration values for the cluster in the plane that is predicted to provide the lowest model-based value for the target position estimation error covariance. This data is utilized to predict when a cluster is responsible for tracking a target in the occupancy corridor given the time of launch of the target.

3.6 Chapter Summary

This chapter presented an optimal approach to constellation design that minimized the average model-based value for the target position estimation error covariance. Observations from the results presented in this chapter suggest that a critically inclined cluster would be capable of providing tracking coverage of the occupancy corridor for up to approximately one-third of a day. This corresponds to no more than five orbits for the constellation configuration chosen. Similarly, each orbital pass of the cluster should be capable of providing coverage of the corridor for up to approximately 16 minutes.

Most importantly for this thesis, the results from this chapter provided a formation center's stable orbit about which the relative motion of the microsatellites in a cluster can be synthesized. The formation center in Sec. 3.5.1 will be used throughout the remainder of this thesis. This chapter did not present an absolute optimal constellation configuration for coverage of the occupancy corridor—rather, it provided stable orbits about which a cluster may be designed for tracking missions. In the process, however, a lower bound for constellation design was achieved that provides information for target tracking capability of different constellation configurations. The four plane, six clusters per plane Walker delta pattern can be used as an initial baseline design for further studies with more sophisticated or in-depth constellation designs.

Chapter 4

Designing a Tracking Cluster

Having found an optimizing *formation center*, the design and control of a cluster of microsatellites about that formation center for target tracking missions are considered in this chapter. The cluster of microsatellites flying in LEO must track an object above the Earth's atmosphere. The design objective is to synthesize a cluster about the orbit that will minimize the average estimation error of a target within the *occupancy corridor.* The approach for this problem uses optimal measurement techniques to choose the microsatellite relative orbital elements in the cluster about the formation center defined in Table 3.3. Thus, the problem is to choose the $6N$ relative orbital elements of the N microsatellites in a cluster to minimize the average model-based value for the position estimation error covariance of a target in the occupancy corridor.

This research focuses on the geometric properties of the cluster such as cluster baseline and assemblage sizes. Intuitively, both larger cluster baseline and assemblage sizes should provide better mission performance; however, the larger cluster will require better communication technology and more power on board each satellite since the cluster must be able to communicate target line-of-sight measurements amongst itself for the onboard extended Kalman filter. Ref. [34] has previously demonstrated that increasing the number of satellites in a cluster can improve tracking accuracy. In addition, this research investigates a methodology to design a target tracking cluster with minimal relative satellite drift due to the J_2 gravitational harmonic.

This chapters's organization is as follows: The problem statement and a cluster's target tracking figure-of-merit are described in Sec. 4.1. Sec. 4.2 then lays out the cluster design approach. An important element of this section is the design of a cluster that penalizes both target observability and J_2-induced relative drift. Finally, cluster design results are presented in Sec. 4.3.

4.1 Approach to Cluster Design

This section describes the cluster design problem and approach utilized in this chapter to synthesize the relative motion of the satellites in the cluster about the formation center.

4.1.1 Problem Definition

The problem considered in this thesis is to develop a spaced-based system of microsatellites in LEO that provides 24 hour coverage of the occupancy corridor described in Sec. 3.1. Chapter 3 dealt with the constellation design component of this problem to provide 24 hour coverage. This chapter considers the cluster design problem within the context of the constellation design.

The function of the tracking clusters is to discriminate and accurately track a target when given a cue to the target's initial position and velocity. The cluster is a distributed array of microsatellites capable of communicating between each other and should be designed to provide the best possible target tracking performance when the occupancy corridor is in the cluster's viewing window (as was defined in Eqn. 3.10 and 3.11). The first objective presented in this chapter is to synthesize the relative motion of the microsatellites to minimize the expected target tracking error. Clusters with baselines up to 1000 km and with two to eight microsatellites per cluster are considered in this research to determine how these geometric constraints affect target tracking performance.

A cluster of microsatellites can drift apart with time due to non-Keplerian forces. Thus, the second objective in this chapter is to design a cluster that exhibits minimal relative satellite drift due to the J_2 gravitational harmonic.

4.1.2 Linearized Relative Motion Model

This chapter makes use of the concept of the formation center, which has been widely utilized in formation flying coordination to choose a virtual stable Earth orbit in which relative satellite motion is modeled. The formation center is chosen in this study as a node of the constellation from the previous chapter (see Table 3.3) and allows the relative dynamic models and the cluster baseline size constraints to be defined.

The linearized state transition matrix developed in Ref. [14] are used for modeling satellite relative motion and are valid for both circular and highly eccentric orbits even though this chapter only requires modeling relative motion for circular orbits. This model will allow the methodology to be easily extended to eccentric orbits. The relative motion model was original presented in Sec. 2.2.

4.1.3 Cluster Target Tracking Figure-of-Merit

The A-optimality criterion of the information matrix is used to formulate a figure-of-merit to synthesize the microsatellites' relative orbital elements. Since the objective of this problem is to minimize a time average value of the target position error covariance over a 24 hour period, the optimization cost function is

$$O_{clust.} = \frac{1}{T}\sum_{i=1}^{T} tr_{pos}\{M^{-1}(t_i)\} \tag{4.1}$$

$O_{clust.}$ is the average model-based value for the target position estimation error covariance where T represents a discretization over all possible target launch times in a 24 hour period for which the cluster has been given the task of tracking objects in the occupancy corridor. This study uses a discretization time step of 60 seconds between target launch times.

4.2 Cluster Design Objective

This section presents the cluster design objectives and optimization formulation using optimal measurement techniques.

4.2.1 Optimal Measurement Technique

The first cluster design objective is to choose the six relative orbital elements ($\delta \mathbf{e}_i$) with respect to the formation center for the N microsatellites to minimize Eqn. 4.1. In this approach, the differential mean semimajor axis of each microsatellite is constrained to zero ($\delta a_i = 0$) so that all the microsatellites have the same orbital period. In addition, the constraint that all relative motion resides within a cube of a given baseline about the

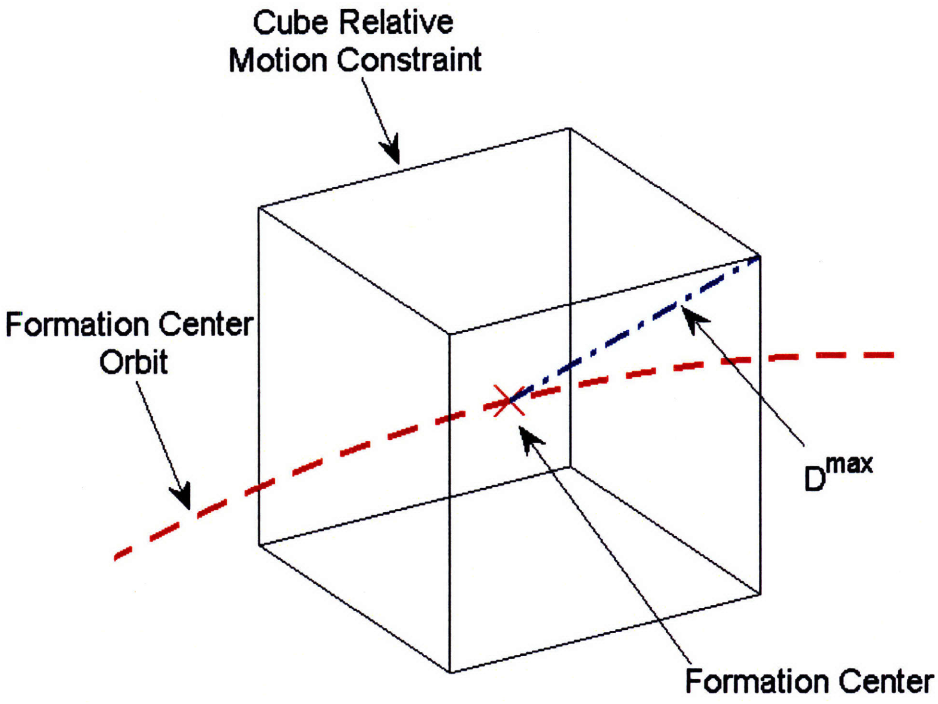

Figure 4-1: Relative satellite motion baseline constraint about the formation center.

formation center is applied to constrain maximum satellite separation. This constraint is chosen as opposed to natural metrics such as Gurfil's distance norm [15] because it can be posed as a linear constraint on satellite relative motion. The baseline D^{max} is defined as the Euclidean distance from the center of the cube (or formation center) to one of the cube's corners (see Fig. 4-1). Thus, the optimization design problem is

$$\begin{aligned} J &= \min_{\delta \mathbf{e_i}} O_{clust.} \\ s.t. \quad & |x_i(t)| \leq d \\ & |y_i(t)| \leq d \\ & |z_i(t)| \leq d \\ & \delta a_i = 0 \\ & i \in (1, \ldots, N) \text{ (satellites)} \\ & t \in (1, \ldots, T) \text{ (time)} \\ & d = \sqrt{\frac{1}{3}} D^{max} \end{aligned} \tag{4.2}$$

and all clusters with $N = (2, \ldots, 8)$ and $D^{max} = (50, 100, 250, 500, 1000)$ km are synthesized.

4.2.2 Optimal Measurement Technique Augmented with J_2-Induced Relative Drift Penalty

The second object of this study is to design a cluster that augments the target tracking performance index from Eqn. 4.2 with a penalty on J_2-induced relative drift since the members of a cluster can be expected to drift relative to their formation center and each other due to non-Keplerian gravitational effects.

Ref. [31] presents criteria for designing relative satellite orbits that are invariant to J_2-induced relative drift; while the satellites are both subjected to J_2 disturbances, they maintain the same secular relative motion every orbit. The approach uses a linear expansion about the formation center which drops higher order terms (i.e., $O({J_2}^2)$) to provide criteria for choosing δa, δe and δi to prevent relative nodal drifts in $\delta\Omega$, $\delta\omega$ and δM. The relative argument of perigee and mean anomaly drift rates are combined in this study since the formation center is in a circular orbit ($\delta\theta_M = \delta\omega + \delta M$). The relative drift rates are

$$\begin{bmatrix} \delta\dot{\Omega} \\ \delta\dot{\theta}_M \end{bmatrix} = \begin{bmatrix} 0 & \frac{3}{2}J_2\frac{r_e^2}{a^2}\frac{n}{\eta^4}\sin i & \frac{3}{2}J_2\frac{r_e^2}{a^2}\frac{n}{\eta^5}4\cos i \\ -\frac{3}{2}\sqrt{\mu}a^{-5/2} & -\frac{3}{4}J_2\frac{r_e^2}{a^2}\frac{n}{\eta^4}\sin i & -\frac{3}{4}J_2\frac{r_e^2}{a^2}\frac{n}{\eta^3}3\sin(2i) \end{bmatrix} \begin{bmatrix} \delta a \\ \delta i \\ \delta\eta \end{bmatrix} \tag{4.3}$$

where all nominal orbital elements are those of the formation center [31]. Combining $\delta\omega$ and δM provides a less restrictive constraint that ensures bounded relative motion but allows these specific orbital elements to slowly change. The linear approximation for satellite relative drift provides drifts rates within a 10% accuracy over all cluster baseline sizes considered in this study and a linear expansion about the relationship $\eta = \sqrt{1-e^2} = \sqrt{1-q_1^2-q_2^2}$ allows the relative drift rates to be written as a linear function of δe

$$\delta\eta = \frac{-q_1}{\eta}\delta q_1 + \frac{-q_2}{\eta}\delta q_2 \tag{4.4}$$

The $\delta\Omega$ drift will have a greater impact on relative satellite separation in relative Cartesian coordinates at high inclinations than low ones. Thus, the estimated change in velocity (ΔV) per orbit (m/s/orbit) required to reestablish $\delta\Omega$ and $\delta\theta_M$ every orbit is used to penalize these drift rates against each other by capturing the effect of the cluster's inclination. The impulsive control scheme developed in Ref. [30] and [33] is utilized to estimate the ΔV necessary to reestablish mean relative orbital elements every orbit. The estimated ΔV per orbit is [33]

$$\begin{bmatrix} \Delta v_h \\ \Delta v_{\theta_M} \end{bmatrix} = \begin{bmatrix} \frac{2\pi}{n}\frac{h \sin i}{r_h} & 0 \\ 0 & \frac{a}{3}\sqrt{\frac{1-e}{1+e}} \end{bmatrix} \begin{bmatrix} \delta\dot{\Omega} \\ \delta\dot{\theta}_M \end{bmatrix} \tag{4.5}$$

Combining Eqns. 4.3, 4.4 and 4.5 provides a linearized metric for the J_2-induced relative drift rates as a linear function of the relative orbital elements. To penalize drift, Λ is defined as the average expected one-norm ΔV expenditure per orbit required to reestablish mean relative orbital elements due to J_2-induced relative drift

$$\Lambda = \frac{1}{N}\sum_{i=1}^{N} \|\Delta v_{hi}\|_1 + \|\Delta v_{\theta_M i}\|_1 \tag{4.6}$$

Now the cost function from Sec. 4.2.1 can be augmented with a penalty on Λ such that the augmented cost function is

$$J = \min_{\delta \mathbf{e}_i} \; R_O \cdot O_{clust.} + R_\Lambda \cdot \Lambda \tag{4.7}$$

Only clusters with four microsatellites and a 250 km baseline are considered for this part of the study. The constraint $\delta a_i = 0$ is relaxed to allow this perturbation to be used in minimizing the relative drift rates of the microsatellites in the cluster. Finally, cluster designs are optimized for a range of relative weights on $O_{clust.}$ and relative satellite drift ($\rho = R_\Lambda / R_O$).

4.3 Results

Nominal cluster design results are presented in this section, as well as results from the optimization problem with an augmented J_2-induced relative drift penalty. In addition, extensive simulations results to verify the optimization approach are presented. The simulation testbed is that described in Sec. 2.4. In order to estimate each cluster's average tracking capability, a Monte Carlo over target launch times is used. Thus, the target follows the same nominal path in the ECEF coordinate frame. All launch times, separated by three minute intervals, in the cluster's viewing window of the target are simulated. Each cluster's simulated tracking performance reported in the next section is the average target position error over the Monte Carlo simulations.

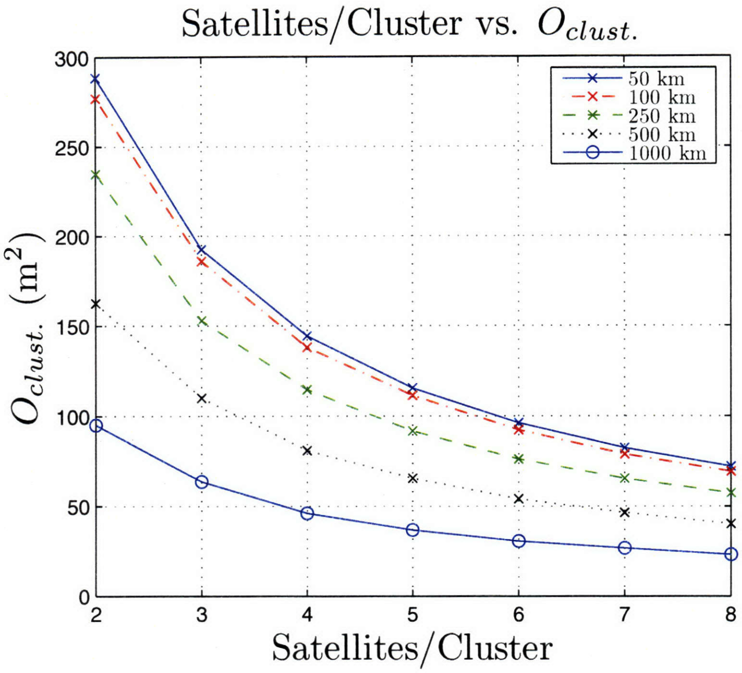

Figure 4-2: Design results for all cluster configurations. Target observability $O_{clust.}$ is defined in Eqn. 4.1.

4.3.1 Comparison of Nominally Synthesized Clusters

The optimal solutions to Eqn. 4.2 for all the cluster configurations were calculated using constrained nonlinear optimization techniques (*fmincon*). $O_{clust.}$, the average model-based value for the target position estimation error covariance, for each cluster configuration is plotted in Fig. 4-2. The model-based predictions support expectations that increasing cluster baseline and assemblage sizes should improve the average model-based value for the target position estimation error covariance. The predictions also suggest that there is a decreasing gain per additional satellite as observability curves monotonically and asymptotically converge as the assemblage size of the cluster increases. It is interesting to note that a three microsatellite cluster with a 1000 km baseline has a similar expected tracking performance index as an eight satellite cluster with a 250 km baseline. These predictions suggest that the relative gain from increasing a cluster's baseline is much greater than simply increasing the cluster's assemblage size.

Monte Carlo simulation results showing actual filter tracking performance for clusters with $N = (2, 3, 4, 5)$ and $D^{max} = (100, 250, 500, 1000)$ km are presented in Fig. 4-3. Average target estimated position error values from the centralized Kalman filter's covariance matrix are reported in Fig. 4-3(a). The values in Fig. 4-3(a) agree well qualitatively with the

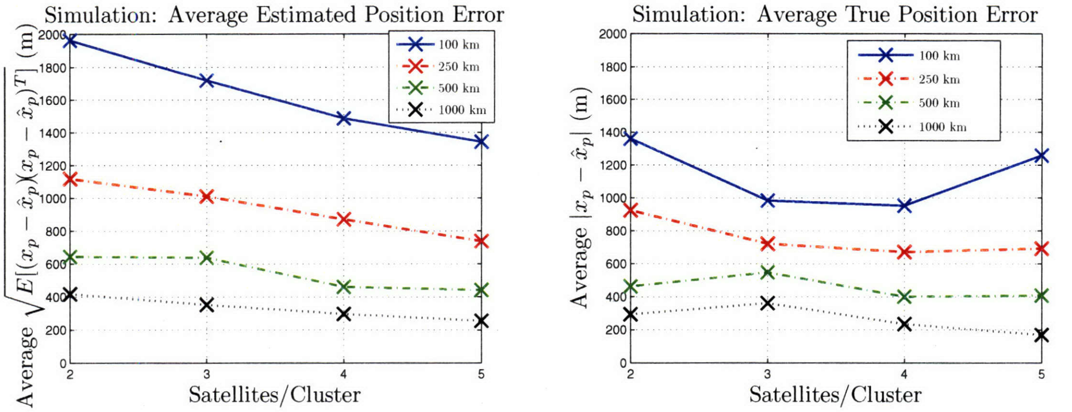

(a) Estimated target position error standard deviation reported from Kalman after filter convergence in Monte Carlo simulations for variable target initial conditions.

(b) Average target position tracking error after filter convergence in Monte Carlo simulations for variable target initial conditions.

Figure 4-3: Graphs showing simulation results for both the estimation standard deviation for target position error and the true average position estimation error over all clusters.

model-based cluster design results in Fig. 4-2. Even though the magnitudes are different in these plots, the relative trends between cluster baseline and assemblage sizes still persist. The increase in magnitudes is driven by sensor noise models for IMU and GPS sensors as well as estimated process noise for the target that is not considered when calculating the information matrix. However, the true target position error results presented in Fig. 4-3(b) show that there is little discernable improvement in tracking error when increasing the assemblage size of the cluster for the larger baseline clusters ($D^{max} \geq 500km$). Increasing the number of satellites from two to three for the smaller 100 km and 250 km baseline clusters increased tracking accuracy. However, increasing the number of satellites for the larger baseline clusters did not have such an impact. These results suggest that tracking accuracy for the larger clusters with better relative cluster/target geometry was limited by the magnitude of the noise sources in the simulation. This result is plausible since the model-based cluster design approach did not take in to account the effect of several noise sources (i.e., GPS, IMU and process noise).

Yet, increasing the assemblage size of the cluster can improve tracking error convergence time as observed in Fig. 4-4. In this study the convergence time is specified as the time for the target position error estimate to converge to within 25% of the final position error for the remainder of the target's 2100 second trajectory. Thus, smaller values correspond to better (i.e., quicker) convergence. The larger clusters (500 km and 1000 km baselines) did

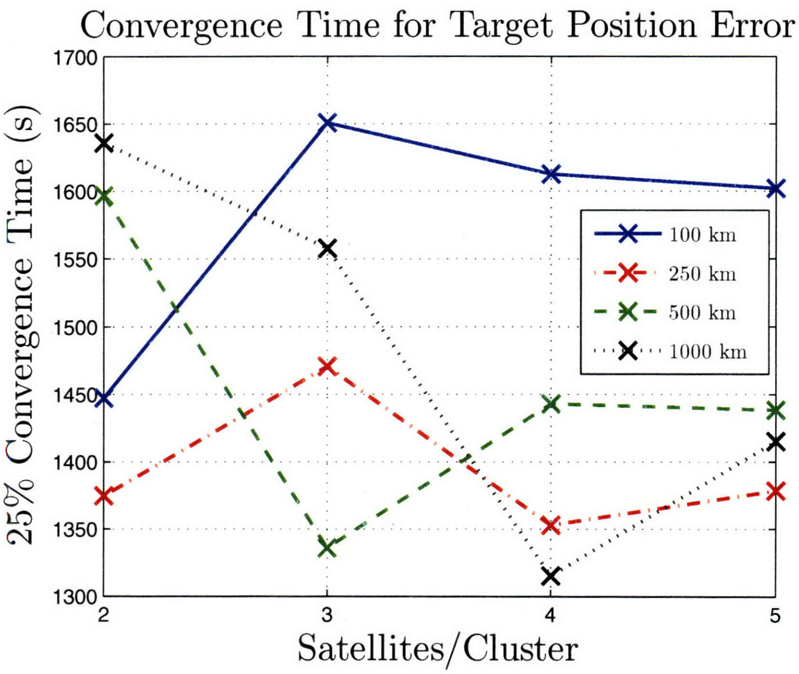

Figure 4-4: Plot of average tracking error convergence times for all simulated cluster configurations.

not show tracking error improvement when increasing the number of satellites. However, the convergence time for these clusters does improve with additional satellites. The 100 km baseline cluster's average convergence time from two to three satellites shows atypical behavior as it dramatically increased by 200 seconds. This is due to the fact, however, that the average tracking error was reduced by approximately 400 m between these cluster configurations. Criteria for tracking convergence is much lower for the three satellite cluster than the two satellite cluster. The tracking error profiles over time are otherwise very similar for these two clusters. These results suggest that a larger baseline with approximately four satellites would be ideal in every way for good target tracking performance.

The cluster design approach described in Sec. 4.2.1 did not penalize J_2-induced relative drift. Yet, the approximated relative drift for the synthesized clusters can be calculated using the analytic approach described in Sec. 4.2.2. The results, in terms of the average ΔV required to maintain the cluster's relative orbital elements, are reported in Table 4.1 against cluster baseline size. There is approximately a linear relationship between cluster baseline size and relative drift. If a cluster control algorithm were to expend ΔV at the rate used in this control scheme, then the life span of clusters with larger baselines would likely be no more than a few months. Ref. [18] predicted the total available ΔV for a mission of

Table 4.1: Average estimated ΔV consumption required to maintain mean relative orbital elements for clusters due to J_2-induced relative drift using the approach described in Sec. 4.2.1.

Cluster Baseline (km)	Average Expected ΔV Consumption (m/s/orbit)
50	0.1838
100	0.3653
250	1.2302
500	2.4045
1000	5.2633

small, light spacecraft to be on the order of 400 m/s—only about 80 orbits for the 1000 km clusters.

While these expected ΔV expenditure results are much higher than predicted for many other formation flying missions, they are not surprising. First, the semimajor axis of the cluster's orbit is very small and, thus, the effects of the J_2 harmonic are much higher than formation flying missions with larger semimajor axes. Another consideration is the size of the clusters in this study. While other formation missions have considered satellite Cartesian separations of similar sizes such as some studied for MMS, the magnitude of the $\delta \mathbf{e_i}$'s in this study are larger than many other missions. The magnitude of the relative drifts rates should therefore be higher as well. These results emphasize the importance of considering the expected ΔV consumption when designing low altitude, largely separated clusters.

4.3.2 Results from Cost Function Augmented with J_2-Induced Relative Drift Penalty

Fig. 4-5 presents drift rates and average model-based value for the target position estimation error covariance for optimal solutions to Eqn. 4.7 with several relative costs $\rho = (0, 0.01, 0.1, 1, 10, 100)$. These predictions for four satellite, 250 km baseline clusters show that augmenting the cost function with a penalty on the J_2-induced relative drift can greatly reduce the expected ΔV consumption per orbit while having minimal impact on target observability. The drift rates are reduced by a factor of a thousand while only having approximately a 8% degradation in $O_{clust.}$. Average target tracking error results from Monte Carlo simulations are presented in Table 4.2 and support these findings. Fig. 4-6 shows the relative motion of a cluster over 15 orbits designed in Sec. 4.3.1 and one with

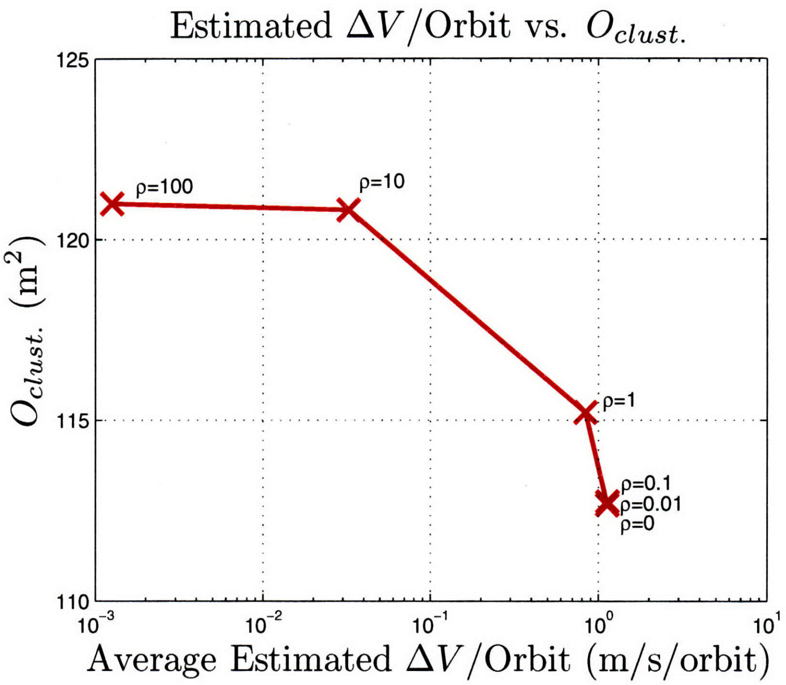

Figure 4-5: Estimated ΔV budget plotted against $O_{clust.}$ for a range of relative costs for four satellite, 250 km baseline clusters. Note that the x-axis is a logarithmic scale.

a high penalty on drift ($\rho = 100$) designed in this section. The relative drift is easily discernable in Fig. 4-6(a) but not Fig. 4-6(b). Designing a space based tracking cluster of microsatellites with criteria on J_2-induced relative drift is easily formulated and can likely extend the cluster's lifetime by reducing the relative microsatellite drift and the need to implement control maneuvers.

These results show that designing a tracking cluster does not require that all six degrees of freedom (or relative orbital elements) be freely chosen. When $\rho = 0$, the optimization problem is allowed to choose the six relative orbital elements freely to minimize the estimated tracking error. However, with a high value of ρ, there are essentially two constraints on four of the relative orbital elements of each satellite. Conceptually, this is equivalent to constraining the design problem to a four-dimensional plane in six-dimensions. These results show that these two constraints on each satellite are not so overly constringent that they cause a large degradation in the cluster's tracking capability.

Table 4.2: Simulation results for clusters with different relative costs on average model-based value for the target position estimation error covariance and J_2-induced relative drift.

ρ	Average Estimated Target Position Error (m)	Average True Target Position Error (m)
0	871.2	671.2
0.01	824.9	847.9
0.1	795.8	705.8
1	858.5	551.3
10	900.4	1051.3
100	958.7	576.4

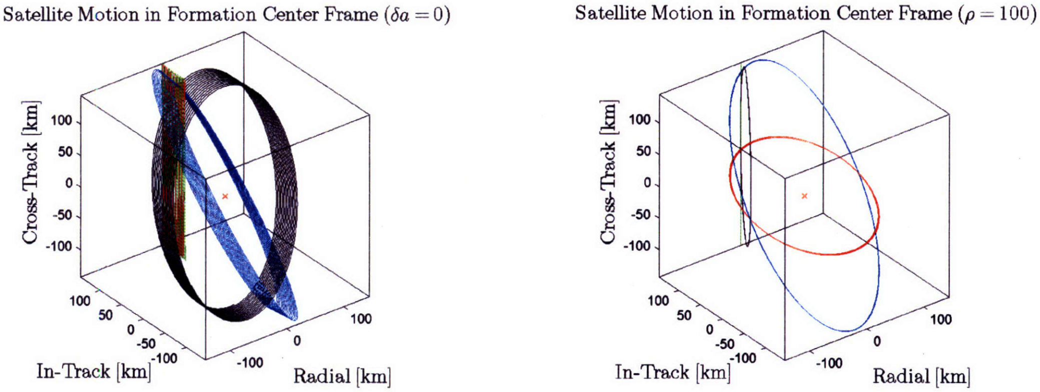

(a) Standard Approach to Cluster Design ($\delta a = 0$).

(b) Cost Function Augmented with J_2-Induced Relative Drift ($\rho = 100$).

Figure 4-6: Cluster relative motion over 15 orbits (or 24 hours) for the two design approaches. The relative drift of the satellites in (a) is clearly greater than in (b).

4.4 Chapter Summary

The objective of this research was to use optimization techniques to design a cluster of microsatellites such that the cluster optimally tracks a target in a perceived occupancy corridor. This study focused on the geometric properties of the cluster to gain insight into how cluster baseline and assemblage sizes can affect a cluster's tracking accuracy. The model-based and simulation results suggest that cluster baseline size is more important than the number of satellites in the cluster. Clusters with a baseline of 1000 km performed better in simulation regardless of the number of satellites in the cluster. In addition, the linear penalty on J_2-induced relative drift provided an intuitive approach to designing a cluster that exhibits minimal relative drift without significantly penalizing target tracking performance.

The concept of operations in this experiment dictated that each cluster was only capable of communication amongst itself. For that reason, the cluster baseline was used to constrain geometric distance to simulate communication constraints. Yet, the largest baseline clusters provided the best target tracking accuracy. If the baseline constraint was removed or largely increased for cluster design, then the notion of a cluster may start to fade and the constellation would begin to look like a large dispersion of satellites. In terms of a resource allocation problem, the *constellation of clusters* approach to space-based tracking missions may not be the best approach. A highly populated constellation of microsatellites where each single satellite is capable of communicating with neighboring satellites may be a better system approach. Further experiments would need to be carried out to test this notion.

THIS PAGE INTENTIONALLY LEFT BLANK

Chapter 5

Volume Heuristic for Cluster Design

In the previous chapter a target tracking cluster of microsatellites was synthesized using optimal measurement techniques. The relative motion of the microsatellites in the cluster was chosen to minimize an average model-based value for the target position estimation error covariance in a well-known *occupancy corridor.* Clusters were designed that exhibited very good tracking behavior. However, the approach has two drawbacks. First, the error covariance minimizing optimal cluster method presented previously relies upon a precise specification of the design target orbit—this will rarely be possible in practice. One approach to address this problem may be to choose a dispersion of candidate trajectories to model the occupancy corridor [27]. However, the occupancy corridor may change after the cluster has already been initialized or target tracking capability of a new occupancy corridor may be desired. Second, the optimal measurement approach to cluster design is complex because the target trajectory and information matrix need to be propagated forward. If a cluster maintenance scheme were implemented using $O_{clust.}$ as a constraint or as a terminal cost to weigh against fuel consumption, then optimal measurement metrics may not be suitable. Given these drawbacks, this chapter explores a robust heuristic for designing a cluster that simply provides good cluster geometry for tracking a target in any direction at any point in time.

This chapter begins with a derivation for using the maximum average *tetrahedral volume* as a heuristic for cluster design by assuming that the target position and trajectory are unknown. Several four satellite clusters are synthesized in Sec. 5.2 to maximize average tetrahedral volume about the same *formation center* used in the previous chapter. Design results are compared to clusters designed in Chapter 4 that minimized the average model-based value of the target position estimation error covariance and are tested in simulation. Model-based predictions and simulation results presented in Sec. 5.3 show that using average tetrahedral volume as a cluster design heuristic is very good for smaller baseline clusters ($D^{max} \leq 250$ km) even when the occupancy corridor can be accurately defined. These clusters perform just as well in simulation as clusters designed in Chapter 4 to minimize the average model-based value of the target position estimation error covariance.

An extension to the tetrahedral volume heuristic is also presented in this chapter for clusters with more than four satellites. Finally, clusters are synthesized with a penalty on J_2-induced relative drift to demonstrate that a cluster which maximizes average tetrahedral volume can also be designed that exhibits little relative satellite drift with minimal degradation in average tetrahedral volume (and expected target tracking capability).

5.1 Extension to Robust Design of Tracking Clusters

This section begins with a derivation for using tetrahedral volume as a cluster design heuristic, which is based on the assumption that the target may be in any direction at any point in time. Thus, the heuristic design goal is to provide good viewing geometry for a target in any direction. A simple study suggests that this design criteria is acceptable when the cluster baseline size (i.e., maximum satellite distance from the formation center) is less than approximately 63% of the distance from the formation center to the target. Finally, the average tetrahedral volume figure-of-merit using the linearized state-transition matrices is also provided in this section.

5.1.1 Derivation of Volume Heuristic

Consider the cluster in Fig. 5-1 where ζ is the target position vector with respect to the formation center (FC) and x_1, x_2, x_3 and x_4 are the satellite position vectors. It can be assumed that the formation center is the geometric mean of the four satellites such that $x_1 + x_2 + x_3 + x_4 = [0, 0, 0]^T$. The information matrix for the target's position due to the pointing vector measurement from a single satellite in the cluster was defined by Eqn. 2.33

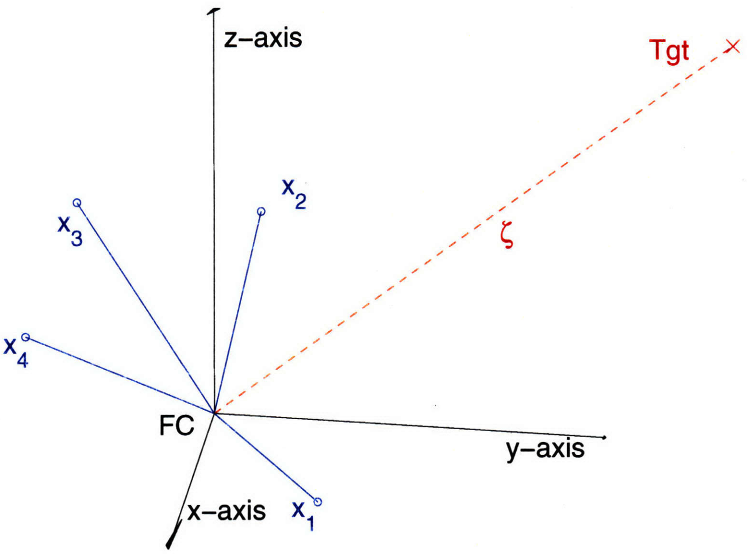

Figure 5-1: Definition of variables used to derive the tetrahedral volume cluster design heuristic.

and repeated here for convenience

$$M_i = \frac{1}{\left(1+\beta\sqrt{(\zeta - x_i)^T \cdot (\zeta - x_i)}\right)^2} \left[I - \frac{(\zeta - x_i)\cdot(\zeta - x_i)^T}{(\zeta - x_i)^T \cdot (\zeta - x_i)} \right] \tag{5.1}$$

By assuming that the focal length is small (i.e., $\beta = \frac{1}{f} \gg 1$), that $|\zeta| \gg |x_i|$ such that $(\zeta - x_1)^T \cdot (\zeta - x_1) \approx \zeta^T \cdot \zeta$ and $|\zeta| = 1$, a single information matrix due to a single satellite measurement is approximated as

$$\begin{aligned} M_i &\approx \frac{1}{\beta^2}\left[I - (\zeta - x_i)\cdot(\zeta - x_i)^T\right] && (5.2)\\ &\approx \frac{1}{\beta^2}\left[I - \zeta\cdot\zeta^T + x_i\cdot\zeta^T + \zeta\cdot x_i^T - x_i\cdot x_i^T\right] && (5.3)\end{aligned}$$

Thus, the aggregate information matrix for the target position vector from the four satellite line-of-sight measurements is

$$\begin{aligned} M &= M_1 + M_2 + M_3 + M_4 && (5.4)\\ &\approx \frac{1}{\beta^2}\Big[4I - 4\zeta\cdot\zeta^T + (x_1 + x_2 + x_3 + x_4)\cdot\zeta^T + \zeta\cdot(x_1 + x_2 + x_3 + x_4)^T \\ &\quad - x_1\cdot x_1^T - x_2\cdot x_2^T - x_3\cdot x_3^T - x_4\cdot x_4^T\Big] && (5.5)\end{aligned}$$

Since the sum of the perturbational satellite positions (x_i's) is the zero vector ($x_1 + x_2 + x_3 + x_4 = [0,0,0]^T$), the information matrix can further be reduced to

$$M \approx \frac{1}{\beta^2}\left[4I - 4\zeta \cdot \zeta^T - x_1 \cdot x_1^T - x_2 \cdot x_2^T - x_3 \cdot x_3^T - x_4 \cdot x_4^T\right] \tag{5.6}$$

The information about the target's position in any particular direction can be found by multiplying M by a vector in that direction. It can also be observed that the first part of Eqn. 5.6 ($4I - 4\zeta \cdot \zeta^T$) has a vector null space in the direction of ζ. Thus,

$$[4I - 4\zeta \cdot \zeta^T] \cdot \zeta = [0,0,0]^T \tag{5.7}$$

If the information matrix M is not invertible, then the cluster does not provide information of the target's position in one direction. For the cluster to be able to provide information in each direction of the target's position requires that M must be invertible.

Since Eqn. 5.7 is true, M is invertible only if

$$[x_1 \cdot x_1^T + x_2 \cdot x_2^T + x_3 \cdot x_3^T + x_4 \cdot x_4^T] \cdot \zeta \neq [0,0,0]^T \tag{5.8}$$

Yet, ζ is unknown—directly calculating Eqn. 5.8 is not possible. It can be observed, however, that if

$$\det\left([x_1 \cdot x_1^T + x_2 \cdot x_2^T + x_3 \cdot x_3^T + x_4 \cdot x_4^T]\right) \neq 0 \tag{5.9}$$

then Eqn. 5.8 will hold regardless of the value of ζ. A robust design heuristic for a four satellite cluster can be stated as

$$J = \max_{x_i} \left| \begin{bmatrix} x_1 & x_2 & x_3 & x_4 \end{bmatrix} \cdot \begin{bmatrix} x_1 & x_2 & x_3 & x_4 \end{bmatrix}^T \right| \tag{5.10}$$

This design heuristic will ensure that M is always invertible regardless of the target position. More importantly, maximizing the determinant is equivalent to minimizing the volume of the uncertainty ellipsoid [40]. It will promote uniform viewing geometry in the cluster for a target in any position.

The design heuristic in Eqn. 5.10 has underlying geometric characteristics. The square root of the cost function is the projected three-dimensional parallelepiped volume of the x_i vectors. Since the matrices in Eqn. 5.10 are both maximum rank three matrices and the volume can be expressed by the edges of the figure, the cluster design heuristic can be more compactly written as

$$J = \max_{x_i} \begin{vmatrix} x_1 - x_4 & x_2 - x_4 & x_3 - x_4 \end{vmatrix} \cdot \begin{vmatrix} x_1^T - x_4^T \\ x_2^T - x_4^T \\ x_3^T - x_4^T \end{vmatrix} \tag{5.11}$$

The square root of this results multiplied by one-sixth is simply the *tetrahedral volume.* Recall that the tetrahedral volume of four vertices in a three-dimensional space is

$$V_{4\star} = \frac{1}{6} \cdot \sqrt{\begin{vmatrix} x_1 - x_2 & x_2 - x_3 & x_3 - x_4 \end{vmatrix} \cdot \begin{vmatrix} x_1^T - x_2^T \\ x_2^T - x_3^T \\ x_3^T - x_4^T \end{vmatrix}} \tag{5.12}$$

Thus, maximizing the tetrahedral volume of a four satellite cluster should provide a uniformly maximum of the information matrix given that ζ is unknown

$$\text{argmax } V_{4\star} \approx \text{argmax } |M| \tag{5.13}$$

The tetrahedral volume cluster design heuristic should provide a target tracking cluster with good geometry for tracking a target in any direction.

A logical question is: Does maximizing the tetrahedral volume provide an intuitive and dependable heuristic for designing a target tracking cluster with four satellites when the cluster is constrained to a maximum baseline? First, consider Fig. 5-2(a) which is an example of a degenerate viewing geometry that can occur for clusters with fewer than four satellites. In this figure the satellites and the target are coplanar. There is a loss of dimensionality in this target tracking configuration orthogonal to the plane. Another issue that presents itself is if one of the satellites failed. It is possible for the two operational satellites in the cluster and the target to be collinear. If this particular tracking geometry were to occur, then the cluster would be incapable of determining the distance to the target.

Now consider a four satellite cluster that has been synthesized to maximize the tetrahedral volume. A cluster, such as the one in Fig. 5-2(b), avoids degenerate cluster/target geometries. A plane cannot be drawn through the cluster such that all of the satellites lie on a plane. Maximizing tetrahedral volume should provide an intuitive and dependable

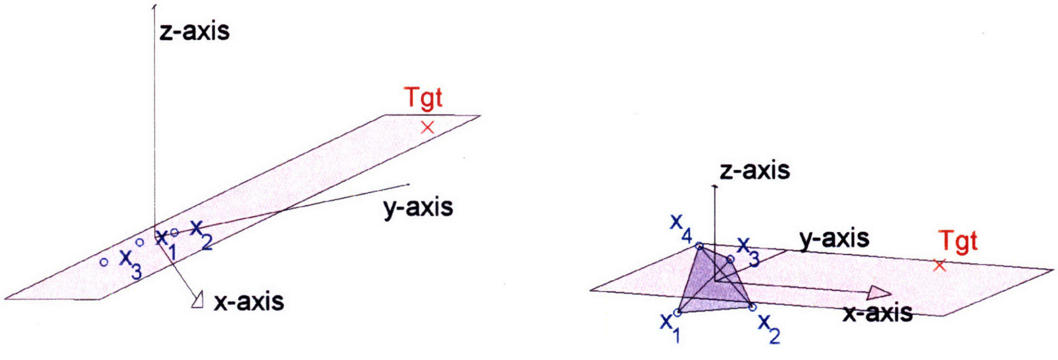

(a) Cartoon showing a degenerate cluster/target geometry that can occur with less than four satellites in the cluster. Regardless of the position of the satellites in the cluster a degenerate plane can always be found.

(b) Cartoon showing that a cluster designed with a tetrahedral volume avoids degenerate cluster/target relative geometry. There is no way to draw a plane through the cluster such that all the satellites and the target lie on a plane.

Figure 5-2: Cartoons showing hypothetical cluster configurations for three and four satellite clusters.

design heuristic because it avoids degenerate cluster/target relative geometries.

5.1.2 Cluster Baseline Size Validation

The derivation of the tetrahedral volume heuristic for cluster design was based on the assumption that $|\zeta| \gg |x_i|$. Thus, as the cluster baseline size approaches the distance to the target, the heuristic may not be valid. For example, consider the most obvious case where the target was actually inside the cluster. Then maximizing cluster volume would reduce target observability by increasing the satellite distances from the target; a cluster with a smaller tetrahedral volume would actually provide better target observability because the distances to the target would be less.

A simple experiment is used to estimate the baseline sizes for which this heuristic may be acceptable for cluster design. The acceptable baseline size criteria is expressed as a function of the ratio of cluster baseline and distance to target $\frac{\gamma}{\zeta}$ (see Fig. 5-3(a)). In the experiment, the cluster is assumed to be a regular tetrahedron (i.e., all sides are equal) and the cluster baseline size is incrementally increased until the D-optimality criterion also starts to increase ($-\ln\det(M)$). Smaller D-optimality values correspond to better target observability. Thus, the critical point is defined as the value of γ/ζ where the monotonic relationship between increasing cluster volume and decreasing $-\ln\det(M)$ ceases to exist. In Fig. 5-3(b), cluster volume and target observability are each plotted against $\frac{\gamma}{\zeta}$ and

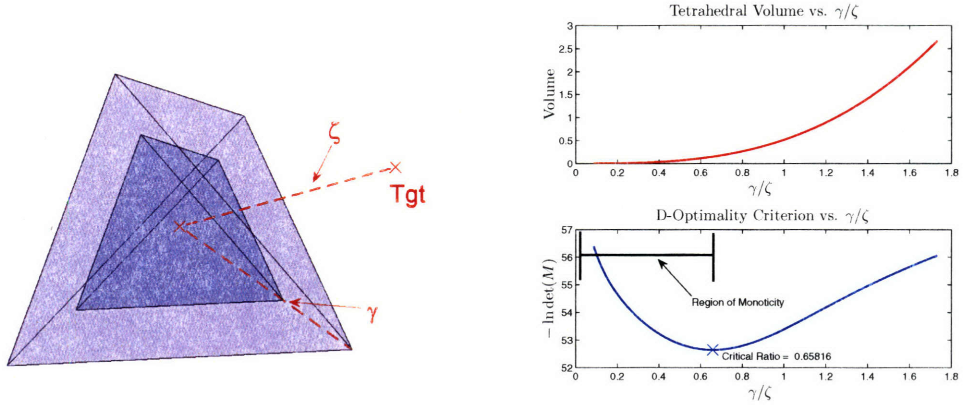

(a) Regular shaped tetrahedra with a random target position.

(b) Curves for D-optimality criterion and tetrahedral volume as a function of γ.

Figure 5-3: For this particular target position, the monotonic relationship between the D-optimality criterion and tetrahedral volume cease to exist when the critical ratio $(\frac{\gamma}{\zeta})$ is 0.65816.

volume always monotonically increases as a function of γ. However, for this particular relative geometry, $-\ln\det(M)$ monotonically decreases only when $\frac{\gamma}{\zeta} \leq 0.658$.

A thousand random target positions were chosen for the regular tetrahedral and the critical value of $\frac{\gamma}{\zeta}$ was found for each target position. Results showed an average critical value of $\frac{\gamma}{\zeta} = 0.759$ with a standard deviation of 0.126. Thus, maximizing volume of a cluster should be an acceptable approach when $\frac{\gamma}{\zeta}$ is less than approximately 0.633 (which statistically corresponds to approximately 84% of possible relative cluster/target geometries). This experiment, while only carried out for regularly shaped tetrahedra, demonstrates that the tetrahedral volume design heuristic is valid for all cluster baseline sizes considered in this research since distances to the target are often much larger than the cluster baseline size.

5.1.3 Cluster Average Tetrahedral Volume Figure-of-Merit

The cluster design figure-of-merit is the time average tetrahedral volume of the cluster because the cluster design objective is to provide good viewing geometry for a target in any direction at any point in time along the cluster's orbit. Thus, all points along the orbit have equal importance. The linearized state-transition matrices from Ref. [14] for satellite relative motion are again utilized to characterize the average tetrahedral volume of a cluster.

Thus, the average tetrahedral volume of a cluster is

$$V_{4\star} = \frac{1}{T}\sum_{j=1}^{T}\left\{\frac{1}{6}\sqrt{|\Sigma_{4\star}(t_j)\cdot\Sigma_{4\star}(t_j)^T|}\right\} \tag{5.14}$$

where

$$\Sigma_{4\star}(t_j) = \left[\begin{array}{ccc} \mathbf{x_1}(t_j) - \mathbf{x_2}(t_j) & \mathbf{x_2}(t_j) - \mathbf{x_3}(t_j) & \mathbf{x_3}(t_j) - \mathbf{x_4}(t_j) \end{array}\right] \tag{5.15}$$

and j is a discretization over the orbit of the cluster. In this study, a 60 second time step ($\Delta t = t_j - t_{j-1}$) is used to characterize a cluster's average tetrahedral volume.

5.2 Cluster Design Approach

5.2.1 Maximum Average Tetrahedral Volume

Optimization methods are used to synthesize the six relative orbital elements for each of the four satellites in a cluster to maximize the average tetrahedral volume. Maximum satellite separations are again constrained using the cubic baseline constraint (with $D^{max} = \{50, 100, 250, 500, 1000\}$ km) defined in Sec. 4.2.1 about the formation center. The nominal cluster design formulation to maximize the average tetrahedral volume is

$$\begin{aligned} J &= \max_{\delta \mathbf{e}_i} \; V_{4\star} \\ s.t. & \;\; |x_i(t)| \le d \\ & \;\; |y_i(t)| \le d \\ & \;\; |z_i(t)| \le d \\ & \;\; i \in (1,2,3,4) \\ & \;\; t \in (1,\ldots,T) \\ & \;\; d = \sqrt{\frac{1}{3}}D^{max} \end{aligned} \tag{5.16}$$

The constrained nonlinear program (MATLAB's built-in function *fmincon*) is again used to solve Eqn. 5.16.

5.2.2 Extension to N-Satellite Clusters

The average tetrahedral volume is a geometric characteristic of the cluster that has underlying mathematical properties. The heuristic can be easily extended to clusters with more than four satellites. Let Σ_N be defined as the $3 \times (N-1)$ matrix

$$\Sigma_N(t_j) = \Big[[\mathbf{x_1}(t_j) - \mathbf{x_2}(t_j)], [\mathbf{x_2}(t_j) - \mathbf{x_3}(t_j)], \ldots, [\mathbf{x_{N-1}}(t_j) - \mathbf{x_N}(t_j)]\Big] \tag{5.17}$$

Then the average projected three-dimensional parallelepiped volume of a cluster with N satellites is

$$V_N = \frac{1}{T}\sum_{j=1}^{T}\left\{\sqrt{\left|\Sigma_N(t_j) \cdot \Sigma_N(t_j)^T\right|}\right\} \tag{5.18}$$

Thus, the N-satellite cluster design formulation to provide uniform satellite distribution in the cluster and good viewing geometry for a target in any direction is

$$J = \max_{\delta\mathbf{e}_i} V_N \tag{5.19}$$

Five satellite clusters are designed with 50, 100, 250, 500, and 1000 km baselines and are compared to similar clusters with five satellites that were synthesized to minimize the average model-based value for the target position estimation error covariance from Chapter 4.

5.2.3 Design with a Penalty on J_2-Induced Relative Drift

Finally, four satellite, 250 km baseline clusters are designed to maximize the average tetrahedral volume with a penalty on J_2-induced relative drift (Λ) as previously defined in Sec. 4.2.2. The design formulation is

$$J = \min_{\delta\mathbf{e}_i} \; -R_{V_4} \cdot V_{4\star} + R_\Lambda \cdot \Lambda \tag{5.20}$$

and clusters are designed with several relative costs on average tetrahedral volume and J_2-induced relative drift ($\rho = R_\Lambda / R_{V_4}$).

5.2.4 Previous Approaches to Initializing Tetrahedral Formations

The tetrahedral shape of a formation of four satellites has been widely studied. In Ref. [25], Robert et al. emphasize the importance of the geometric shape of the tetrahedron on obtaining quality scientific data or successfully achieving mission requirements. Robert describes many ways to characterize the geometry of the tetrahedron based on its size, elongation and planarity.

Table 5.1: Dispersion values from nominal target trajectory used in the extended Monte Carlo simulation.

Orbital Parameter	Random Dispersion Values
a	±500 km
e	±0.1
i	±15°
Ω	±15°
ω	±10°
$f_{initial}$	±5°

Previously, Breger et al. [5] and Guzmán et al. [16] have both investigated techniques to initialize regularly shaped tetrahedron (where all sides are of equal length). Guzmàn studied initializing the cluster at different points along the orbit to see how the tetrahedron geometry would evolve with time. Breger studied ways to initialize a regular tetrahedron at a point in the orbit that are fuel optimal. Neither of these approaches are completely appropriate for the target tracking cluster considered in this study because size, rather than regularity, is the important design factor. Plus, both approaches only design the tetrahedron for a single point in the orbit. While Guzmán studies how the tetrahedron evolves, the evolution of the tetrahedron is not taken into account in the design formulation. For this reason, the design problem in this research is to maximize the average tetrahedral volume.

The design approach in this study is also different in the way that clusters with more than four satellites are initialized. Guzmán arbitrarily initializes a fifth satellite at the geometric center of the tetrahedron. In this study, the fifth satellite is not arbitrarily initialized. It is specifically used to improve the clusters target tracking capability.

5.3 Cluster Design and Simulation Results

All the cluster designed in this chapter are tested in the same high-fidelity Monte Carlo simulation testbed as previously described in Sec. 2.4 and 4.3. Average tracking results for targets in the occupancy corridor are reported. These simulation results are used to compare optimal measurement techniques for cluster design versus the cluster design heuristic that maximizes the average tetrahedral volume.

In addition to the nominal Monte Carlo simulations, an extended Monte Carlo simulation is utilized that perturbs the nominal target trajectory as described in Table 5.1. A total of

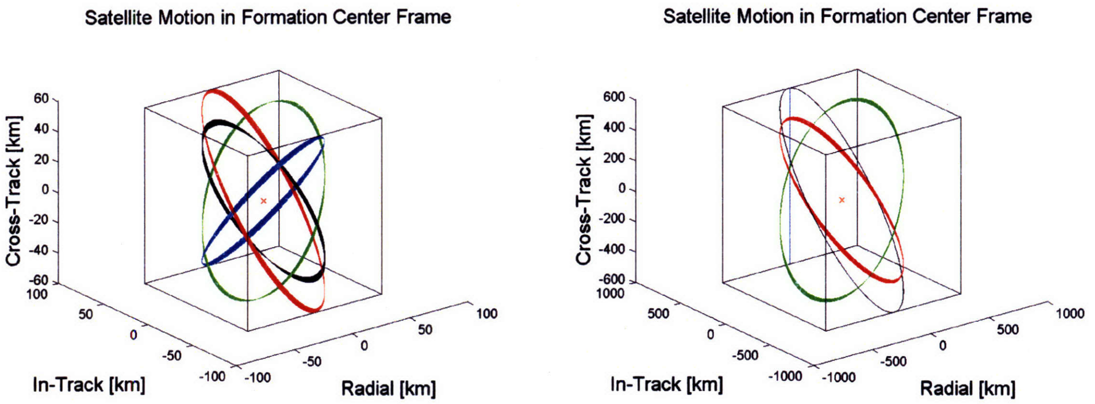

(a) 100 km baseline cluster.

(b) 1000 km baseline cluster.

Figure 5-4: Relative motion of satellites in clusters designed to maximize average tetrahedral volume.

340 cluster/target engagements are simulated (as opposed to 23 in the nominal Monte Carlo simulation). The purpose of the extended simulation is to provide a more likely dispersion of target trajectories that would be representative of a volumetric occupancy corridor.

5.3.1 Maximum Tetrahedral Volume Cluster Design

Model-based design results are presented in Table 5.2 for clusters with 50, 100, 250, 500 and 1000 km baselines and the relative satellite motion of 100 and 1000 km baseline clusters are provided in Fig. 5-4. These results are directly compared to four satellite clusters designed to minimize $O_{clust.}$ in Fig. 5-5. These model-based results predict that maximizing the average tetrahedral volume is a good heuristic for synthesizing a target tracking cluster—as the cluster baseline and average tetrahedral volume increases the average model-based value for the target position error estimation covariance decreases. The 50 km baseline cluster only has a predicted target position error covariance 1.5% higher than the *optimal* cluster. The larger 1000 km baseline was 32.5% higher. These predictions imply that the cluster design heuristic is better for smaller clusters than larger ones; this finding corresponds well with the previous assumption made that the distance to the target is much larger than the cluster baseline size in the derivation of the heuristic.

Monte Carlo simulation results for 100, 250, 500 and 1000 km baseline clusters are shown in Fig. 5-6. These results match model-based predictions and confirm that increasing the cluster baseline improves target tracking accuracy for a cluster designed to maximize average tetrahedral volume. Clusters designed to maximize average tetrahedral volume and those

Table 5.2: Model-based design results for four satellite clusters designed to maximize average tetrahedral volume are presented. Column two is the corresponding average model-based value for the target position estimation error covariance for a target in the occupancy corridor

Baseline (km)	Max Volume Cluster	
	Average Tetrahedral Volume (km^3)	$O_{clust.}$ (m^2)
50	10,000	146.7
100	80,000	140.5
250	1,248,000	118.3
500	10,138,000	99.9
1000	51,909,000	61.2

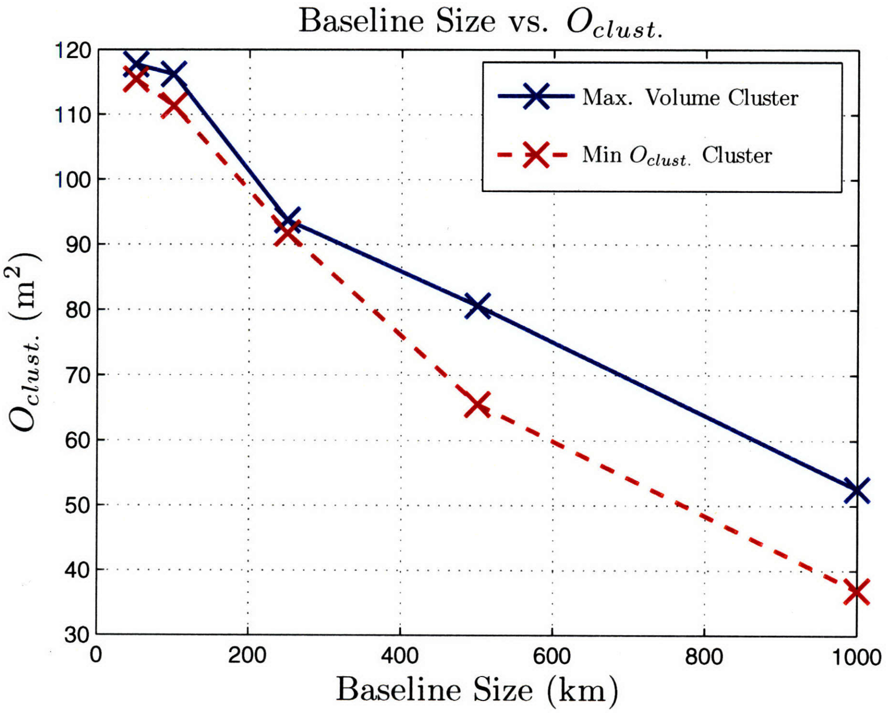

Figure 5-5: Model-based value for the target position estimation error covariance for four satellite clusters formulated with the different design approaches.

designed to minimize the average model-based value for the target position estimation error covariance perform similarly in simulation for the smallest simulated cluster (100 km). The difference in tracking performance increases as the cluster baseline size increases; this observation agrees with both model-based predictions and assumptions made when deriving the cluster design heuristic. These results reiterate that the average tetrahedral volume is a good, simple heuristic for cluster design. The relative motion of the satellites in the cluster was designed with no information about occupancy corridor and still provides similar tracking performance. This indicates that the smaller clusters, while they provide less overall tracking accuracy, are also less sensitive to relative geometry provided good distribution about the formation center is maintained.

Fig. 5-7 presents extended simulation tracking results for 1000 km baseline clusters. Even though there is a still a gap in tracking performance, the gap between the two clusters is smaller. A more interesting result is that the average tracking error the cluster designed with optimal measurement metrics increased by 53% and 70% for estimated and true position tracking error between nominal and extended simulations. However, the cluster designed to maximize tetrahedral volume only showed a 12% increase in estimated tracking error and actually a reduced true tracking error of 27%. Even though the tracking error is higher, the cluster designed to maximize tetrahedral volume has a tracking capability that is more robust to target trajectory uncertainty. A small sample of target trajectories in the nominal trajectory more accurately represented the cluster's tracking capability for a realistic dispersion of target trajectories in the extended simulation than a cluster designed with optimal measurement metrics. These findings support the prediction that designing a cluster to maximize average tetrahedral volume is an appropriate heuristic that ensures good (robust) tracking capability in the limit when there is no prior information of the target position and trajectory.

5.3.2 Extension to N-Satellite Cluster Design

The relative satellite motion presented in Fig. 5-8 is for 100 km and 1000 km baseline clusters with five satellites designed to maximize the average projected three-dimensional parallelepiped volume. Average model-based expected target position covariance results are reported in Fig. 5-9 and are compared to corresponding clusters designed to minimize the average model-based value for the target position estimation error covariance. Again

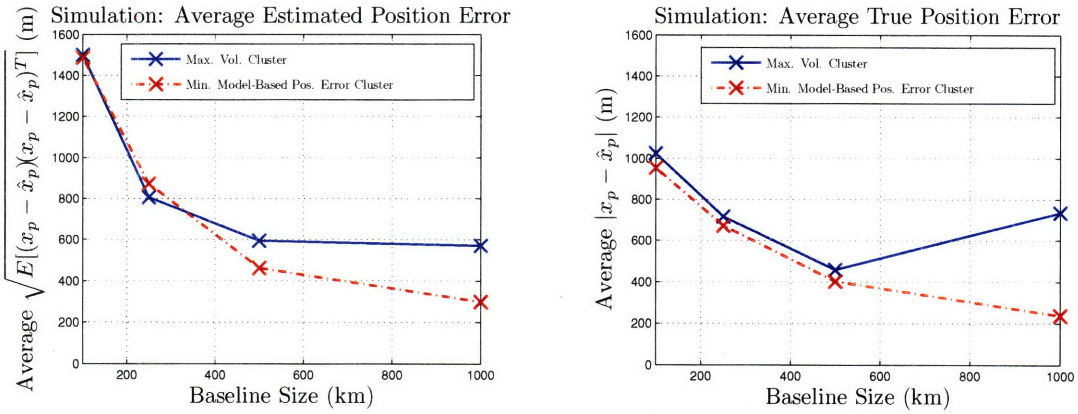

(a) Comparison of estimated target position error standard deviation reported from Kalman filter after convergence in nominal Monte Carlo simulations.

(b) Comparison of average target position tracking error after filter convergence in nominal Monte Carlo simulations.

Figure 5-6: Comparison of nominal Monte Carlo simulation results for clusters designed to minimize the average model-based value for the target position estimation error covariance and clusters designed to maximize the average tetrahedral volume.

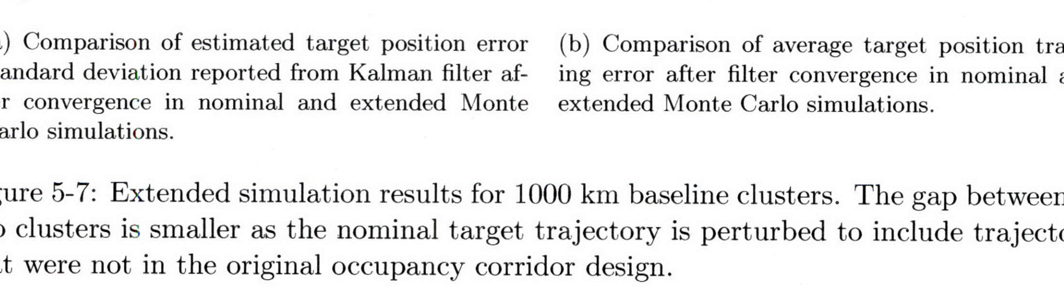

(a) Comparison of estimated target position error standard deviation reported from Kalman filter after convergence in nominal and extended Monte Carlo simulations.

(b) Comparison of average target position tracking error after filter convergence in nominal and extended Monte Carlo simulations.

Figure 5-7: Extended simulation results for 1000 km baseline clusters. The gap between the two clusters is smaller as the nominal target trajectory is perturbed to include trajectories that were not in the original occupancy corridor design.

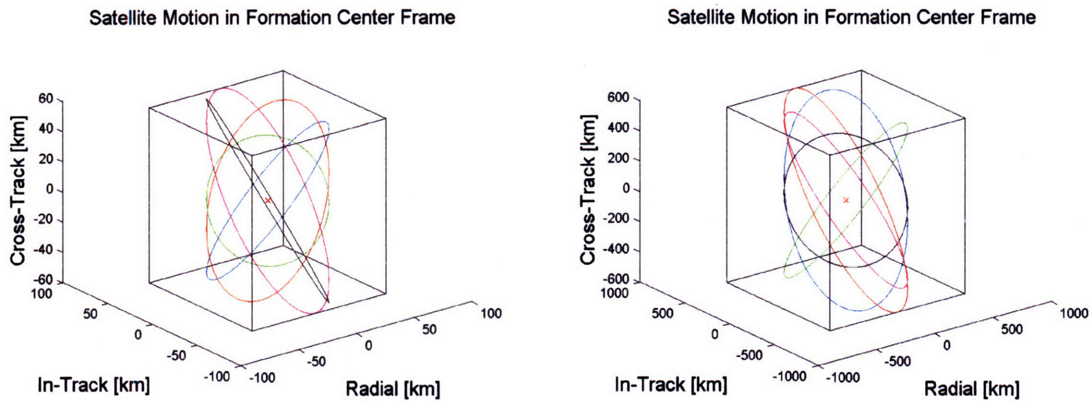

(a) 100 km Baseline.

(b) 1000 km Baseline.

Figure 5-8: Relative motion of five satellite clusters designed to maximize the average projected parallelepiped volume.

model-based predictions suggest that the design heuristic is very accurate for the smallest cluster, which has an average model-based value for the target position estimation error covariance 2% higher. The largest cluster (1000 km) is 42% higher.

Nominal simulation results are presented in Fig. 5-10. The two clusters designed to maximize the average projected three-dimensional parallelepiped volume and to minimize the estimated tracking error perform even more alike than the four satellite cluster configurations did. The difference in simulation tracking performance between the two cluster configurations is indiscernible. In the previous chapter, increasing the number of satellites in the cluster did not improve tracking accuracy. However, increasing the number of satellites for a cluster designed to maximize the projected parallelepiped volume reduces the gap in tracking performance with a cluster designed to minimize the average value for the target position estimation error covariance. This suggests that adding satellites to a cluster designed to maximize the average projected parallelepiped volume can improve the tracking accuracy of a cluster.

5.3.3 Maximum Volume plus J_2-Invariance Cluster Design

Design results for four satellite, 250 km clusters with a range of relative costs on average tetrahedral volume and J_2-induced relative drift are presented in Table 5.3. Again, results show that a cluster can be designed that exhibits minimal relative satellite drift with little to no degradation in estimated tracking accuracy (and, in this case, average tetrahedral volume). The average expected ΔV consumption is reduced by three orders of magnitude

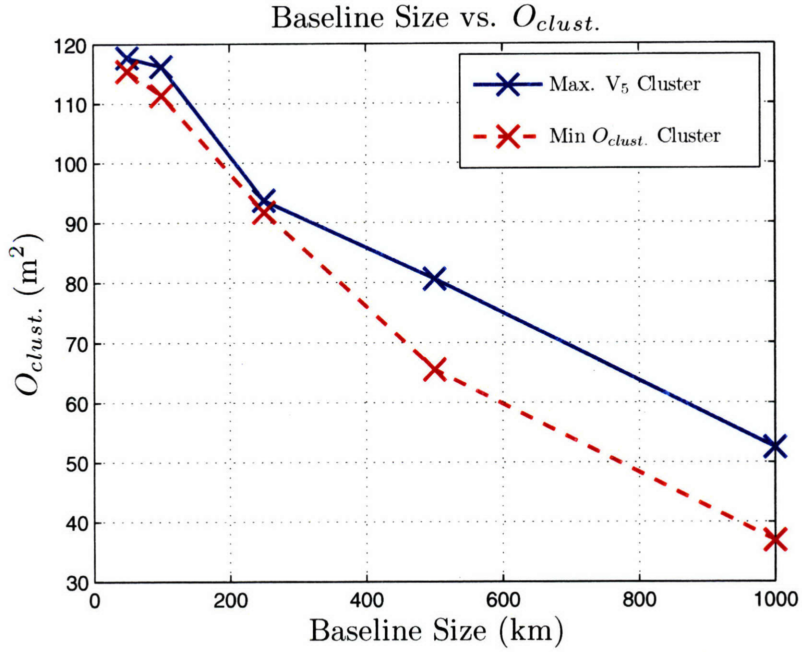

Figure 5-9: Model-based results for five satellite clusters designed to maximize the average projected parallelepiped volume of the cluster are compared to five satellite clusters that minimized $O_{clust.}$.

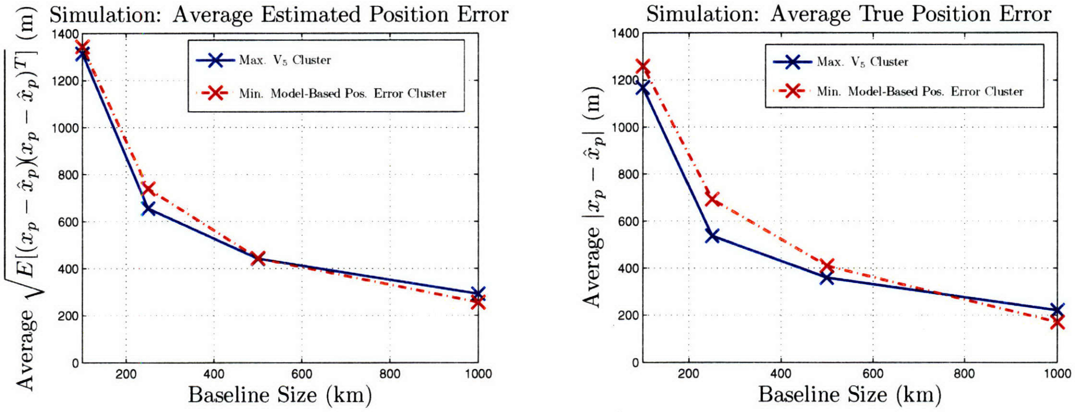

(a) Comparison of estimated target position error standard deviation reported from Kalman filter after convergence in nominal Monte Carlo simulations.

(b) Comparison of average target position tracking error after filter convergence in nominal Monte Carlo simulations.

Figure 5-10: Comparison of nominal Monte Carlo simulation results for five satellite configurations.

Table 5.3: Model-based results for four satellite clusters designed with a range of relative costs on average tetrahedral volume and J_2-induced relative satellite drift ($\rho = R_d/R_{V_4}$).

ρ	Expected ΔV (m/s/orbit)	Average Tetrahedral Volume (km^3)	Average Model-Based Estimation Error (m^2)
0	0.01371	1,267,200	128.6
$2.5 \cdot 10^5$	0.01023	1,266,900	127.8
$1.25 \cdot 10^6$	0.00831	1,266,800	127.8
$5.0 \cdot 10^6$	0.00003	1,247,000	128.3

Table 5.4: Simulation results for four satellite clusters designed with a range of relative costs on tetrahedral volume and J_2-induced relative satellite drift (ρ).

ρ	Average Estimated Position Error (m)	Average True Position Error (m)
0	887.7	822.7
$2.5 \cdot 10^5$	1020.3	863.0
$1.25 \cdot 10^6$	828.5	737.9
$5.0 \cdot 10^6$	884.2	879.5

and the average tetrahedral volume is only reduced by 1.6%. Plus, the average model-based estimation error covariance is actually the worst for the cluster designed without a penalty on J_2-induced relative drift. This result suggests that there is no correlation between ρ and tracking accuracy when designing a cluster to maximize average tetrahedral volume.

Simulation results for the range of relative cost clusters are presented in Table 5.4. There is no major difference in tracking performance between these clusters. While the second cluster has an estimated tracking error 200 m higher than the other clusters, it's true tracking performance is nearly identical.

5.4 Chapter Summary

This chapter presented a cluster design heuristic that provides good cluster viewing geometry for a target in any direction. The average tetrahedral volume cluster design heuristic for clusters with four satellites was derived directly from the information matrix and was extended to clusters with more than four satellites. In addition, results in this chapter demonstrated again that a cluster can be designed thats exhibits little relative satellite drift with minimal reduction in the cluster's average tetrahedral volume (and, effectively, target tracking capability).

There are many benefits for using tetrahedral volume as a heuristic for cluster design over optimal measurement principles. First, for several space-based missions such as tracking satellites or space debris the target of interest could realistically be in any direction at any point in time. Optimal measurement techniques required that the occupancy corridor be specifically defined. In real tracking scenarios that is rarely be possible. There would typically be a wide range of potential trajectories that would need to be considered. Second, the tetrahedral volume design heuristic provides a cluster geometry metric (about the formation center which was specifically synthesized for the occupancy corridor) that is robust to target position uncertainty. This metric and results in this chapter suggest that there is little justification to synthesize the relative motion of the microsatellites in the cluster with the same optimal measurement metrics used to design the formation center. Finally, designing a cluster to maximize the average tetrahedral volume has an added benefit that it extracts the target occupancy corridor from the synthesis of the microsatellites' relative motion about the formation center. Average tetrahedral volume is a more spatially intuitive metric for cluster design.

Part II

Cluster Maintenance and Control

THIS PAGE INTENTIONALLY LEFT BLANK

Chapter 6

Cluster Maintenance and Control

This chapter investigates strategies to mitigate and correct the cluster configuration when drift inevitably degrades the cluster's viewing configuration. The objective of the research is to accommodate the reconfiguration in order to minimize cluster-wide fuel consumption while maintaining geometric characteristics of the cluster that ensure minimum target tracking criteria. A receding horizon model predictive control (MPC) algorithm is proposed that minimizes total fuel consumption subject to constraints on maximum cluster baseline and minimum average volume. Tillerson et al. demonstrated that a model predictive controller can be used for formation flying missions [37, 38, 36, 39]. Breger et al. expanded on the work of Tillerson by developing a time-varying form of the relative equations of motion based on Gauss's variational equations [4, 5]. In addition, Breger has demonstrated initializing a spacecraft formation with partial J_2-invariance as well as using a *virtual center* to minimize relative satellite state errors [6, 7]. This research capitalizes on many of these important contributions in developing the control architecture considered in this chapter. Important technical considerations of this chapter are the inclusion of J_2-induced relative drift as a terminal cost in a multi-objective MPC scheme and the concept of a *variable formation center.*

Results from this chapter show fuel consumption rates less than would be expected from a control scheme that simply reestablishes the relative orbital elements of the satellites in the cluster ($\delta \mathbf{e}_\mathbf{i}$) every orbit. More importantly, observations from this chapter confirm that initializing a cluster with low J_2-induced relative drift rates reduces cluster wide fuel consumption. In addition, including J_2-induced relative drift as a terminal cost does not guarantee reduced fuel consumption due to higher order gravitational disturbances. Implementation of a variable formation center, though, demonstrates reduced fuel consumption by minimizing the effect of cluster-wide motion and unmodeled disturbances such as J_3 in the linearized relative motion dynamic model.

This chapter's outline is as follows: The cluster control problem and approach are presented in Sec. 6.1. The proposed control architecture uses an outer-loop and inner-loop approach. The inner-loop is satellite specific and described in Sec. 6.2. A description of the outer-loop algorithm is presented in Sec. 6.3, as well as a multi-objective MPC algorithm and a variable formation center. Finally, simulation results are presented in Sec. 6.4.

6.1 Cluster Control Problem and Approach

In Chapter 4, a control scheme that reestablished mean relative orbital elements every orbit was used to predict expected ΔV consumption rates for a target tracking cluster. If such a control scheme were used, the effective lifetime of the cluster could be extremely short. Previously designed clusters in Chapter 4 required unacceptable ΔV consumption rates as high as 1 m/s/orbit to maintain relative orbital elements due to J_2-induced relative drift. However, maintaining mean relative orbital elements is not a mission requirement for a cluster of target tracking satellites. In Chapter 5, for example, sub-optimal clusters still provided acceptable target tracking capability (i.e., cluster designed to maximize the average tetrahedral volume). An intelligent control algorithm would allow satellite drift as long as certain mission driven cluster characteristics were maintained. Those characteristics for a target tracking cluster are limits on maximum inter-satellite separation and acceptable cluster geometry. In order to guarantee that the microsatellites can communicate with each other, microsatellites may not drifts so far apart that communication within the cluster is impossible. Bad geometries that may occur due to relative satellite drift can interfere with the cluster's ability to track an object with acceptable precision or speed of convergence. The controller must ensure that the microsatellites do not all agglomerate about each other.

This research proposes an MPC algorithm to approach the cluster maintenance problem. MPC is a *closed-loop* control strategy that uses an internal model of the system to predict the future behavior of the system and determine the control sequences that minimize an objective function. The strategy is to solve for the control sequence over a finite planning horizon and then only carry out a portion of the control sequence. The control sequence is then re-obtained using the current state, system model and objective function. The control sequence that minimizes the objective function is solved for using optimization techniques. MPC has several advantages over classic control approaches. It allows for control and state constraints to be explicitly taken into account. In addition, it can accommodate nonlinear and time- or parameter-varying dynamic models. Typical objective functions penalize either the state of the system, the control sequence or a combination of the two [12, 17].

The control strategy in this research involves cluster reconfiguration over one reconfiguration orbit and then requires several consecutive observing orbits. A satellite's estimate of its own position, velocity, and attitude degrades whenever a satellite applies an impulsive thrust maneuver to change its orbit. Thus, a microsatellite would not be able to track an object in space well if it were constantly firing its thrusters or had just recently completed an impulsive maneuver. Minimizing how often cluster reconfiguration occurs is a mission necessity for target tracking missions.

The proposed MPC algorithm in this research has two components: (1) an outer-loop control algorithm and (2) an inner-loop, satellite specific control algorithm (see Fig. 6-1). The outer-loop control algorithm determines the relative states of the satellites in the cluster necessary to maintain maximum cluster baseline and average minimum tetrahedral volume. The algorithm estimates the cost of changing relative orbital elements over an orbit but does not actually calculate the impulsive maneuvers. The outer-loop algorithm is fully described in Sec. 6.3. The inner-loop algorithm calculates the optimal impulsive maneuvers that minimize the one-norm ΔV to achieve the desired orbital element differences for each satellite as defined by the outer-loop algorithm. The inner-loop algorithm uses convex numerical optimization techniques to solve a linear system of equations that minimizes the one-norm ΔV required to establish the orbital element differences. This control approach (the inner-loop) for formation flying missions has been recently studied and demonstrated to be very accurate and efficient [39, 7, 5, 4]. The inner-loop formulation is presented in Sec. 6.2.

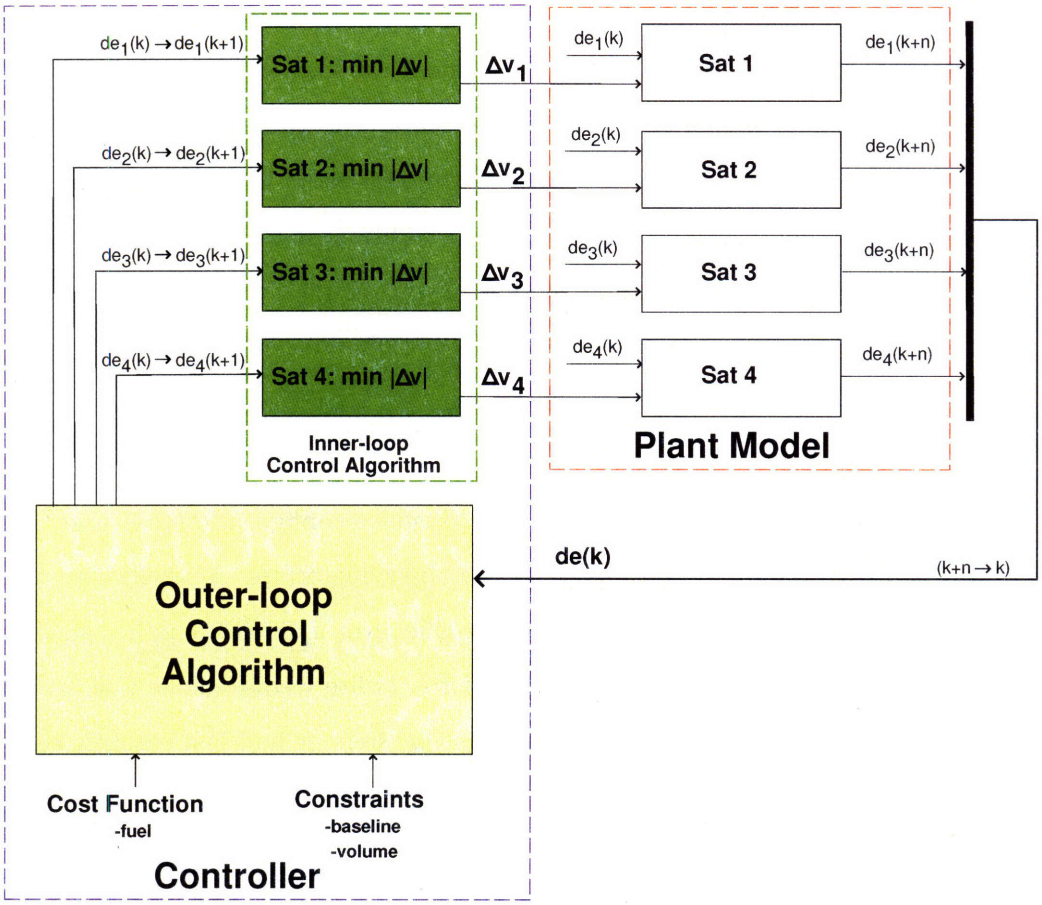

Figure 6-1: Proposed control architecture design.

6.2 Inner-loop Controller Description

In Refs. [39, 7, 5, 4], Tillerson et al. and Breger et al. demonstrated model predictive controllers using a linearized dynamic model for satellite formation flying missions. The controller is implemented as a linear program and the general form is given by

$$\begin{aligned} J &= \min \ ||U||_1 \\ s.t \ \ & \mathbf{A}U \leq \mathbf{b} \end{aligned} \tag{6.1}$$

The matrices **A** and **b** are based on the dynamics and constraints of the formation flying mission and U is a vector of admissible control inputs with the form [7]

$$U = \begin{bmatrix} \mathbf{u_i}(1)^T & \mathbf{u_i}(2)^T & \ldots & \mathbf{u_i}(n-1)^T & \mathbf{u_i}(n-1)^T \end{bmatrix}^T \tag{6.2}$$

For typical spacecraft missions, those inputs are a series of impulses (or Δv maneuvers) distributed about the entire planning horizon.

The state transition matrices $\phi(t_j, t_{j+1})$ developed in Ref. [14] are used as a valid set of linearized dynamics for implementation of the controller in this research. These state transition matrices were first demonstrated as an acceptable model for MPC in formation flying missions in Ref. [5]. The discrete control effect matrix is calculated using the *Rectilinear Dynamics Discretization* method described by Breger in Ref. [7]. The discrete control effect matrix is

$$\Gamma(t) = M_{\mathbf{x}\to\delta\mathbf{e}}(\mathbf{e_{fc}}(t)) \begin{bmatrix} \frac{(\Delta t)^2}{2} I_3 \\ (\Delta t) I_3 \end{bmatrix} \tag{6.3}$$

where $M_{\mathbf{x}\to\delta\mathbf{e}}$ is fully defined in Ref. [33]. The Γ matrix is calculated by assuming the input can be modeled as a set of rectilinear equations of motion, which are then rotated into the relative orbital element set. Thus, the input vectors are Δv impulses in the three orthogonal directions in the Cartesian coordinate frame defined about the formation center ($\mathbf{u_i} = (\Delta v_x, \Delta v_y, \Delta v_z)^T$). This approach is very accurate for LEO missions [7].

For the controller architecture in Fig. 6-1, the outer-loop control algorithm provides a commanded state for each spacecraft after one reconfiguration orbit. Therefore, the objective function in the inner-loop controller is to choose the Δv impulses that minimize the one-norm sum such that the relative orbital elements after one orbit $\delta\mathbf{e_i}(t_p)$ is equal to the commanded state from the outer-loop control algorithm (the time difference $t_p - t_0$ is equal to the orbital period of the formation center). Defining

$$\bar{\phi}(j,k) = \prod_{i=j}^{k-1} \phi(t_i, t_{i+1}) \tag{6.4}$$

the linear optimization problem in the inner-loop is

$$\begin{aligned} J &= \min ||U||_1 \\ &s.t.\ \ \mathbf{A}U = \mathbf{b} \end{aligned} \tag{6.5}$$

where

$$\mathbf{A} = \begin{bmatrix} \bar{\phi}(0,p)\Gamma(t_0) & \bar{\phi}(1,p)\Gamma(t_1) & \dots & \bar{\phi}(p-2,p)\Gamma(t_{p-2}) & \bar{\phi}(p-1,p)\Gamma(t_{p-1}) \end{bmatrix} \tag{6.6}$$

and

$$\mathbf{b} = \delta\mathbf{e_i}(t_p) - \bar{\phi}(0, p)\delta\mathbf{e_i}(t_0) \tag{6.7}$$

The inner-loop controller is run on each satellite in the cluster and a time step (Δt) of ten seconds is used. The ΔV impulses are evenly distributed over 100 points along the orbit in this study.

6.3 Outer-loop Cluster Control Algorithm Design

The purpose of this section is to describe the outer-loop control algorithm studied in this chapter. The outer-loop controller solves for the commanded $\delta\mathbf{e_i}$'s necessary to maintain the maximum cluster baseline and minimum average volume that minimize an estimated ΔV required to obtain the $\delta\mathbf{e_i}$'s in the cluster. In Sec. 6.3.1 simple analytic control schemes are compared in order to estimate the ΔV required to establish desired orbital element differences over one orbit. The finite horizon, linearized propagation model is then given in Sec. 6.3.2 and the nominal outer-loop MPC formulation is provided in Sec. 6.3.3. Variations to the nominal control algorithm considered in this chapter include a multi-objective MPC algorithm that also penalizes J_2-induced relative drift (Sec. 6.3.4) and a control algorithm with a variable formation center (Sec. 6.3.5). Finally, planning horizon and admissible reconfiguration orbits are addressed in Sec. 6.3.6.

6.3.1 Analytic Impulsive Control Schemes

Researchers have recently studied fuel optimal, analytic control algorithms to establish small desired orbital element differences. The most common approaches to the analytic control problem utilize Gaussian variational equations (Eqn. 2.17). These approaches (of which three are compared) replace the three orthogonal acceleration vectors (a_r, a_θ, a_h) from Gauss' variational equations with Δv impulses $(\Delta v_r, \Delta v_\theta, \Delta v_h)$ at different points along the orbit to establish the desired orbital element differences. In this section, three analytic control algorithms are compared to the inner-loop control algorithm [4, 5].

Three Impulse Scheme

A three impulse scheme derived by Schaub and Alfriend in Ref. [30] is calculated directly from the Gaussian variational equations that assumes all the $\Delta\mathbf{e}$'s are relatively small. The scheme couples the corrections for Ω and i, since out-of-plane corrections are generally more fuel expensive than in-plane ones. The magnitude of the coupled out-of-plane impulse is

$$\Delta v_h = \frac{h}{r}\sqrt{\Delta i^2 + \Delta\Omega^2 \sin i^2} \tag{6.8}$$

and this correction occurs at

$$\theta_c = \arctan\frac{\Delta\Omega \sin i}{\Delta i} \tag{6.9}$$

Next, a radial firing at both orbital perigee and apogee are used to control w and M

$$\begin{aligned} \Delta v_{r_p} &= -\frac{na}{4}\left(\frac{(1+e)^2}{\eta}(\Delta\omega + \Delta\Omega\cos i) + \Delta M\right) && (6.10) \\ \Delta v_{r_a} &= \frac{na}{4}\left(\frac{(1-e)^2}{\eta}(\Delta\omega + \Delta\Omega\cos i) + \Delta M\right) && (6.11) \end{aligned}$$

Finally, the remaining orbital elements (a and e) are controlled using in-track firings that also occur at orbital perigee and apogee

$$\begin{aligned} \Delta v_{\theta_p} &= \frac{na\eta}{4}\left[\frac{\Delta a}{a} + \frac{\Delta e}{1+e}\right] && (6.12) \\ \Delta v_{\theta_a} &= \frac{na\eta}{4}\left[\frac{\Delta a}{a} - \frac{\Delta e}{1-e}\right] && (6.13) \end{aligned}$$

Thus, the total fuel budget for the three impulse scheme derive in Ref. [30] is

$$\Delta V_{3imp} = \Delta v_h + \sqrt{\Delta v_{r_p}{}^2 + \Delta v_{\theta_p}{}^2} + \sqrt{\Delta v_{r_a}{}^2 + \Delta v_{\theta_a}{}^2} \tag{6.14}$$

Two Impulse Scheme

In Ref. [41], Vaddi derives a similar impulsive control algorithm, except that the radial and tangential impulses to correct $(\Delta a, \Delta e, \Delta\omega, \Delta M)$ are directly coupled with two out-of-plane firings to control Δi and $\Delta\Omega$. To begin, Vaddi splits Eqn. 6.8 into two impulses phased 180° apart such that Δv_{h_1} occurs at $\theta_1 = \theta_c$ and Δv_{h_2} at $\theta_2 = \theta_c + \pi$

$$\begin{aligned} \Delta v_{h_1} &= \frac{h}{2r}\sqrt{\delta i^2 + \delta\Omega^2 \sin i^2} && (6.15) \\ \Delta v_{h_2} &= -\frac{h}{2r}\sqrt{\delta i^2 + \delta\Omega^2 \sin i^2} && (6.16) \end{aligned}$$

Vaddi then derives the necessary radial and tangential impulses at θ_1 and θ_2 to establish the remaining orbital element differences. These four impulses are directly solved for since there are four remaining orbital element differences that need to be achieved in Eqn. 6.17.

$$\begin{bmatrix} \Delta a \\ \Delta e \\ \Delta\omega + \cos i \Delta\Omega \\ \Delta M \end{bmatrix} = A \cdot \begin{bmatrix} \Delta v_{r_1} \\ \Delta v_{\theta_1} \\ \Delta v_{r_2} \\ \Delta v_{\theta_2} \end{bmatrix} \tag{6.17}$$

where

$$A(:,1:2) = \begin{bmatrix} \frac{2a^2 e}{h}\sin f_1 & \frac{2a^2}{h}(1+e\cos f_1) \\ \frac{p}{h}\sin f_1 & \frac{p}{h}\left[\frac{2+e\cos f_1}{1+e\cos f_1}\cos f_1 + \frac{e}{1+e\cos f_1}\right] \\ -\frac{p}{he}\cos f_1 & \frac{p}{he}\left[\frac{2+e\cos f_1}{1+e\cos f_1}\sin f_1\right] \\ \frac{\eta}{he}(p\cos f_1 - 2r_1 e) - \frac{3\pi a}{h}e\sin f_1 & -\frac{\eta}{he}(p+r_1)\sin f_1 - \frac{3\pi a p}{h r_1} \end{bmatrix}$$

$$A(:,3:4) = \begin{bmatrix} \frac{2a^2 e}{h}\sin f_2 & \frac{2a^2}{h}(1+e\cos f_2) \\ \frac{p}{h}\sin f_2 & \frac{p}{h}\left[\frac{2+e\cos f_2}{1+e\cos f_2}\cos f_2 + \frac{e}{1+e\cos f_2}\right] \\ -\frac{p}{he}\cos f_2 & \frac{p}{he}\left[\frac{2+e\cos f_2}{1+e\cos f_2}\sin f_2\right] \\ \frac{\eta}{he}(p\cos f_2 - 2r_2 e) & -\frac{\eta}{he}(p+r_2)\sin f_2 \end{bmatrix}$$

The remaining elements of the two impulse control scheme can be found by solving $\Delta\mathbf{v} = A^{-1}\Delta\mathbf{e}$. The ΔV budget for the two impulse control scheme is

$$\Delta V_{2imp} = \sqrt{{\Delta v_{r_1}}^2 + {\Delta v_{\theta_1}}^2 + {\Delta v_{h_1}}^2} + \sqrt{{\Delta v_{r_2}}^2 + {\Delta v_{\theta_2}}^2 + {\Delta v_{h_2}}^2} \tag{6.19}$$

Six Impulse Scheme

A six impulse scheme is also considered in this experiment that is a linear function of the orbital element differences and is similar to the three impulse method presented in Sec. 6.3.1. Instead of coupling the out-of-plane firings, though, an impulsive firing at $\theta^o = 0$ is used to control i and one at $\theta = 90^o$ controls Ω

$$\Delta v_{h_{0^o}} = \frac{h}{r}\Delta i \tag{6.20}$$

$$\Delta v_{h_{90^o}} = \frac{h\sin i}{r}\Delta\Omega \tag{6.21}$$

The decoupled out-of-plane impulses will require no more than 42% more fuel over all possible inclinations and values of $\frac{\Delta\Omega}{\Delta i}$ (see Fig. 6-2). The tangential and radial impulses at perigee and apogee in the three impulse scheme to control $(\delta a, \delta e, \delta\omega, \delta M)$ are already linear functions and remain the same for the six impulse scheme. The required six impulses can then be calculated using the linear relationship

$$\begin{bmatrix} \Delta v_{h_{0^o}} \\ \Delta v_{h_{90^o}} \\ \Delta v_{r_p} \\ \Delta v_{r_a} \\ \Delta v_{\theta_p} \\ \Delta v_{\theta_a} \end{bmatrix} = \begin{bmatrix} 0 & 0 & \frac{h}{r} & 0 & 0 & 0 \\ 0 & 0 & 0 & -\frac{na(1+e)^2}{4\eta}\cos i & -\frac{na(1+e)^2}{4\eta} & -\frac{na(1+e)^2}{4\eta} \\ 0 & 0 & 0 & \frac{na(1-e)^2}{4\eta}\cos i & \frac{na(1-e)^2}{4\eta} & \frac{na(1-e)^2}{4\eta} \\ 0 & 0 & 0 & \frac{h\sin i}{r} & 0 & 0 \\ \frac{na\eta}{4a} & \frac{1}{1+e} & 0 & 0 & 0 & 0 \\ \frac{na\eta}{4a} & -\frac{1}{1-e} & 0 & 0 & 0 & 0 \end{bmatrix} \begin{bmatrix} \Delta a \\ \Delta e \\ \Delta i \\ \Delta\Omega \\ \Delta\omega \\ \Delta M \end{bmatrix} \tag{6.22}$$

The total fuel budget for this control scheme is the one-norm sum (instead of the two-norm as previously calculated)

$$\Delta V_{6imp} = |\Delta v_{h_0}| + |\Delta v_{h_{90}}| + |\Delta v_{r_p}| + |\Delta v_{r_a}| + |\Delta v_{\theta_p}| + |\Delta v_{\theta_a}| \tag{6.23}$$

Scheme Comparison

The three different impulsive control schemes are compared to the *optimal solution* solved for using the inner-loop algorithm to determine the optimality of each algorithm in a similar manner as described in Ref. [7]. In the experiment, there is a nominal trajectory (Table 6.1) about which the satellite has been perturbed by some random error

$$(\Delta a, \Delta e, \Delta i, \Delta\Omega, \Delta\omega, \Delta M)^T = 10^{-6} \cdot \text{rand}(1,6)^T \tag{6.24}$$

The ΔV required by each algorithm is calculated to reestablish the satellite to the nominal trajectory. This experiment was carried out a thousand times and Table 6.2 presents the average percentage more fuel required for each of the analytic control schemes than the optimal solution. As is expected, the control strategy that coupled the firings together into two impulses performed the closest to the optimal solution. Conversely, decoupling both

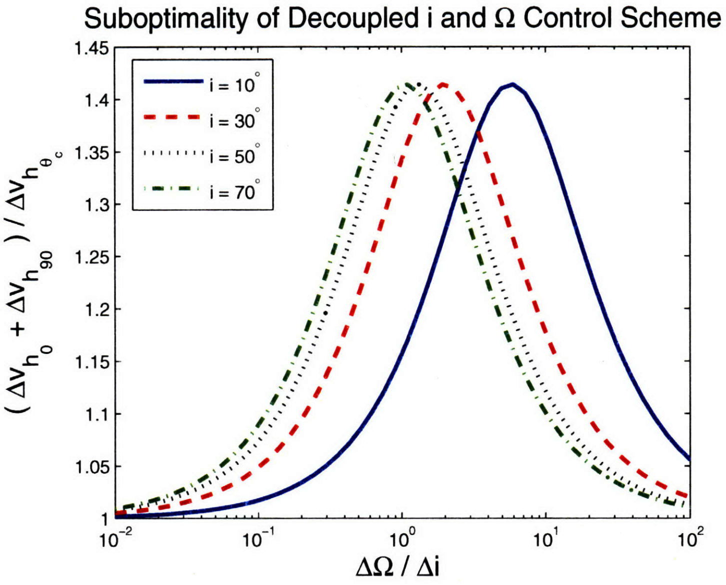

Figure 6-2: Plot for the ratio of Δv required for two decoupled impulses to establish Δi and $\Delta\Omega$ and a single coupled impulse at θ_c. The plot assumes that radius of the orbit at each firing (or θ) is the same.

Table 6.1: Nominal orbital parameters for control scheme comparison.

Parameter	Value
a	7555 km
e	0.05
i	48°
Ω	20°
ω	10°
M	120°

the out-of-plane firings and the radial and tangential firings at apogee and perigee was the most ΔV costly.

However, for a first approximation the six impulse scheme could be used to estimate cluster wide fuel consumption. The six impulse scheme is desirable because it can be linearly posed. Thus, a discretization of the equinoctial variational equations (see Eqn. 2.18) is used to estimate the ΔV required to achieve desired orbital element differences over one orbit by assuming radial and tangential Δv's at perigee and apogee. Likewise, out-of-plane firings occur at $\theta = 0°$ and $\theta = 90°$ to control i and Ω.

Table 6.2: Scheme comparison results. Results presented are the average percent more ΔV required to reestablish the nominal orbital elements than that calculated by the optimal solution.

Control Scheme	Percent More ΔV than the Optimal Solution
ΔV_{3imp}	72%
ΔV_{2imp}	68%
ΔV_{6imp}	116%

6.3.2 Linearized Dynamic Propagation Model

A high-fidelity state transition matrix over one orbit $\Psi(k, k+1)$ is calculated by multiplying several small time step linearized state transition matrices $\phi(t_j, t_{j+1})$ from Ref. [14]

$$\Psi(k, k+1) = \prod_{j=0}^{p-1} \phi(t_j, t_{j+1}) \tag{6.25}$$

A time step ($\Delta t = t_{j+1} - t_j$) of 5 seconds is used in this study and $t_p - t_0$ is equal to the orbital period of the formation center. The finite horizon, predictive linearized dynamic propagation model admits a reconfiguration orbit every n orbits where T is the number of reconfiguration orbits in the outer-loop control algorithm. Thus, the planning horizon in the outer-loop algorithm is $T \cdot n$ orbits. The linearized model for a single satellite ($\delta \mathbf{e_i}$) is

$$\delta \mathbf{E_i} = H \cdot \delta \mathbf{e_i}(0) + G \cdot \mathbf{U_i} \tag{6.26}$$

where the relative orbital element state vector is

$$\delta \mathbf{E_i} = \begin{bmatrix} \delta \mathbf{e_i}(1)^T & \delta \mathbf{e_i}(2)^T & \dots & \delta \mathbf{e_i}(T \cdot n - 1)^T & \delta \mathbf{e_i}(T \cdot n)^T \end{bmatrix}^{\mathbf{T}} \tag{6.27}$$

The matrix H propagates the initial satellite relative orbital elements $\delta \mathbf{e_i}(0)$ through the planning horizon. It is

$$H = \begin{bmatrix} \Psi(0,1) \\ \Psi(0,2) \\ \vdots \\ \Psi(0, T \cdot n - 1) \\ \Psi(0, T \cdot n) \end{bmatrix} \tag{6.28}$$

The candidate control actuation (or decision variable) vector is

$$\mathbf{U}_{\mathbf{i}} = \begin{bmatrix} \Delta V_i(1)^T & \Delta V_i(n)^T & \dots & \Delta V_i((T-1)\cdot n)^T \end{bmatrix}^T \tag{6.29}$$

and $\mathbf{U}_{\mathbf{i}}$ is multiplied by the control sensitivity matrix G

$$G = \begin{bmatrix} B & 0 & \dots & 0 \\ \vdots & \vdots & & \\ \Psi(1,n)\cdot B & 0 & & \vdots \\ \Psi(1,n+1)\cdot B & B & & \\ \vdots & \vdots & & \\ \Psi(1,(T-1)\cdot n)\cdot B & \Psi(n+1,(T-1)\cdot n)\cdot B & \ddots & 0 \\ \Psi(1,(T-1)\cdot n+1)\cdot B & \Psi(n+1,(T-1)\cdot n+1)\cdot B & & B \\ \vdots & \vdots & & \vdots \\ \Psi(1,T\cdot n)\cdot B & \Psi(n+1,T\cdot n)\cdot B & \dots & \Psi((T-1)\cdot n+1,T\cdot n)\cdot B \end{bmatrix} \tag{6.30}$$

In Eqn. 6.30, the matrix B is a linear transformation between six impulsive firings along the orbit and the resulting orbital element differences ($\Delta\mathbf{e}_{\mathbf{i}} = B \cdot \Delta V_i$). The matrix B is

$$B = \begin{bmatrix} 0 & 0 & 0 & 0 & \frac{2a^2p}{hr_p} & \frac{2a^2p}{hr_a} \\ 0 & \frac{-r_{90}\cos i}{h\sin i} & 0 & 0 & 0 & 0 \\ \frac{r_0}{h} & 0 & 0 & 0 & 0 & 0 \\ 0 & \frac{r_{90}q_2\cos i}{h\sin i} & \frac{p\sin\theta_p}{h} & \frac{p\sin\theta_a}{h} & \frac{(p+r_p)\cos\theta_p+r_pq_1}{h} & \frac{(p+r_a)\cos\theta_a+r_aq_1}{h} \\ 0 & -\frac{r_{90}q_1\cos i}{h\sin i} & -\frac{p\cos\theta_p}{h} & -\frac{p\cos\theta_a}{h} & \frac{(p+r_p)\sin\theta_p+r_pq_2}{h} & \frac{(p+r_a)\sin\theta_a+r_aq_2}{h} \\ 0 & \frac{r_{90}}{h\sin i} & 0 & 0 & 0 & 0 \end{bmatrix} \tag{6.31}$$

and impulsive firings are modeled as occurring at perigee, apogee, $\theta = 0$ and $\theta = 90°$ where the vectors are

$$\Delta\mathbf{e}_{\mathbf{i}} = \begin{bmatrix} \Delta a & \Delta\theta & \Delta i & \Delta q_1 & \Delta q_2 & \Delta\Omega \end{bmatrix}^T \tag{6.32}$$

$$\Delta V_i(j) = \begin{bmatrix} \Delta v_{h_{0^o}} & \Delta v_{h_{90^o}} & \Delta v_{r_p} & \Delta v_{r_a} & \Delta v_{\theta_p} & \Delta v_{\theta_a} \end{bmatrix}^T \tag{6.33}$$

The p, a, 0 and 90 subscripts for r and θ correspond to the radius and argument of latitude values at perigee, apogee, $\theta = 0$ and $\theta = 0$, respectfully. For example, r_0 corresponds to the radius of the formation center orbit when $\theta = 0$. In this formulation of the B matrix, $\Delta\theta$ and $\Delta\Omega$ are coupled. However, control over $\delta\theta$ can also be achieved with small changes in δa.

6.3.3 Standard Control Algorithm

The outer-loop algorithm solves the optimization problem

$$
\begin{aligned}
J \;&=\; \min_{\Delta\mathbf{U_i}} \; ||\Delta\mathbf{U_1}||_1 + ||\Delta\mathbf{U_2}||_1 + ||\Delta\mathbf{U_3}||_1 + ||\Delta\mathbf{U_4}||_1 \qquad (6.34)\\
\text{s.t.} \;\; & \delta\mathbf{E_i} = H \cdot \delta\mathbf{e_i}(0) + G \cdot \Delta\mathbf{U_i}\\
& |x_i(t,\theta)| \leq d_{max}\\
& |y_i(t,\theta)| \leq d_{max}\\
& |z_i(t,\theta)| \leq d_{max}\\
& V_{4\star}(\delta\mathbf{e_1}, \delta\mathbf{e_2}, \delta\mathbf{e_3}, \delta\mathbf{e_4}) \geq V_{4\star}^{min}\\
& i = 1,2,3,4 \text{ (satellite)}\\
& t = 1,\ldots,T\cdot n \text{ (orbit)}\\
& \theta = [0, \pi/8, \pi/4, \ldots, 15\pi/8]
\end{aligned}
$$

to calculate the desired orbital element differences of the microsatellites in the cluster after one orbit. The optimization problem minimizes the estimated one-norm ΔV such that all the microsatellites stay within the cubic baseline constraint (defined in Chapter 4) and the cluster maintains a minimum average tetrahedral volume over the planning horizon. Both maximum baseline and average minimum volume constraints are maintained by considering the relative position of the satellites in the cluster over 16 evenly spaced points about each orbit.

The constraints on the formation flying problem in this control approach is fundamentally different than several of the previous MPC approaches demonstrated by Tillerson and Breger. Breger, for example, has paid particular attention to the MMS mission where forming tetrahedron shapes are also a mission necessity. According to Ref. [25] the geometric shape of the tetrahedron is important for a formation of satellites to obtain scientific data—

particular emphasis is put on the *regularity* of the tetrahedron. Breger has approached the formation control problem by requiring that the formation achieve a regular tetrahedron once per orbit within a prescribed error [5, 8]. The scale, position and orientation of the tetrahedron are left as degrees of freedom that can be manipulated to obtain the minimum fuel optimal maneuver to achieve a regular tetrahedron once per orbit. While this control approach may be attractive for the MMS mission, it is not suitable for the mission considered in this research. Requiring that the cluster achieve a regular tetrahedron once every orbit would not coincide with mission criteria. Good target tracking capability would not be guaranteed over the remainder of orbit. Good tracking geometry must be maintained throughout the entire orbit since the target time of launch and trajectory are unknown. In addition, satellite separations would not be taken into account by requiring a regular tetrahedron once every orbit. A satellite could potentially be so far away that it is incapable of communicating target line-of-sight measurements with the rest of the cluster and the satellite would not contribute to the cluster's mission performance.

Maximum cluster baseline and minimum average tetrahedral volume are used as constraints to model realistic mission criteria for a target tracking mission. In many space missions, minimum criteria are usually identified as control or formation requirements. Since fuel is a limited resource, this control approach attempts explicitly pose those criteria as constraints in the control problem. Thus, fuel is only consumed to maintain geometry above specified mission criteria; not to maintain a cluster geometry that exceeds mission criteria.

6.3.4 Control Algorithm Augmented with J_2-Induced Drift Penalty (Multi-objective MPC)

A standard practice in infinite horizon control schemes is to penalize or constrain a terminal state of the system to ensure plant stability [12]. With this in mind, another approach to the control problem is considered that penalizes terminal J_2-induced relative drift as well as the expected ΔV. In this formulation, J_2-induced relative out-of-plane and in-plane drifts for each satellite are penalized using the linearized formulation defined in Eqn. 4.6 and is denoted as Λ_i. The objective function in the multi-objective MPC outer-loop algorithm is

$$J = \min_{\Delta \mathbf{U_i}} R_{\Delta V} \cdot \Big(||\Delta \mathbf{U_1}||_1 + ||\Delta \mathbf{U_2}||_1 + ||\Delta \mathbf{U_3}||_1 + ||\Delta \mathbf{U_4}||_1 \Big) + R_{\Lambda} \cdot \Big(||\Lambda_1||_1 + ||\Lambda_2||_1 + ||\Lambda_3||_1 + ||\Lambda_4||_1 \Big) \quad (6.35)$$

6.3.5 Variable Formation Center

Refs. [36] and [7] reduced fuel consumption for each of the satellites in a cluster by choosing the formation center to minimize the mean squared error of the satellites at a prescribed point along the orbit. In the study, relative geometry between the satellites was the important cluster criteria, not the satellites' relative positions from the formation center about which their motion was modeled. Thus, fuel consumption was reduced by accounting for unmodeled forces such as atmospheric drag that affected the entire cluster. For this study, a variable formation center is proposed that updates the formation center to minimize the maximum distance of all the satellites from the formation center. Control actions in the algorithm advocated in this chapter only occur when one of the two cluster constraints are violated (i.e., maximum baseline or minimum average volume). Thus, intelligently choosing a formation center that minimizes the maximum distance of the satellites from the formation center should reduce cluster-wide fuel consumption.

A linear, convex formulation for determining the variable formation center is considered in this chapter. The current formation center ($\mathbf{e_{fc}}$) is propagated forward using the nonlinear dynamic model for orbital motion and the relative motion of the satellites in the cluster are calculated using the linearized state transition matrices. The six relative orbital elements of the variable formation center ($\delta \mathbf{e_{fc^\star}}$) are then chosen to satisfy the optimization problem

$$\begin{aligned} J &= \min_{\delta \mathbf{e_{fc^\star}}, \mathbf{x^\star}, \mathbf{y^\star}, \mathbf{z^\star}} c_x x^\star + c_y y^\star + c_z z^\star \qquad (6.36) \\ s.t. \ & |x_i(t) - x_{fc^\star}(t)| \leq x^\star \\ & |y_i(t) - y_{fc^\star}(t)| \leq y^\star \\ & |z_i(t) - z_{fc^\star}(t)| \leq z^\star \\ & i \in (1, \ldots, N) \text{ (satellite)} \\ & t \in (1, \ldots, T) \text{ (time)} \end{aligned}$$

Table 6.3: Initial formation center parameters.

Orbital Element	value
a	7653.77 km
e	0.1
i	45°
Ω	0°
ω	0°
M	0°

The outer-loop optimization problem (Eqn. 6.34) uses the updated variable formation center ($\mathbf{e_{fc^*}} = \mathbf{e_{fc}} + \delta\mathbf{e_{fc^*}}$) to model satellite relative motion and constrain the maximum baseline. The relative orbital elements of the satellites in the cluster are re-initialized to the updated formation center by: $\delta\mathbf{e_i}^\star = \delta\mathbf{e_i} - \delta\mathbf{e_{fc^*}}$.

The cost function coefficients (c_x, c_y, and c_z) are chosen such that $c_z > c_x > c_y$ since out-of-plane control actuation requires more fuel than radial control and in-track control [30]. Thus, out-of-plane maximum satellite distance is penalized the most and in-track the least. This formulation ensures that in-track maximum distances are not traded for out-of-plane ones and cause increased fuel consumption. This study uses $c_z = 3$, $c_x = 2$ and $c_y = 1$ and acceptable behavior is observed.

6.3.6 Planning Horizon and Reconfiguration Orbits

Errors in linearized models tend to grow quickly when the states of the system are quickly changing. For this reason, an important benefit of propagating the relative orbital elements in the model is that most of the states are slowly changing as opposed to modeling relative satellite motion in Cartesian space. Unfortunately, while δa, δi, δq_1, δq_2 and $\delta\Omega$ are slow changing states, the relative argument of latitude ($\delta\theta$) is not. $\delta\theta$ will grow unbounded due to differences in orbital energy. Even with bounded relative motion, though, $\delta\theta$ will oscillate with the same period as the formation center's orbit. Accumulated error in $\delta\theta$ can cause in-plane relative motion linear prediction errors of several kilometers over long planning horizons (several orbits) for the cluster baseline sizes considered in this study. Thus, planning horizon has a big impact on controller performance. A planning horizon that is too long can cause control actions to unnecessarily occur.

In order to choose planning horizon and reconfiguration orbits for the MPC algorithm,

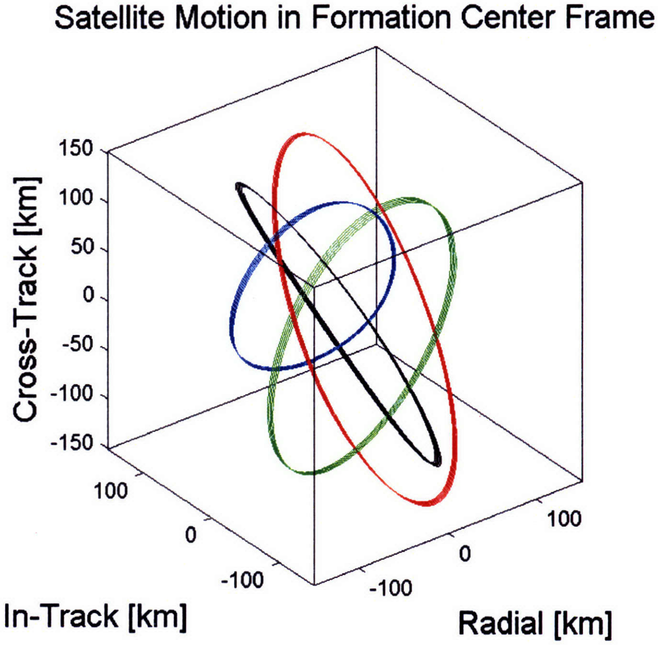

Figure 6-3: Initial configuration for cluster #1 plotted about the formation center.

Table 6.4: Relative orbital elements for microsatellites in cluster #1. δa is normalized by the radius of the Earth (r_{eq}).

$\delta\mathbf{e}$	Sat 1	Sat 2	Sat 3	Sat 3
δa	0	0	0	0
$\delta\theta$	-0.0219763	-0.0004971	-0.0026236	0.0038658
δi	0.0132516	0.0085032	-0.0080945	-0.0119598
δq_1	0.0064206	-0.0054917	-0.0044107	0.0037031
δq_2	0.0019176	-0.0043700	0.0723877	-0.0058130
$\delta\Omega$	0.0161712	0.0208307	-0.0213800	-0.0175778

the controller is implemented for a cluster that exhibits high relative drift rates in a simulation with a J_2 gravity model about the formation center orbit in Table 6.3. Thus, all state errors are associated with linearization errors in the controller model. The cluster (with initial states in Table 6.4) was designed with a 250 km baseline to maximize average tetrahedral volume subject to $\delta a_i = 0$ (see Fig. 6-3).

The cluster is simulated over 150 orbits with different planning horizon and reconfiguration orbits values as shown in Table 6.5. The average total ΔV consumption for each planning horizon reconfiguration orbit value are plotted in Fig. 6-4. Results shown in Fig. 6-4(a) demonstrate that longer planning horizons cause an increase in ΔV consumption. This observation is likely due to the increased modeling error associated with longer planning

Table 6.5: Test matrix for tuning the planning horizon and reconfiguration orbits in the MPC algorithm.

		Planning Horizon (Orbits)							
		5	10	15	20	30	40	45	60
Reconfiguration Orbits	1	x	x	x					
	2		x		x	x			
	3			x		x		x	
	4				x		x		x

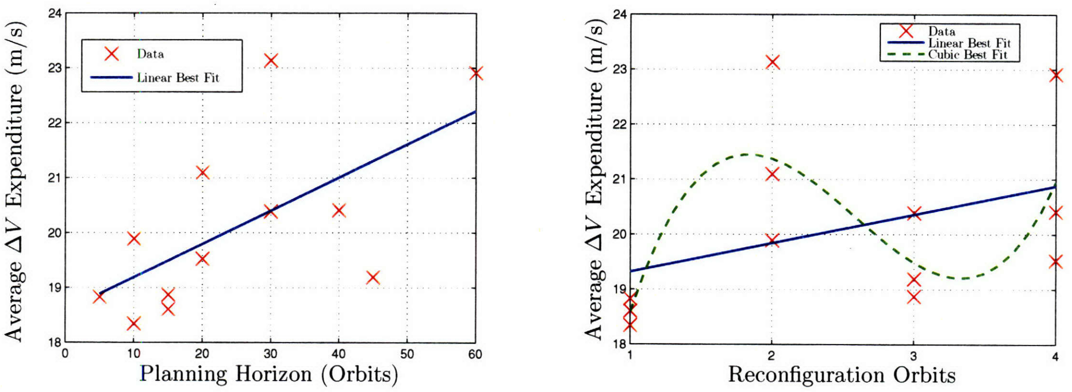

(a)

(b)

Figure 6-4: Average ΔV consumption for cluster #1 with different planning horizons and reconfiguration orbits in the nominal outer-loop MPC algorithm. General trend lines are also plotted.

horizons. Results in Fig. 6-4(b) show two general trends: (1) a linear increase in ΔV associated with increased reconfiguration orbits and (2) a local minimum at three reconfiguration orbits in the outer-loop planner. The linear trend is driven by planning horizon and the local minimum is due to more control authority in the control algorithm. There is a minimum in controller performance with three configuration orbits in the outer-loop planner for a fixed planning horizon.

Thus, a planning horizon of 15 orbits is chosen with three reconfiguration orbits in the MPC algorithm for this research. The cluster will be allowed to reconfigure for one orbit then spends four orbits observing.

6.4 Results

A 490 orbit, high-fidelity simulation with the Earth's J_2 through J_{10} zonal harmonics is used to evaluate controller performance. However, no sensing noise is included. Two clusters

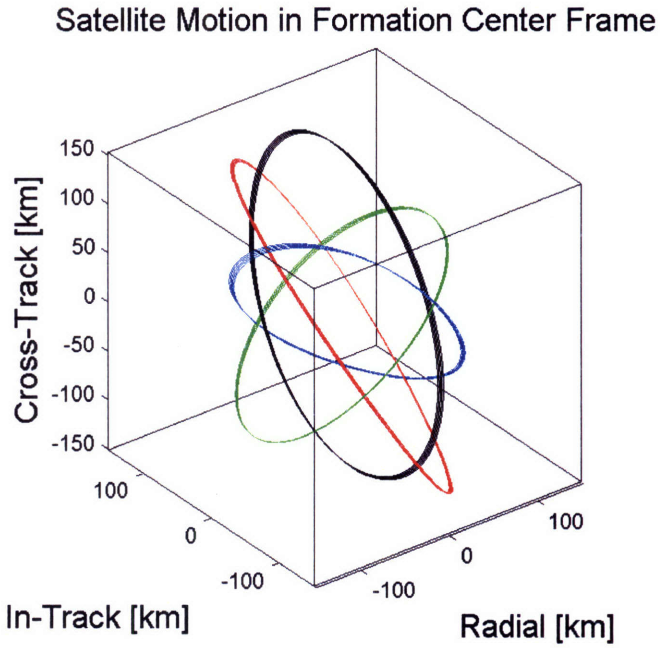

Figure 6-5: Initial relative motion for cluster #2 about the formation center.

Table 6.6: Relative orbital elements for microsatellites in cluster #2. δa is normalized by the radius of the Earth (r_{eq})

$\delta\mathbf{e}$	Sat 1	Sat 2	Sat 3	Sat 4
δa	0.0000273	-0.0000298	-0.0000056	-0.0000215
$\delta\theta$	-0.0006589	0.0007161	0.0005621	0.0006958
δi	-0.0005368	0.0006990	-0.0000495	0.0000849
δq_1	0.0006657	-0.0009601	-0.0002987	-0.0006207
δq_2	0.0003126	-0.0000908	-0.0002612	-0.0007132
$\delta\Omega$	-0.0004362	-0.0009482	0.0004339	-0.0001978

about the formation center in Table 6.3 are used to test the controller performance. Cluster #1 is the one used to tune the MPC algorithm and the satellites in the cluster exhibit high relative drift rates (see Table 6.4 and Fig. 6-3). Cluster #2 was designed to maximize average tetrahedral volume with a high penalty on J_2-induced relative drift (see Table 6.6 and Fig. 6-5). Expected fuel rates for each of these cluster using the linearized predictions to reestablish mean relative orbital elements due to J_2-induced relative drift are presented in Table 6.7.

The maximum cluster baseline and minimum average tetrahedral volume constraints in the control algorithm are both relaxed by 5% from initial cluster design values for all simulation runs (i.e., both clusters were designed with a 250 km baseline but the baseline

Table 6.7: Estimated ΔV for satellites in the clusters required to reestablish mean relative orbital elements due to J_2-induced relative drift (mm/s/orbit).

Cluster	Sat 1	Sat 2	Sat 3	Sat 4	Average
Cluster #1	347	223	212	314	274
Cluster #2	78	41	57	70	54

Table 6.8: Fuel rate for each satellite with the nominal MPC algorithm in the high-fidelity simulation (mm/s/orbit).

Cluster	Sat 1	Sat 2	Sat 3	Sat 4	Average
Cluster #1	150	201	242	352	236
Cluster #2	58	3.3	29	1.6	23

constraint is increased to 262.5 km in the control algorithm). The formation center is numerically integrated in the controller model with J_2 harmonics to define relative satellite motion and cluster constraints.

In the outer-loop planner, the first two propagated orbits did not have to satisfy maximum baseline and minimum volume constraints so that a feasible solution could always be found. For implementation, a linear program was used to solve Eqn. 6.34 without the volume constraints. This linear programming problem was solved in a few seconds on a 3.60 GHz computer with 1 GB of RAM. A nonlinear program then used the linear solution to solve Eqn. 6.34 with the volume constraint. If the volume constraint was satisfied, then the linear solution was the global solution. If the volume constraint was not satisfied, then the nonlinear program generally returned a feasible solution in under 60 seconds (much smaller than a single orbit).

6.4.1 Standard Control Algorithm

This section presents results for the standard outer-loop control algorithm. Total fuel consumption results for the two clusters are presented in Fig. 6-6 and Table 6.8 using the nominal optimization formulation (Eqn. 6.34). In both cases, satellites in the cluster don't require ΔV until a constraint becomes active.

Both clusters consume less average ΔV than is expected from a control algorithm that simply reestablished mean relative orbital elements. Cluster #1 used an average of 14% less ΔV and Cluster #2 used 57% less. Interestingly, though, the third and fourth satellites

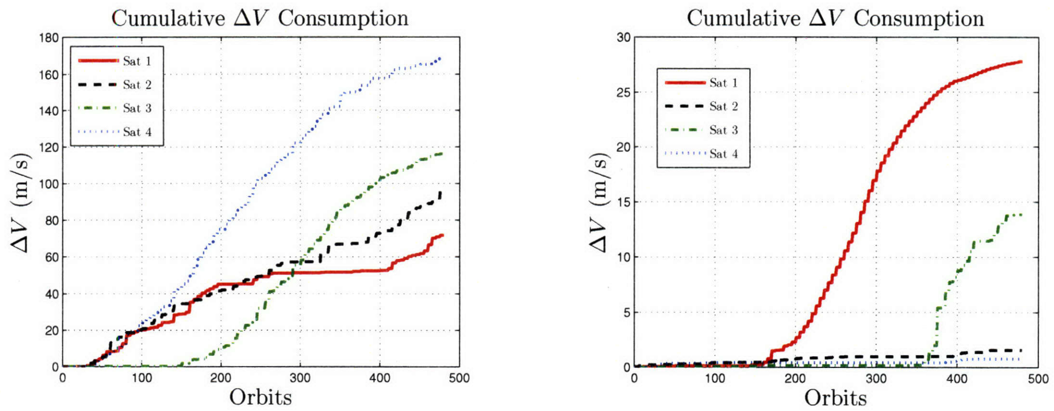

(a) High Relative Drift Rates (Cluster #1). (b) Low Relative Drift Rates (Cluster #2).

Figure 6-6: Fuel consumption for each cluster with the nominal MPC algorithm. Note the difference in the magnitudes of the plots. The rapid increase in fuel consumption for the first satellite in (b) occurs because the out-of-plane baseline constraint became active due to J_2-induced relative drift for $\delta\Omega$.

in Cluster #1 required more ΔV than predicted by simply reestablishing mean relative orbital elements every orbit. This observation may be due to the fact that the control algorithm penalized the total cluster wide ΔV consumption. Thus, these satellites using more ΔV resulted in less total ΔV consumption to maintain the maximum cluster baseline and minimum volume constraints. One way to prevent this phenomenon would be to place a higher penalty on ΔV in the control algorithm for satellites that have already used more ΔV [37]. This technique keeps the ΔV consumption of the satellites about equal so that one satellite does not run out of fuel before the rest of the satellites in the cluster.

Another, perhaps more important, observation from the data of these two clusters is the relative ΔV consumption between the clusters. Initializing a cluster with low J_2-induced relative drift greatly reduces the ΔV consumption of the cluster. Cluster #2 used 90% less ΔV than cluster #1 even though the satellites in both clusters were allowed to drift relative to each other. High drift rates in cluster #1 caused the constraints to be more active and require more fuel to maintain those constraints.

6.4.2 Control Algorithm Augmented with J_2-Induced Drift Penalty (Multi-Objective MPC)

Fuel consumption results for cluster #1 using the multi-objective MPC algorithm with $R_\Lambda/R_{\Delta V} = 200$ are presented in Fig. 6-7(b) against results with the nominal MPC algo-

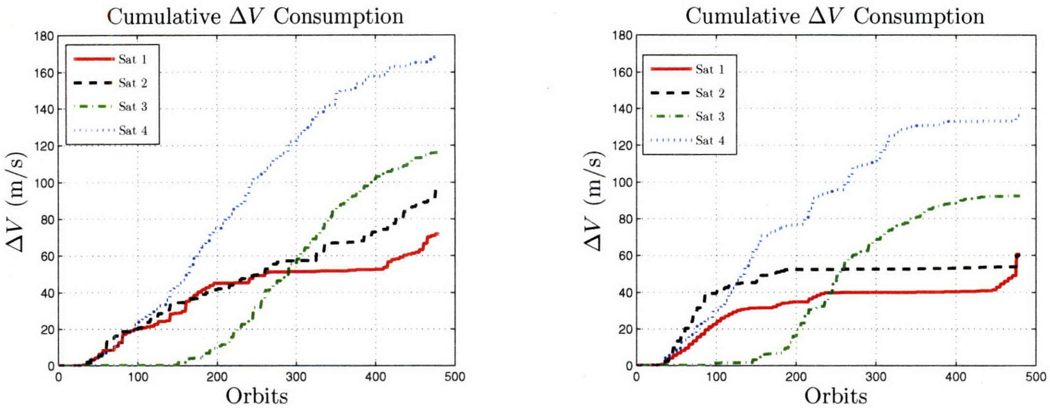

(a) ΔV for cluster #1 with the nominal MPC algorithm.

(b) ΔV for cluster #1 with the multi-objective MPC algorithm.

Figure 6-7: ΔV for cluster #1 with both the nominal and multi-objective MPC algorithms.

rithm. The multi-objective MPC algorithm uses 23% less fuel than the nominal algorithm. Reduced fuel is not observed with the multi-objective MPC algorithm until 260 orbits into the simulation. The multi-objective MPC algorithm initially causes the cluster to consume more ΔV because the satellites in the cluster are using ΔV to maneuver towards J_2-invariant orbits in addition to maintaining the controller constraints.

Fig. 6-8 presents the relative drift rates for the satellites in the cluster for each of the control approaches throughout the simulation. The absolute relative drift rates for the cluster with the multi-objective MPC algorithm are clearly being reduced. An interesting observation from Fig. 6-8(a) is the long term oscillation in expected ΔV to reestablish $\delta\Omega$. Control actuation did not cause this oscillation; rather, higher order gravitational terms caused it. According to Roy [26], the J_3 harmonic causes long term oscillations in i and e for a satellite

$$\Delta_3 i = \frac{1}{2}\frac{J_3}{J_2}\frac{r_{eq}}{a}\frac{e}{1-e^2}\cos i \sin \omega \tag{6.37}$$

$$\Delta_3 e = -\frac{1}{2}\frac{J_3}{J_2}\frac{r_{eq}}{a}\sin i \sin \omega \tag{6.38}$$

These, and higher order, oscillations are not accounted for in the linearized J_2-induced relative drift cost. In addition, only a linear mapping between osculating and mean orbital elements was used to convert orbital elements into mean orbital elements for modeling relative satellite motion in the control algorithm [33]. The transformation only takes into account the J_2 harmonic; higher order terms are unaccounted. Thus, using a linearized

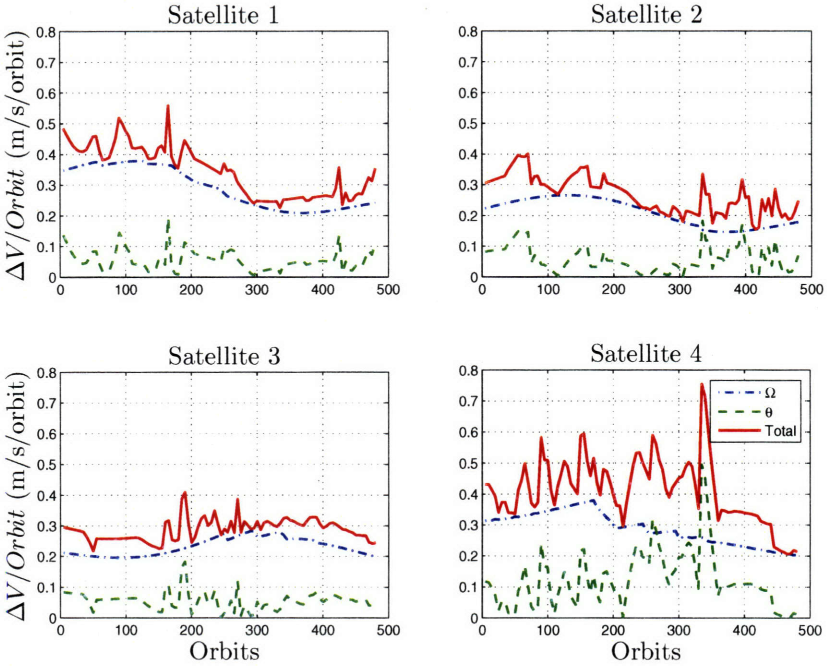

(a) Linearized J_2-induced relative drift (Λ_i) of the satellites in the cluster for the nominal MPC algorithm

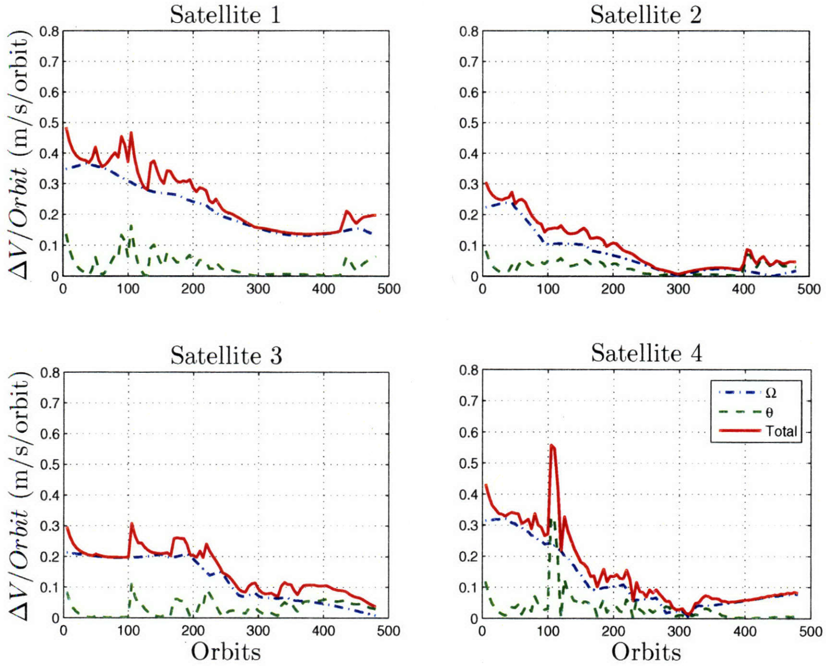

(b) Linearized J_2-induced relative drift (Λ_i) of the satellites in the cluster for the multi-objective MPC algorithm that penalizes both ΔV and J_2-induced relative drift

Figure 6-8: Relative drift for the two MPC approaches. The relative drift is reported as the predicted ΔV required to reestablish the relative orbital elements of the satellites every orbit due to J_2-induced relative satellite drift.

Table 6.9: Comparison of ΔV results for cluster #2 with a fixed and a variable formation center (mm/s/orbit).

Control Algorithm	Sat 1	Sat 2	Sat 3	Sat 4	Average
Fixed FC	57.86	3.32	28.87	1.64	22.92
Variable FC	0.79	1.19	1.10	0.43	0.88

cost for J_2-induced relative drift is limited by higher order harmonics. The behavior of cluster #2 with the multi-objective MPC algorithm supports this notion. Reduced ΔV was not observed for cluster #2. For example, a relative cost ($R_\Lambda/R_{\Delta V} = 200$) that was successful for cluster #1 resulted in approximately 9% more ΔV consumption for cluster #2. The relative drifts rates are already so low that rates are near the minimum threshold for using a linearized J_2-invariant criteria without taking into account higher order gravitational harmonics. Long term variations in inclination due to J_3 result in variations of 1.5 mm/s/orbit and 0.7 mm/s/orbit for estimated ΔV required to maintain relative Ω and θ_M, respectfully at this formation center. Similarly, long term variations in eccentricity due to J_3 result in approximated variations of 6.0 mm/s/orbit and 0.7 mm/s/orbit.

6.4.3 Variable Formation Center

The results from the outer-loop control algorithm with the variable formation center are presented in this section. A linear program consistently solved Eqn. 6.36 for the variable formation center in under one second.

Fig. 6-9(b) presents ΔV consumption results for cluster #2 with a variable formation center and are compared directly to results using the nominal MPC algorithm (Fig. 6-9(a)). The consumption is reduced by 96% when the variable formation center is implemented (see Table 6.9) and the maximum distance between the variable formation center and the nominal formation center is no more than 184.9 km over the 490 orbit simulation (see Fig. 6-10). The variation between the two formation centers is less than the baseline size of the cluster (250 km). This is important because the formation center is designed in the context of the entire constellations to maintain 24 hour coverage of the occupancy corridor. Moving the formation center significantly could open up substantial gaps in tracking coverage.

The variation in orbital elements of the two formation centers are plotted in Fig. 6-11. Variations in out-of-plane parameters (i and Ω) seem to coincide with long-term, cluster

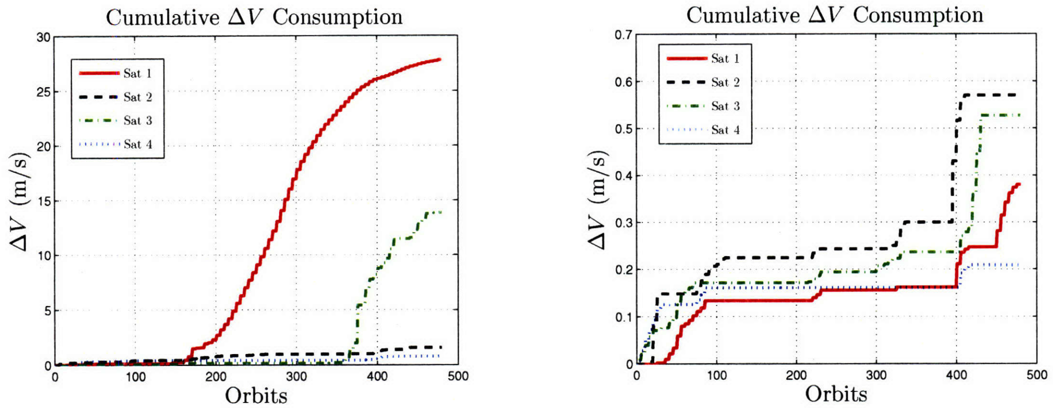

(a) Fixed formation center.

(b) Variable formation center.

Figure 6-9: Fuel consumption for cluster #2 with a fixed and variable formation center. Note the difference in the magnitudes of the plots.

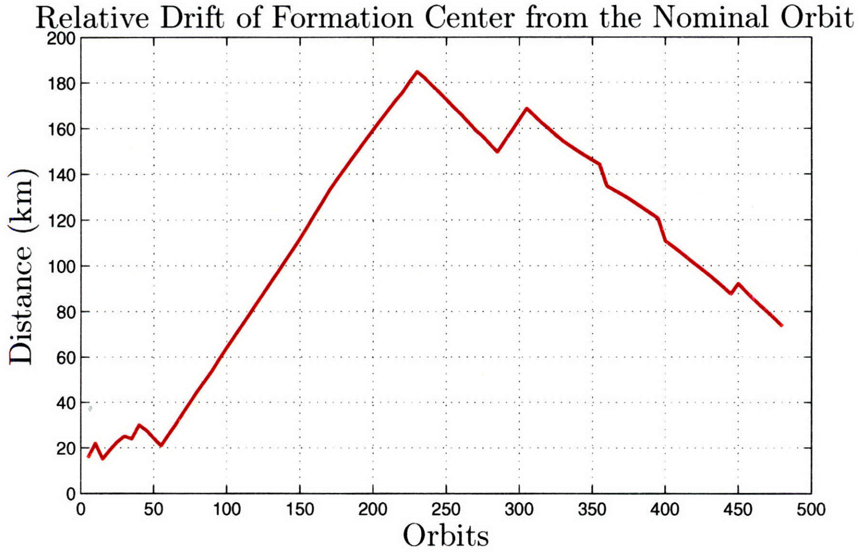

Figure 6-10: Distance between variable and fixed formation centers throughout the simulation.

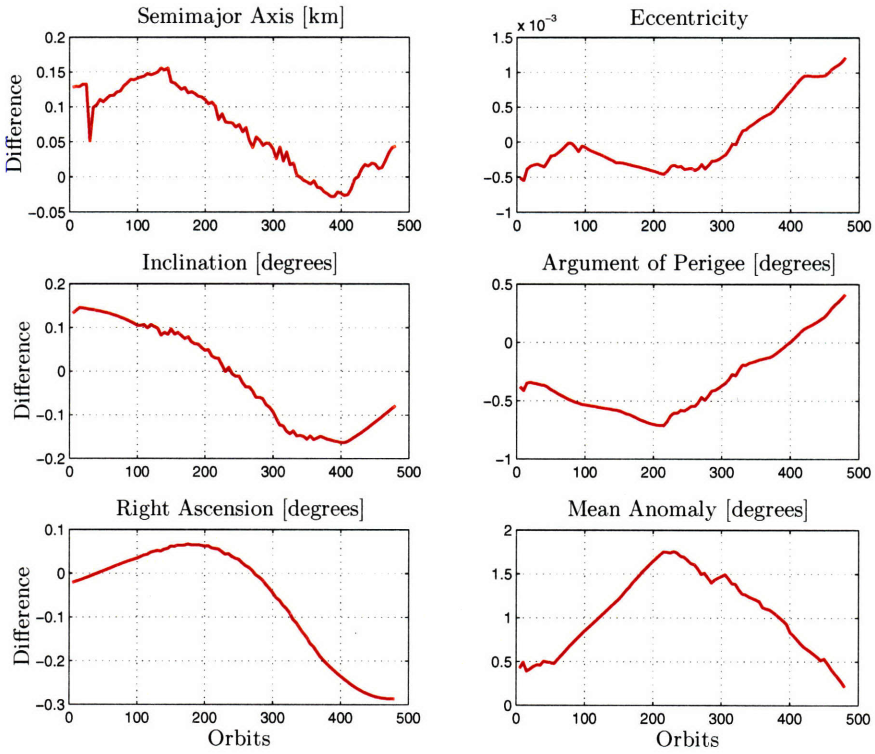

Figure 6-11: Difference between orbital elements of the variable formation center and the fixed formation center.

wide oscillations associated with J_3. The variations in ω and M are likely due to slight variations in cluster wide orbital energy. These results suggest that the variable formation center is a simple way to accommodate for unmodeled dynamics in the control algorithm without using a more complex dynamic model. Atmospheric drag is a particularly important consideration for clusters flying in LEO. The variable formation center would likely exhibit even better results in comparison if drag was included in the simulation.

6.5 Chapter Summary

An MPC algorithm for cluster maintenance was developed in this chapter that allowed relative satellite drift to occur as long as simple, mission driven constraints were met (i.e., maximum baseline and minimum average tetrahedral volume). With mission success in mind, reconfiguration maneuvers only occurred once every five orbits so that the likelihood of the microsatellites firing their thrusters during a target launch are minimal. Important technical considerations in this chapter were a multi-objective MPC algorithm and a variable formation center.

Observations from this chapter confirm that designing a cluster with low allowable J_2-induced relative drift rates greatly reduces the ΔV consumption of the satellites in the cluster even when the satellites are allowed to drift. In fact, other clusters designed with very high penalties on J_2-induced relative drift (not presented in this chapter) did not require any fuel consumption over the 490 orbit simulation when the nominal MPC architecture was couple with the variable formation center. The variable formation center presented in this chapter added a robustness to the control algorithm that minimized control actuation due to unmodeled dynamics and cluster wide motion that did not interfere with mission requirements. The simulation results for cluster #2 presented in this chapter showed 96% less ΔV consumption with a variable formation center.

Simulation results from this chapter are comparable to previous simulations using model predictive controllers by Tillerson and Breger, even though the missions considered are very different. In Ref. [5], Breger et al. use a model predictive controller for an MMS-like mission that maintains a regular tetrahedron once every orbit in a highly elliptical orbit. In the seven day simulation, results indicated that the satellites used 11.5 mm/s per day ($\approx$ 1 orbit). These fuel consumption rates are lower than those for cluster #2 using the nominal MPC approach which required 22.92 mm/s per orbit (where 13 orbits $\approx$ 1 day). However, the rates are higher than cluster #2 with a variable formation center (0.88 mm/s/orbit). Directly comparing these rates is not trivial since the simulations are for two very different missions in two very different orbits. However, the general rates at which ΔV is consumed provide some additional and useful insights. In Ref. [5], the satellites consume ΔV at a steady rate (per orbit) throughout the simulation suggesting the controller is constantly compensating for some disturbance every orbit. In this chapter, however, the ΔV consumption rates are not uniform (see Fig. 6-9(b), for example). In Fig. 6-9(b), the cluster does not require ΔV for as many as 100 consecutive orbits in the simulation. This suggests that the model predictive controller in this study allows the cluster to naturally evolve. It does not uniformly consume fuel to compensate for natural disturbances.

In Ref. [39], Tillerson et al. present simulation results for a model predictive controller applied to formation initialization and formation-keeping problems. Results for the formation-keeping problem (similar to a TechSat-21 mission) can be most directly compared to results in this research. The simulation lasted two days (or approximately 32 orbits) and is for a LEO mission. Tillerson reports for a simulation with no measurement noise that the controller requires approximately 12 mm/s/orbit. A simulation with noise and a robust controller formulation required 32 mm/s/orbit for each satellite. These values are comparable to some of the results presented in this chapter. However, the cluster size in the simulation is much smaller than that considered in this research. The satellites in Ref. [39] are required to maintain a passive aperture formation that projects a 400 m by 200 m ellipse on the orbital plane and oscillates with an amplitude of 100 m in the cross-track direction. This is much smaller than the 250 km baseline clusters in this study. In addition, the ΔV consumption rates are also uniform throughout the simulation suggesting that the model predictive controller is also constantly compensating for disturbances on relative satellite motion.

Conclusions from this chapter emphasize the value of designing cluster control algorithms that are robust to unmodeled dynamics (if missions requirements allow for such robustness). Results also indicate the importance of choosing controller constraints that accurately reflect mission requirements. Further improvements in this MPC algorithm could likely be achieved by exploring better ways to constrain intersatellite communication requirements. The linearized cubic baseline constraint in this research, for example, may have unnecessarily caused ΔV consumption even though realistic communication constraints were not being violated.

Chapter 7

Final Simulation Results

Chapters 3 and 4 of this thesis presented an optimal measurement approach to designing a constellation and a cluster for tracking a target in the *occupancy corridor.* Clusters were synthesized to provided the minimum target tracking error given constraints on cluster baseline size and number of satellites in the cluster. The cluster design approach in Chapter 5 diverged from the optimal measurement approach. A cluster design heuristic was derived that provided good cluster geometry for tracking a target in any direction. Finally, Chapter 6 presented a control algorithm that minimized cluster-wide fuel consumption by allowing the cluster drift and naturally evolve with time. This chapter describes a high-fidelity, 30 day simulation that is used to compare the optimal measurement methods approach to cluster design versus the approach that maximizes average *tetrahedral volume* and allows the cluster to evolve with time. Over 400 cluster/target engagements are simulated and this chapter compares tracking results for the different approaches.

This chapter's outline is as follows: Sec. 7.1 describes the target trajectories used in the simulation to analyze cluster tracking performance. In addition, three different clusters are described which are all compared to a single satellite at the formation center as a baseline. Sec. 7.2.1 compares the clusters' tracking performance over the entire simulation. Between the three clusters over 1200 tracking engagements were simulated. Thus, Sec. 7.2.2 discusses some general observations for a cluster's tracking performance.

Table 7.1: Dispersion values for target trajectories from the nominal path in the simulation.

Orbital Parameter	Random Dispersion Values
a	±50 km
e	±0.2
i	±10°
Ω	±3°
ω	±10°
$f_{initial}$	±10°

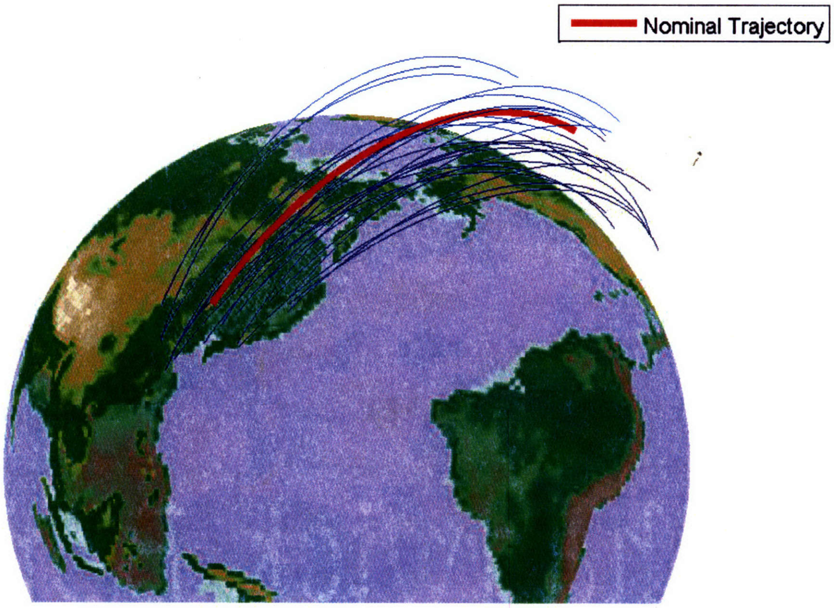

Figure 7-1: Twenty-one of the 429 target trajectories are plotted in the ECEF coordinate frame. The nominal occupancy corridor is in bold.

7.1 Simulation Description

This section describes a high-fidelity simulation used to compare three different clusters. A total of 429 cluster/target engagements that each last 1700 seconds are simulated and recorded for each of the clusters over a 30 day simulation. In addition, the tracking performance of a single satellite located at the *formation center* is used as a baseline for comparison. The nominal target occupancy corridor is the same as that described in Chapter 3. However, each of the target trajectories are randomly perturbed from nominal values as defined in Table 7.1 (see Fig. 7-1 for a representative dispersion of the target trajectories modeled in the simulation).

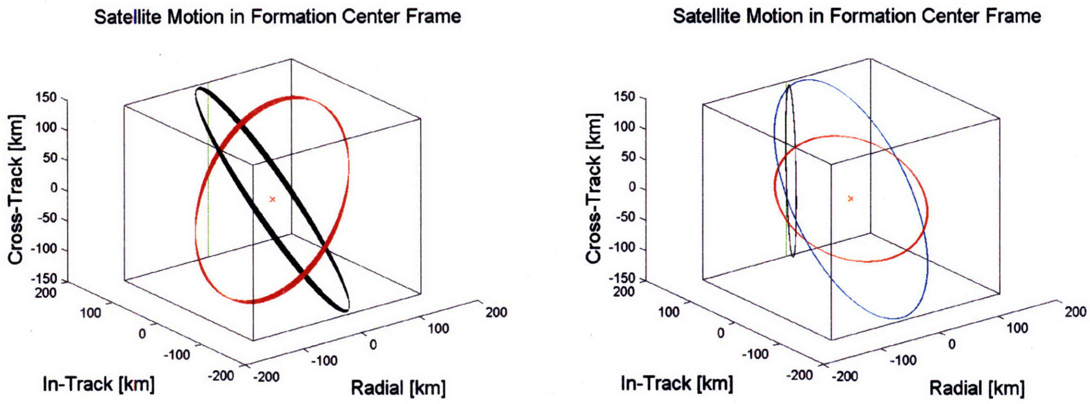

(a) First cluster.

(b) Second cluster.

Figure 7-2: Initial relative motion of the first two clusters about the formation center over 15 orbits.

Each cluster in the simulation has four satellites, a 250 km baseline and all are designed about the formation center defined in Chapter 4. The first cluster is designed to minimize the average model-based value for the target position estimation error covariance (Eqn. 4.2). The second cluster is designed to minimize the average model-based value for the target position estimation error covariance plus expected J_2-induced relative satellite drift (Eqn. 4.7). Finally, the third cluster is designed to maximize the average tetrahedral volume and is also designed with a high penalty on J_2-induced relative drift (Eqn. 5.20).

The relative motion of the satellites in the first and second clusters are shown in Fig. 7-2. Both of these clusters are assumed to maintain their relative motion throughout the entire simulation by reestablishing their mean relative orbital elements every orbit using the impulsive control scheme described in Sec. 4.2.2. This corresponds to an average ΔV expenditure of 1128 mm/s/orbit for satellites in the first cluster and an average of 1.25 mm/s/orbit for satellites in the second cluster. The third cluster shown in Fig. 7-3, however, is allowed to drift as long as maximum baseline and minimum average tetrahedral volume are maintained. The control algorithm in Chapter 6 is utilized with a variable formation center. The total ΔV consumption for this cluster is reported in Fig. 7-4 and average ΔV required per orbit is presented in Table 7.2. This cluster uses significantly less ΔV per orbit than predicted for either of the other two clusters (an average of 0.086 mm/s/orbit). The maximum distance between the variable formation center for the third cluster and the nominal formation center of the first two clusters is 110 km for the 30 day simulation (see Fig 7-5). This is less than the baseline size of the cluster.

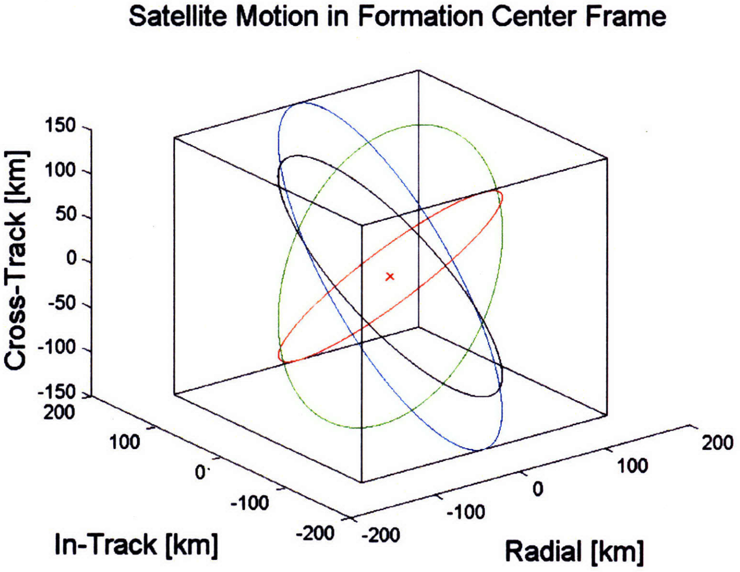

Figure 7-3: Relative motion of satellites in the third cluster, which was initialized to maximize average tetrahedral volume and had a high penalty on J_2-induced relative drift.

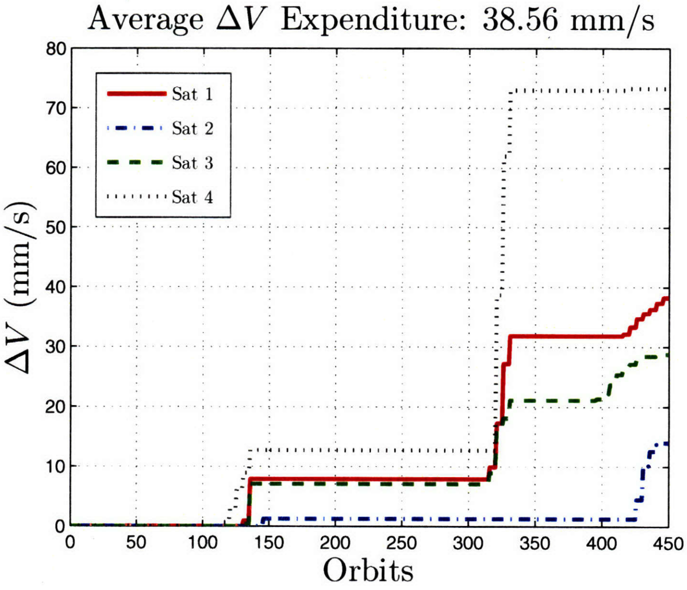

Figure 7-4: The ΔV consumption for the third cluster over the 30 day simulation. The jump in ΔV expenditure around 320 orbits occurs because baseline constraints in the out-of-plane direction were simultaneously violated for satellites one, two and three. The controller re-establishes the satellites over three reconfiguration orbits such that no further constraints are violated until approximately 400 orbits.

Table 7.2: The third cluster's ΔV average consumption rate per orbit using the MPC algorithm and variable formation center described in Chapter 6.

Sat 1	Sat 2	Sat 3	Sat 4	Average
0.085	0.01	0.064	0.163	0.086

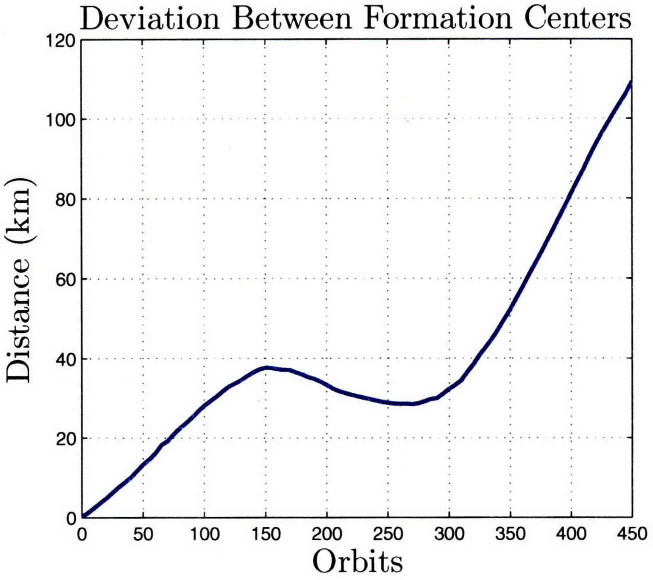

Figure 7-5: Distance between the nominal formation center and the variable formation center used in the maintenance algorithm over the 450 orbit simulation.

7.2 Simulation Results

Simulation target tracking results are presented in this section. Tracking behavior for each of the three clusters and the single satellite are compared in Sec. 7.2.1. In addition, general observation for target tracking performance for a cluster of microsatellites are studied in Sec. 7.2.2.

7.2.1 Cluster Comparison

Average expected estimation errors (as reported from the centralized Kalman filter) for each of the clusters are plotted in Fig 7-6 and true average errors are presented in Fig. 7-7 and the first cluster showed the best tracking performance, exhibiting approximately 20% better tracking accuracy than the other two clusters. However, this increased performance is negligible when compared to the tracking performance of a single satellite. Standard deviation values are presented in Table 7.3. The difference between standard deviation values are also negligible when compared to the values for a single satellite.

Average 50% convergence times for each of the clusters are presented in Table 7.4 and show similar convergence speeds for all the clusters. While the first cluster's convergence speed for actual target position error is approximately 41 seconds faster than the third cluster's, it's convergence time for estimated target position error is 46 seconds slower.

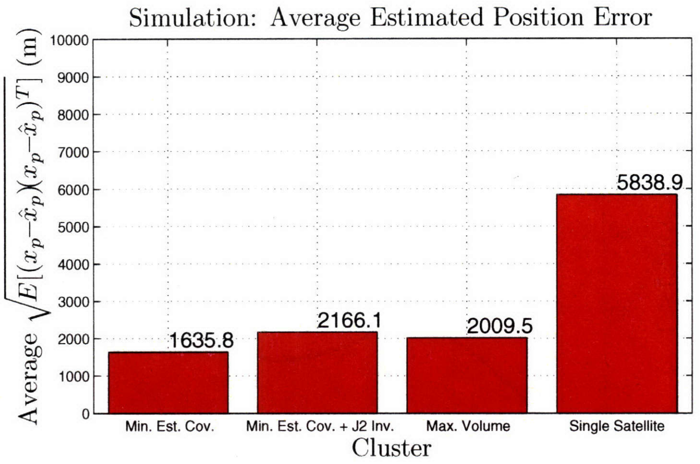

Figure 7-6: Average standard deviation value for the expected target position estimation error as reported from the Kalman filter for each of the clusters.

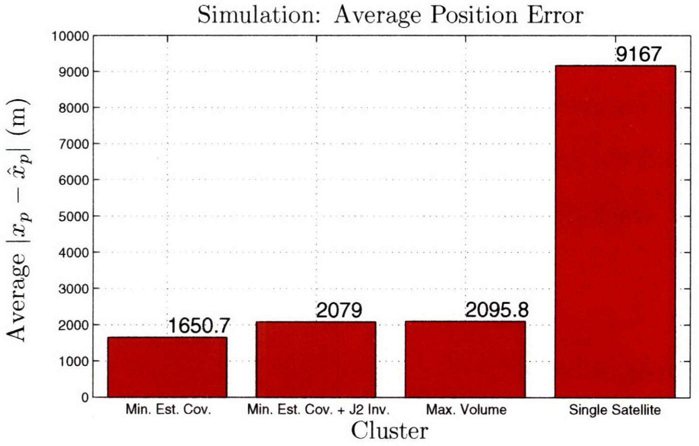

Figure 7-7: Average true target position estimation error for each of the clusters.

Table 7.3: Standard deviations for estimated and true target position error for each cluster over the Monte Carlo simulation.

Cluster	Actual Position Error	Estimated Position Error
Min. Est. Cov.	1511 m	900 m
Min. Est. Cov. + J_2-Inv.	1649 m	965 m
Max. Volume	2013 m	947 m
Single Satellite	47392 m	3406 m

Table 7.4: Average convergence time for all clusters. The convergence time is defined as the time (in seconds) for the position error or estimated position error to converge within 50% of the final value. Smaller convergence times correspond to quicker convergence. The simulation time is 1700 seconds.

Cluster	Actual Position Error Convergence Time (s)		Estimated Position Error Convergence Time (s)	
	mean	σ	mean	σ
Min. Est. Cov.	1191	455	852	388
Min. Est. Cov. + J_2-Inv.	1223	441	783	400
Max. Volume	1233	446	806	385
Single Satellite	1200	422	789	402

The increased tracking performance observed for the first cluster comes at the high price of fuel consumption and design complexity. Recall that Ref. [18] predicted the total available ΔV for a mission of small, light spacecraft to be on the order of 400 m/s. If the satellites in the cluster were to expend fuel at 1128 mm/s/orbit, the cluster's effective lifetime would be less than 400 orbits (or 27 days). The approach to cluster design which maximized the average tetrahedral volume and cluster control which allowed relative satellite drift to occur seems like a reasonable and acceptable approach to cluster design for target tracking missions given these results.

7.2.2 General Observations

Estimated and actual position error results for the 1287 cluster/target engagements simulated in this study are plotted in Fig. 7-8 against target inclination (i_{tgt}), target eccentricity (e_{tgt}), the difference between formation center and target argument of latitudes ($\theta_{fc} - \theta_{tgt}$) and the difference between formation center and target right ascensions ($\Omega_{fc} - \Omega_{tgt}$). The plots show a correlation between e_{tgt} and estimated position error as reported from the Kalman filter—the estimated position error increases as e_{tgt} increases. A strong relationship between ($\theta_{fc}-\theta_{tgt}$) and tracking performance also appears to exist. There is a minimum in tracking error when ($\theta_{fc} - \theta_{tgt}$) $\approx 15°$. This observation suggests that there is a *sweet-spot* at $-15°$ for target tracking performance. Finally, there appear to be slight correlations between i_{tgt} and the magnitude of ($\Omega_{fc} - \Omega_{tgt}$) with tracking performance.

Correlation coefficients and p-values are reported in Table 7.5 for these simulation results and support the observations from the plots. There are indeed strong correlations between

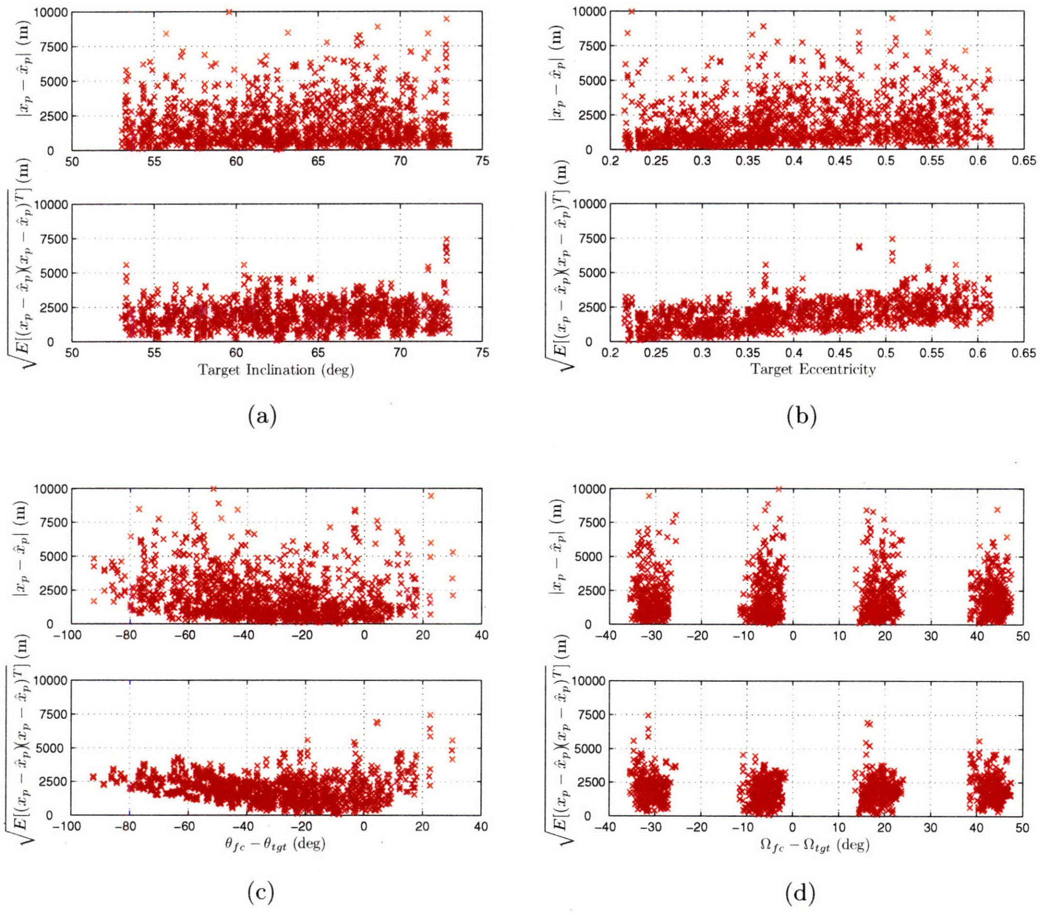

(a)

(b)

(c)

(d)

Figure 7-8: Cumulative simulation target tracking data. The gaps in (d) correlate to the part of the orbit where the cluster is on the other side of the Earth and is not capable of tracking a target in the corridor. Another cluster in the constellation would be responsible for providing tracking capability during these times.

Table 7.5: Correlation coefficients and p-value results for cumulative simulation data. The reported p-values correspond to the chance of getting a correlation coefficient as large as observed by random chance.

	Observation Parameter			
	Actual Position Error		Estimated Position Error	
Variable	Correlation Coefficient	p-value	Correlation Coefficient	p-value
i_{tgt}	0.077	$5.6 \cdot 10^{-3}$	0.096	$5.7 \cdot 10^{-4}$
e_{tgt}	0.227	$1.7 \cdot 10^{-16}$	0.493	$1.1 \cdot 10^{-79}$
$\lvert\theta_{fc} - \theta_{tgt} + 15°\rvert$	0.278	$3.1 \cdot 10^{-24}$	0.328	$1.4 \cdot 10^{-33}$
$\lvert\Omega_{fc} - \Omega_{tgt}\rvert$	-	-	0.074	$7.9 \cdot 10^{-3}$

e_{tgt} and $|\theta_{fc} - \theta_{tgt} + 15°|$ with tracking performance and smaller correlations associated with i_{tgt} and $|\Omega_{fc} - \Omega_{tgt}|$. If there is indeed a casual relationship between $|\theta_{fc} - \theta_{tgt} + 15°|$, i_{tgt}, and $|\Omega_{fc} - \Omega_{tgt}|$ with tracking performance, then the causal relationship is likely driven by the distance between the cluster and the target due to these variables. Tracking accuracy should increase when the cluster is closer to the target.

In general, the eccentricity of the target's orbit has no correlation with distance between the target and the tracking cluster. Given that the correlation is more evident for the estimated position error than actual position error, this suggests that the observed decrease in tracking performance is not due to modeling errors in the Kalman filter target model for larger eccentricities. Rather, an interaction between target trajectory complexity for highly eccentric orbits and the manner in which the covariance matrix is propagated in the estimation Kalman filter may cause the relationship (assuming a causal relationship between target eccentricity and tracking performance does indeed exist). Further investigation into specific Kalman filter performance, which is not in the scope of this thesis, are required to test this hypothesis.

7.3 Chapter Summary

The main purpose of this chapter was to compare the optimal measurement approach to cluster design for target tracking missions to the approach developed in Chapters 5 and 6 that use a heuristic for cluster design to provide good viewing in any direction and a control algorithm that allows relative satellite drift to occur while maintaining simple, mission driven requirements. The first cluster, designed to minimize the average model-based value for the target position estimation error covariance, outperformed the other clusters in the simulation. However, the results from this chapter provide a stronger argument for using the cluster heuristic for designing a target tracking cluster of microsatellites because the increased tracking accuracy is negligible when compared to a single satellite's tracking capability. In addition, the third cluster required significantly less fuel (more than 5 orders of magnitude) than the first cluster. This would significantly reduce the cost from having to replenish the system as satellites run out of fuel. The savings could be re-applied to improved tracking or communication technology. More clusters could also be inserted into the constellation to reduce the chance of missing a target or not having a cluster in tracking range of the target.

Chapter 8

Conclusions and Future Work

This chapter summarizes the thesis with a discussion of the major findings and contributions. This chapter also provides directions for future work to improve and expand upon the work presented in this thesis.

8.1 Thesis Contributions

The primary objective of this thesis was to provide initial insight into the use of a cluster of microsatellites for space-based tracking of a target in an *occupancy corridor* with an unknown time of launch. This objective was achieved by studying the orbital design and maintenance of a cluster of microsatellites for target tracking missions. This research focused primarily on the geometric properties of the cluster in order to understand how the relative motion of the satellites in a cluster affect both target tracking accuracy and cluster-wide fuel consumption. The orbital design of target tracking cluster utilized optimization techniques and an MPC algorithm for cluster maintenance was studied. The approaches presented in this thesis were all validated in a high-fidelity simulation. This section describes the main findings and contributions in orbital design and maintenance of a target tracking cluster.

8.1.1 Orbital Design Using Optimal Measurement Techniques

The research in Chapter 3 utilized an optimal measurement approach to designing a constellation that provides 24-hour coverage of a perceived occupancy corridor. In this research, the nodes of the constellation provided a *formation center* about which the target tracking clusters were designed.

The cluster design approach in Chapter 4 used optimal measurement methods to synthesize the relative orbital elements of satellites in the cluster for a range of cluster parameters (i.e., cluster baseline and assemblage sizes). Results from the model-based cluster design approach suggest that cluster baseline size, rather than assemblage size, is a bigger factor on target tracking accuracy. Clusters with larger baselines consistently provided more accurate estimates of the final position of the target. However, increasing the number of satellites in a cluster improved convergence time. These observations suggests that the *constellation of clusters* approach in this thesis could be improved upon. In particular, a highly populated constellation of microsatellites, where microsatellites are capable of communicating with other neighboring microsatellites, may be a better approach to the problem of designing a space-based system for providing 24-hour tracking coverage of a perceived occupancy corridor.

Another important result of the cluster design problem was the design of a cluster that penalized J_2-induced relative satellite drift. The results from this experiment demonstrated that a target-tracking cluster can be designed that exhibits minimal relative drift with little degradation in target tracking capability. For example, the expected fuel expenditure rate of a 250 km baseline cluster with four satellites was reduced by several orders of magnitude while only increasing the model based expected target position error by approximately 8%.

8.1.2 Heuristic for Cluster Design

An obvious drawback to the model-based optimal measurement methods approach taken in Chapter 4 was that the occupancy corridor needed to be specifically defined. This would rarely be possible. Thus, in Chapter 5 a heuristic was derived for cluster design directly from the information matrix to ensure good cluster viewing geometry for a target in any direction. Findings showed that maximizing the *tetrahedral volume* of a cluster with four or more satellites was an acceptable heuristic for designing a target tracking cluster. The heuristic derived in Chapter 5 provided a simpler, more spatially intuitive approach to cluster design that negated the need to define the target's occupancy corridor.

8.1.3 Cluster Maintenance

The final contributions of this thesis were in cluster maintenance. In Chapter 6, an MPC approach to cluster maintenance was implemented that allowed relative drift to occur in the cluster as long as the cluster maximum baseline and minimum average tetrahedral volume were maintained. This approach allowed control actions over a reconfiguration orbit once every five orbits to minimize the chances of the cluster reconfiguring during a target tracking engagement.

Results in this section confirmed that designing a cluster with a penalty on J_2-induced relative drift reduces fuel expenditure even when relative satellite drift is allowed to occur. Clusters that were designed with a penalty on J_2-induced relative drift used much less fuel than those that did not. However, limitations of a linearized J_2 relative drift metric were observed due to higher order gravity perturbations (i.e., J_3, J_4, etc). True invariant orbits cannot be achieved with a linearized metric that only includes secular J_2 effects. A major contribution in the cluster maintenance problem was the *variable formation center* to account for unmodeled dynamics. The variable formation center was simply found using convex optimization techniques. It reduced fuel consumption by making the control scheme insensitive to cluster wide, long-term perturbational motion. The algorithm achieved reduced cluster wide fuel consumption by choosing the variable formation center to minimize relative out-of-plane motion first. In one example, incorporating a variable formation center into the control algorithm reduced the cluster-wide fuel consumption by over 96%.

8.2 Extensions and Future Work

Possible areas for future work to expand on research in this thesis are presented in this section.

8.2.1 Concept of Operations

The concept of operations for a space-based target tracking system considered in this thesis was a constellation of clusters. Recent advances in both microsatellite technology and the modeling and control of satellites flying in a formation fueled the decision to take this approach. However, the system approach considered in this thesis may not be the best approach, as was demonstrated in Chapter 4. The largest baseline clusters (1000 km) more accurately estimated the state vector of the target at the end of it's trajectory regardless of the number of satellites in the cluster. A highly populated constellation of microsatellites where microsatellites in proximity of each other can communicate information about the target's estimated position and velocity may be a better system approach. Future researchers may want to investigate such a spaced-based system approach to maintaining 24 hour coverage of a perceived occupancy corridor.

8.2.2 Natural Metrics for Formation Flying

Maximizing the average tetrahedral volume proved to be a good heuristic for target tracking cluster design. However, calculating it in this thesis required that the relative motion of the satellites in the cluster be propagated forward. The development of natural metrics for clusters based on the relative orbital elements of the satellites in the cluster ($\delta \mathbf{e}_i$'s) would be a logical extension to this thesis work. Researchers haver previously derived several natural metrics such as maximum, minimum, and mean distance between two elliptical orbits [15, 20]. Similar tools in the arena of formation flying could be very useful. They could be applied to this thesis project to estimate average tetrahedral volume of the cluster. They could also easily be extended to many other formation flying missions such as MMS where they may play a useful role.

8.2.3 Cluster Coordination

At this point it is tempting to suggest that a logical extension that comes from findings in this thesis is a need for a better relative satellite motion model. However, better models already exist. They just do not lend themselves well to control algorithms and modeling satellite motion because of their complexity. It would be possible (but perhaps not rational) to incorporate models for all the disturbances that play a role in satellite relative motion into cluster coordination algorithms.

Instead, future researchers could develop techniques that make control schemes insensitive to unmodeled disturbances. In this thesis, allowing relative satellite drift to occur reduced fuel consumption while maintaining simple, mission driven characteristics (i.e., maximum baseline and minimum average volume). The variable formation center also reduced fuel consumption without hindering the cluster's target tracking capability. The variable formation center had the effect of making the control algorithm insensitive to cluster-wide long term variations from higher order gravitational disturbances. Future researchers would have to deeply consider mission requirements (whether they be scientific, defense-related or commercial missions) and tailor the control scheme to reasonably satisfy those requirements without consuming unnecessary fuel.

An immediate extension on the work in this thesis would be a better way to model communication constraints between satellites in a cluster. The three-dimensional cube baseline constraint was chosen to represent communication constraints between satellites because it could be easily posed as a linear constraint. However, this linear constraint may have unnecessarily limited satellite relative motion and effectively increased cluster-wide fuel consumption.

THIS PAGE INTENTIONALLY LEFT BLANK

Bibliography

[1] Jonathan Alon and Stan Sclaroff. Recursive estimation of motion and planar structure. In *Computer Vision and Pattern Recognition*, volume 2, pages 550–556, Hilton Head Island, SC, 13-15 June 2000. IEEE.

[2] Ali Azarbayejani and Alex Pentland. Recursive estimation of motion, structure, and focal length. *IEEE Transactions on Pattern Analysis and Machine Intelligence*, 17(6):562–575, 1995.

[3] Richard H. Battin. *An Introduction to the Mathematics and Methods of Astrodynamics, Revised Edition.* American Institute of Aeronautics and Astronautics, Inc, Reston, 1999.

[4] Louis Breger and Jonathan P. How. GVE-based dynamics and control for formation flying spacecraft. In *2nd International Symposium of Formation Flying Missions and Technologies*, Washington, DC, 14-16 September 2004.

[5] Louis Breger and Jonathan P. How. J2-modified GVE-based MPC for formation flying spacecraft. In *AIAA Guidance, Navigation, and Control Conference and Exhibit*, San Francisco, CA, August 2005. AIAA.

[6] Louis Breger and Jonathan P. How. Partial J_2-invariarance for spacecraft formations. In *AIAA Guidance, Navigation, and Control Conference and Exhibit.* AIAA, August 2006.

[7] Louis Breger and Jonathan P. How. Gauss's variational equation-based dynamics and control for formation flying spacecraft. *Journal of Guidance, Control, and Dynamics*, 30(2):437–448, March-April 2007.

[8] Louis Scott Breger. Model predictive control for formatin flying spacecraft. Master's thesis, Massachusetts Institute of Technology, 2004.

[9] D. Brouwer. Solution of the problem of artificial satellite theory without drag. *Astronautical Journal*, 64(1274), 1959.

[10] Robert Grover Brown and Patrick Y. C. Hwang. *Introduction to Random Signals and Applied Kalman Filtering.* John Wiley and Sons, Inc., 1997.

[11] Irene A. Budianto, Diane Gerencser, and Patrick J. McDaniel. Design and analysis of a small constellation of satellites for mid-course tracking. *Advances in the Astronautical Sciences*, 116(3):2093–2106, 2003.

[12] E. F. Camacho and C. Bordons. *Model Predictive Control.* Springer-Verlag London Limited, London, 1999.

[13] Vladimir A. Chobotov. *Orbital Mechanics, Third Edition.* American Institute of Aeronautics and Astronautics, Inc, Reston, 2002.

[14] Dong-Woo Gim and Kyle T. Alfriend. The state transition matrix of relative motion for the perturbed non-circular reference orbit. *Journal of Guidance, Control and Dynamics*, 26(6):956–971, 2003.

[15] Pini Gurfil. Distances on the relative spacecraft motion manifold. In *Guidance, Navigation, and Control Conference*, San Francisco, August 2005. AIAA.

[16] José J. Guzmán and Conrad Schiff. A preliminary study for a tetrahedron formation: Quality factors and visualization. In *AIAA/AAS Astrodynamics Specialist Conference and Exhibit*, California, August 2002. AIAA.

[17] Jonathan How. MIT Course 16.323: Principles of Optimal Control. Lecture Notes, 2006. MIT OpenCourseWare, URL: http://ocw.mit.edu/OcwWeb/Aeronautics-and-Astronautics/16-323Spring-2006/CourseHome/index.htm.

[18] Stephen P. Hughes and Laurie M. Mailhe. A preliminary formation flying orbit dynamics analysis for Leonardo-BRDF. In *IEEE Aerospace Conference*, pages 579–596, 2001.

[19] Gokhan Inalhan, Franz D. Busse, and Jonathan P. How. Precise formation flying control of multiple spacecraft using carrier-phase differential GPS. In *The AAS/AIAA Space Flight Mechanics Meeting*, pages 151–165, Clearwater, FL, 23-26 January 2000. AAS/AIAA.

[20] K. V. Kholshevnikov and N. N. Vasiliev. Natural metrics in the spaces of elliptic orbits. *Celestial Mechanics and Dynamical Astronomy*, 89:119–125, Mar 2004.

[21] R. H. Lyddane. Small eccentricities or inclinations in the brouwer theory of the artificial satellite. *Astronomical Journal*, 68(8), 1963.

[22] V. V. Malyshev, M. N. Krasilshikov, and V. I Karlov. *Optimization of Observation and Control Processes.* American Institute of Aeronautics and Astronautics, Inc, Washington, DC, 1992.

[23] Maurice Martin and Michael J. Stallard. Distributed satellite missions and technologies - the TechSat 21 program. In *AIAA Space Technology Conference and Exposition*, Alburqureque, NM, Sept 1999. AIAA.

[24] David Mishne. Formation control of satellites subject to drag variations and J_2 perturbations. In *Journal of Guidance, Control, and Dynamics*, volume 27, pages 685–692. AIAA, July-August 2004.

[25] Patrick Robert, Alain Roux, Christopher C. Harvey, Malcolm W. Dunlop, Patrick W. Daly, and Karl-Heinz Galssmeier. Tetrahedron geometric factors. In *Analysis Methods for Multi-Spacecraft Data*, pages 323–348. ESA Publications Division, 1998.

[26] A. E. Roy. *Orbital Motion.* Institute of Physics Publishing, London, 4th edition, 2005.

[27] Luke Michael Sauter. Satellite constellation design for mid-course ballistic missile intercept. Master's thesis, Massachusetts Institute of Technology, 2002.

[28] Daniel P. Scharf, Fred Y. Hadaegh, and Scott R. Ploen. A survey of spacecraft formation flying guidance and control (part I): Guidance. In *Proceedings of the American Control Conference*, volume 2, pages 1733–1739, Denver, CO, June 2003. IEEE.

[29] Daniel P. Scharf, Fred Y. Hadaegh, and Scott R. Ploen. A survey of spacecraft formation flying guidance and control (part II): Control. In *Proceedings of the American Control Conference*, Boston, MA, June-July 2004. AACC.

[30] Hanspeter Schaub and Kyle T. Alfriend. Impulsive feedback control to establish specific mean orbit elements of spacecraft formations. *Journal of Guidance, Control and Dynamics*, 24(4):739–745, 2001.

[31] Hanspeter Schaub and Kyle T. Alfriend. J2 invariant relative orbits for spacecraft formations. *Celestial Mechanics and Dynamical Astronomy*, 79(2):77–95, February 2001.

[32] Samuel A. Schweighart and Raymond J. Sedwick. High-fidelity linearized J2 model for satellite formation flight. *Journal of Guidance, Control, and Dynamics*, 25(6):1073–1080, 2002.

[33] Hanspeter Shaub and John L. Junkins. *Analytical Mechanics of Space Systems.* American Intitute of Aeronautics and Astronautics, Inc, Reston, 2003.

[34] Leena Singh, E. Griffith, and J. Griffith. Optimal satellite formation determination for distributed target state estimation. In *American Control Conference*, 2007. To be published.

[35] The Mathworks, Inc. Optimization toolbox user's guide. website: http://www.mathworks.com/access/helpdesk/help/pdf_doc/optim/optim_tb.pdf, April 2007.

[36] Michael Tillerson, Louis Breger, and Jonathan P. How. Distributed coordination and control of formation flying spacecraft. In *The American Control Conference*, volume 2, pages 1740– 1745, 4-6 June 2003.

[37] Michael Tillerson and Jonathan P. How. Formation flying control in eccentric orbits. In *AIAA Guidance, Navigation, and Control Conference and Exhibit*, Montreal, Canada, 6-9 August 2001. AIAA.

[38] Michael Tillerson and Jonathan P. How. Advanced guidance algorithsm for spacecraft formation-keeping. In *The American Control Conference*, pages 2830–2835, Anchorage, AK, 8-10 May 2002.

[39] Michael Tillerson, Gokhan Inalhan, and Jonathan P. How. Co-ordination and control of distributed spacecraft systems using convex optimization techniques. *International Journal of Robust and Nonlinear Control*, 12(2-3):207–242, 2002.

[40] Dariusz Uciński. *Optimal Measurement Methods for Distributed Parameter System Identification.* CRC Press LLC, New York, 2005.

[41] Veera Vaddi. *Modeling and Control of Satellite Formations.* PhD thesis, Texas A&M University, 2003.

[42] J. G. Walker. *Satellite Constellations.* British Interplanetary Society, 1984.

[43] James R. Wertz. *Space Mission Analysis and Design.* Kluwer Academic Publishers, Boston, 1999.

[44] James R. Wertz. *Mission Geometry; Orbit and Constellation Design and Management.* Microcosm Press and Kluwer Academic Publishers, Boston, 2001.

[45] J. Williamsen. Review of space shuttle meteoroid/orbital debris critical risk assessment practices. 45th Structures, Dynamics, And Materials Symposium. AIAA, April 2004.